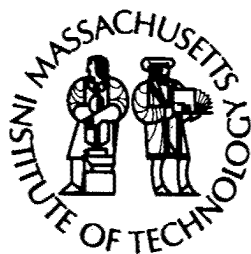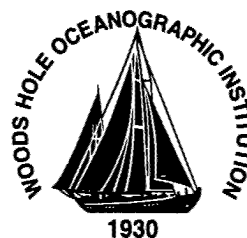# Massachusetts Institute of Technology
Woods Hole Oceanographic Institution

Joint Program in Oceanography/ Applied Ocean Science and Engineering

1930

DOCTORAL DISSERTATION

Acoustic Scattering by Axisymmetric Finite-Length Bodies with Application to Fish: Measurement and Modeling

by

D. Benjamin Reeder

June 2002

20030515 102

MIT/WHOI

2002-11

Acoustic Scattering by Axisymmetric Finite-Length Bodies with Application to Fish: Measurement and Modeling

by

D. Benjamin Reeder

Massachusetts Institute of Technology
Cambridge, Massachusetts 02139

and

Woods Hole Oceanographic Institution
Woods Hole, Massachusetts 02543
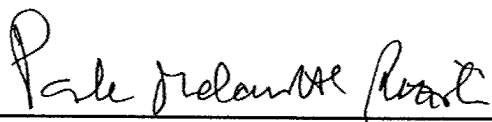
June 2002

DOCTORAL DISSERTATION

Approved for publication; distribution unlimited.
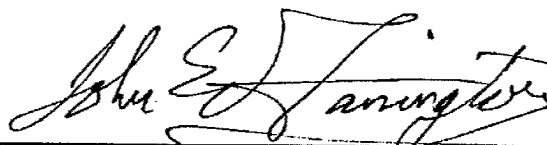
Approved for Distribution:

_____
W. Rockwell Geyer, Chair
Department of Applied Ocean Physics and Engineering

_____
Paola Malanotte-Rizzoli
MIT Director of Joint Program

_____
John W. Farrington
WHOI Dean of Graduate Studies

Acoustic Scattering by Axisymmetric Finite-length Bodies with Application to Fish: Measurement and Modeling

by

D. Benjamin Reeder

B.S., Clemson University (1988)

Submitted to the Department of Ocean Engineering, MIT and the
Department of Applied Ocean Physics and Engineering, WHOI
in partial fulfillment of the requirements for the degree of

Doctor of Philosophy

at the

MASSACHUSETTS INSTITUTE OF TECHNOLOGY
AND THE
WOODS HOLE OCEANOGRAPHIC INSTITUTION

June 2002

© 2002 D. Benjamin Reeder. All rights reserved.

The author hereby grants to Massachusetts Institute of Technology
and the
Woods Hole Oceanographic Institution permission to reproduce and
to distribute copies of this thesis document in whole or in part.

Signature of Author . . . .
Department of Ocean Engineering, MIT and the
Department of Applied Ocean Physics and Engineering, WHOI
May 1, 2002
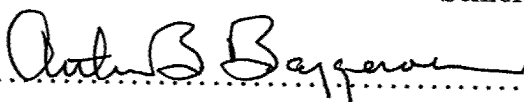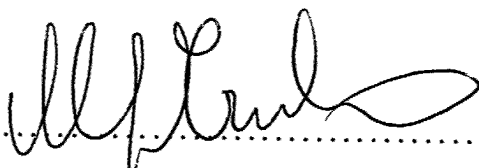
Certified by . . . .
Dr. Timothy K. Stanton
Senior Scientist, WHOI
Thesis Advisor

Certified by . . . .
Prof. Arthur B. Baggeroer
Professor, MIT
Academic Advisor

Accepted by . . . .
Michael S. Triantafyllou
Chair, Joint Committee for Applied Ocean Science and Engineering
Massuchusetts Institute of Technology and the Woods Hole Oceanographic Institution

Acoustic Scattering by Axisymmetric Finite-length Bodies with Application to Fish: Measurement and Modeling

by

D. Benjamin Reeder

Abstract

This thesis investigates the complexities of acoustic scattering by finite bodies in general and by fish in particular through the development of an advanced acoustic scattering model and detailed laboratory acoustic measurements. A general acoustic scattering model is developed that is accurate and numerically efficient for a wide range of frequencies, angles of orientation, irregular axisymmetric shapes and boundary conditions. The model presented is an extension of a two-dimensional conformal mapping approach to scattering by irregular, finite-length bodies of revolution. An extensive series of broadband acoustic backscattering measurements has been conducted involving alewife fish (*Alosa pseudoharengus*), which are morphologically similar to the Atlantic herring (*Clupea harengus*). A greater-than-octave bandwidth (40-95 kHz), shaped, linearly swept, frequency modulated signal was used to insonify live, adult alewife that were tethered while being rotated in 1-degree increments over all angles of orientation in two planes of rotation (lateral and dorsal/ventral). Spectral analysis correlates frequency dependencies to morphology and orientation. Pulse compression processing temporally resolves multiple returns from each individual which show good correlation with size and orientation, and demonstrate that there exists more than one significant scattering feature in the animal. Imaging technologies used to exactly measure the morphology of the scattering features of fish include very high-resolution Phase Contrast X-rays (PCX) and Computerized Tomography (CT) scans, which are used for morphological evaluation and incorporation into the scattering model. Studies such as this one, which combine scattering models with high-resolution morphological information and high-quality laboratory data, are crucial to the quantitative use of acoustics in the ocean.

Thesis Advisor: Dr. Timothy K. Stanton
Title: Senior Scientist, WHOI

Academic Advisor: Prof. Arthur B. Baggeroer
Title: Professor, MIT

Acknowledgments

Contents

---

[1]This chapter is based on an article submitted to the Journal of the Acoustical Society of America (Reeder and Stanton, submitted).

---

[2]This chapter is based on an article submitted to the Journal of the Acoustical Society of America (Reeder *et al.*, submitted).

Chapter 1

Introduction

1.1 Historical background for the use of sound in underwater observations

The first significant experiment in underwater acoustics was conducted by Colladon and Sturm in 1826 in the waters of Lake Geneva, Switzerland. By striking a bell underwater while simultaneously setting off a flash of light from explosives above the water, an observer in a boat some distance away measured the time lapse between the flash of light and the arrival of the sound of the ringing bell underwater. Colladon and Sturm, in a single experiment, not only a established a good value for the speed of sound (c) in fresh water but simultaneously, and possibly unintentionally, demonstrated the fact that as light and sight are the primary means of assessing the world above water, sound is the method of choice to observe the underwater world. Water is opaque to light but is

transparent to sound which can travel great distances through the ocean and be detected at low frequencies even at megameter ranges (Baggeroer *et al.*, 1994).

Medwin and Clay (1998) opine that acoustical oceanography (the use of sound to study oceanographic processes) got its start in 1912, with the sinking of the HMS Titanic. Within months of the tragedy, patents were filed for new sonar systems to detect the presence of large objects underwater using acoustic backscattering. In fact, within 20 years of the Titanic's sinking, sonar was being used for the detection of schools of fish. Since that time, the science of underwater acoustics has progressed and has been applied in many ways to study the ocean environment. Much interest continues in the study of how human-generated sound interacts with marine organisms, whether for the purpose of understanding how the sound affects marine mammal behavior or for the purpose of detecting and tracking marine organisms. Acoustic scattering from marine organisms is the focus of much research by a diverse number of individuals: the academic biologist/acoustician, the commercial fisherman, the fisheries manager and the military sonar engineer.

1.2   Current interest in ocean observation

Just as in the 1930's, the modern commercial fisherman uses sonar to detect and localize the presence of schools of fish to maximize the catch. Given the limits on the number of fishing days and types of harvested fish allowed, remotely classifying fish would be advantageous for the commercial fisherman in order to avoid unnecessary catches of

unwanted species and to maximize time at sea by limiting operational costs in terms of payroll and fuel.

The fisheries manager is tasked with observing and estimating fish populations in particular regions of the ocean to prevent over-fishing and the resultant collapse of the fisheries as happened in New England (Fogerty and Murawski, 1998; Steele, 1998), or worse, the extinction of particular species due to over-fishing or habitat destruction.

The academician is interested in better understanding the distribution, diversity, abundance and size distributions of fish populations in order to assess the state of the resources present in the ocean and changes in the environment in which these organisms live. Without knowledge of these factors, it is difficult to determine, much less predict, the effect on populations of low availability of food supplies for each species or the effect of over-fishing by humans.

The military sonar engineer is interested in observing and understanding how sound interacts with boundaries such as the sea surface, the seafloor, turbulence, internal waves, bubbles and marine organisms. Organism-based sound can be due to scattering from the animal or actually produced by the animal itself, e.g., whales, dolphins and snapping shrimp (Au and Banks, 1998; Olivieri and Glegg, 1998; Versluis *et al.*, 2000; Schmitz *et al.*, 2000). For active sonar systems seeking an acoustic target, organism-based interference contributes to the background reverberation detected by the sonar, decreasing the signal-to-noise ratio (SNR) and lowering the probability of detection (Urick, 1983).

1.3 Methods of ocean observation

Historically, scientists have relied on ocean surveys involving direct sampling with various types of nets to assess organism populations. Direct sampling furnishes biological data like abundance, biomass, length and species identification but is time-consuming and expensive. The catch may not be representative of the biomass in the water column since the net is selective, and as many marine organisms are free swimmers, the animals can avoid the net. Some delicate animals are destroyed by the nets, making it difficult to count the catch. The population estimate generated from the survey is susceptible to error since the sampling volume is small relative to the size of the region that is being surveyed. The abundance estimate from the small volume is then extrapolated to the whole, large region, causing errors to be propagated and amplified in the biomass estimate.

To overcome the problems and limitations plaguing the biological oceanographer and fisheries manager, the use of acoustic technology has made it possible to do rapid, high-resolution, broad-scale synoptic surveys of marine organisms (Gunderson, 1993). An acoustic survey would be less expensive by sampling the entire water column at a much faster rate, requiring less ship-time and labor while providing total coverage of the surveyed region. The acoustic survey is non-invasive, eliminating the problems of net avoidance and destruction of the organisms. The potential exists for the acoustic survey to produce high-resolution maps that can help advance understanding of aquatic community compositions, predator-prey interactions and habitat utilization (Horne, 1998).

Acoustic sampling produces acoustic data, not biological data; therefore, the acoustic backscattered signal must be translated into meaningful biological information. Abundance estimates using echo sounders have been made for several decades; however, these estimates are quite often based on the assumptions that (1) the aggregation is composed of animals of a single size and species, (2) the echo energy is proportional to the product of the number of animals per unit volume and average backscattering cross section, and (3) the average backscattering cross section is relatively constant for a given size and species, implying variations in echo energy are related to variation in numerical density. Directly relating acoustic scattering strength to biomass can be an unreliable indicator of abundance. The scattering strength of an organism depends upon the anatomical features of the animal, which vary widely between species that may even be of the same individual size or biomass, introducing large errors in the abundance estimates (Foote, 1980; Stanton *et al.*, 1994a). Dawson and Karp (1990) observed that fish at nearly horizontal aspect experienced approximately 10 dB target strength variations, apparently due to its swimming motion only. In an earlier study, Nakken and Olsen (1977) noted a 20 dB variation over time for a swimming Atlantic cod (*Gadus morhua*) at zero tilt angle.

Therefore, the goal of inverting acoustic scattering by marine organisms for meaningful biological information such as species, size and numerical density requires an understanding of the scattering characteristics of each type of organism. In other words, solving the inverse problem requires a detailed knowledge of the forward problem of

predicting the acoustic scattering based on each animal's unique acoustic signature.

In the case of the impact of reverberation on the performance of military sonar systems, characterization of the complex reverberant properties of the water column has been largely ignored, i.e., the physics of the scattering by inhomogeneities, and specifically, marine organisms has not been taken into account in any significant way. Detailed physics-based characterization of marine organisms' scattering properties over a wide range of frequencies could lead to improvements in sonar system performance.

1.4 The physics of acoustic scattering

In order to exploit the properties of sound transmission and interaction with boundaries in the ocean, the physics of the scattering must be formalized and the factors affecting scattering studied in detail.

The far-field scattered sound wave is expressed as:

$$P^{scat} \underset{r \to \infty}{\longrightarrow} P_{inc} \frac{e^{ikr}}{r} f, \tag{1.1}$$

where P^{inc} is the pressure amplitude of the incident acoustic wave upon the object at a distance r away, k $(= 2\pi/\lambda, \lambda =$ wavelength$)$ is the acoustic wavenumber of the incident field and f is the scattering amplitude. Given the dynamic range of the far-field scattering amplitude in the backscatter direction, it is often expressed in logarithmic terms as target strength (TS), expressed in units of decibels (dB) relative to 1 m (Urick,

1983):

$$TS = 10 \log_{10} \sigma_{bs}, \tag{1.2}$$

where σ_{bs} is the differential backscattering cross section, which can be considered to be a measurement of the effective (acoustic) area of the target. The equation can be represented in another form:

$$TS = 20 \log_{10} |f_{bs}|, \tag{1.3}$$

where f_{bs} is the backscattering amplitude and $\sigma_{bs} = |f_{bs}|^2$.

The scattering amplitude, f, is a complex function of the size, shape, orientation and material properties of the scatterer as well as the wavelength of the incident acoustic field. The scattering characteristics of the object are fully described by the scattering amplitude whose accurate parameterization is the focus of scattering physics research.

Prediction of an organism's scattering properties requires detailed, accurate measurement of the acoustic scattering characteristics of the animal of interest as well as a detailed theoretical scattering model to quantify the nature and extent to which size, shape, material properties, orientation and frequency affect scattering characteristics (Greenlaw and Johnson, 1983).

1.5 Overview of relevant work

Two vast bodies of literature exist on acoustic scattering that are nearly independent of each other: one consists of general scattering research without specific application,

while the other consists of studies on scattering by marine organisms specifically. Since the objective of this thesis is to contribute to both of these fields of study, the following paragraphs provide an overview of work done in both areas and a description of the factors that contribute to the complexity of scattering physics.

1.5.1 General scattering

Solutions to the wave equation can be approached in a number of different ways. Possible approaches can be categorized as exact analytical, exact numerical or approximate methods of solution.

Exact analytical solutions to the wave equation require the scatterer surface to exactly match the locus of all points for a constant radial coordinate. Such exact analytical solutions exist only for a limited number of simple geometries (eleven) for which the separation of variables is possible (Morse and Feshbach, 1953; Bowman *et al.*, 1987). These exact analytical solutions are limited to smooth, simple geometries, such as the sphere, infinitely long cylinder, or spheroid. Exact analytical solutions for acoustic scattering was first investigated in the 1870's by Lord Rayleigh (1945), where he considered the case of spherical and infinitely long cylindrical scatterers whose cross sections were small compared to the wavelength of the incident sound. Anderson (1950) presented an exact solution for scattering from a fluid sphere. Scattering by solid, rigid spheres and cylinders was investigated by Morse (1981), as well as Faran (1951) who focused on shear waves of the object. Junger (1951) formulated scattering from thin elastic,

air-filled shells of spherical and cylindrical shape in terms of "rigid body scattering" and "radiation scattering". Goodman and Stern (1962) addressed the problem of scattering by elastic spherical shells in which the material properties of the surrounding medium and the interior of the shell differ from the shell itself. Since scattering from simple spherical and infinitely long cylinders is not sufficient to describe scattering from realistic scatterers found in nature, scattering by prolate spheroids has been investigated by Spence and Granger (1951), Weston (1967), Yeh (1967), Furusawa (1988) and Ye *et al.* (1997). Some of these exact modal series solutions were transformed through use of the Sommerfeld-Watson Transformation to obtain an exact formulation for the rays scattered by bodies (Uberall, 1966; Williams and Marston, 1985).

Exact numerical solutions to the wave equation are required, particularly at high frequencies, once the scatterer shape deviates from a simple geometry, as do most realistic scatterers of interest. These formally exact, numerically solved methods include the perturbation method (Ogilvy, 1991) which is limited to shapes that are close to a separable geometry, the T-matrix method (Waterman, 1968; Varadan *et al.*, 1982; Lakhtakia *et al.*, 1984; Hackman and Todoroff, 1985) and solving the boundary integral equation by the boundary element method (Tobocman, 1984; Francis, 1993). These numerical models are limited in that they can be computationally intensive and numerically unstable as the frequency or irregularity of the surface increases.

Approximate solutions are useful in that they provide an analytical solution under certain conditions of validity in which no exact solution exists, or they attempt to avoid

15

unwieldy analytical formulations or numerical difficulties inherent in the numerical implementation of exact solutions. Approximate analytical solutions include the physical optics, or Kirchhoff, approximation (Born and Wolf, 1999; Neubauer, 1963; Junger, 1982; Gaunaurd, 1985) which involves an integral over the scatterer surface, the Born approximation (Born and Wolf, 1991) and Distorted Wave Born Approximation (DWBA) (Stanton et al., 1993; Chu et al., 1993) which involve an integral over the volume of the scatterer and the deformed cylinder method (Stanton, 1988a, 1988b, 1989a, 1989b) which involves a line integral. Other approximate solutions include the geometric theory of diffraction (Levy and Keller, 1959; Yamashita, 1990) which is based on the superposition of scattered rays, as well as a ray solution for curved edges based on the exact solution for straight edges (Svensson et al., 1999). Approximate analytical solutions also include asymptotic formulations based on the exact solutions for the cases of low and high frequencies (Sammuelmann, 1988). While each of these approximations may perform well in their respective ranges of validity, they are all limited in one or more of the following conditions: frequency range, class of surfaces, types of boundary conditions and eccentricity of shape.

1.5.2 Scattering from marine life

In the particular field of acoustic scattering by marine organisms, the multitude of different species of zooplankton and fish that occupy the water column make it impractical to study and acoustically characterize each individual species. Figure 1-1 illustrates the

categorization by gross anatomical structure and the approximation by simpler shapes necessary to describe the important scattering mechanisms of the animals. The great complexities of the physics of the scattering require detailed measurements and development of models to accurately characterize scattering from marine organisms.

Acoustic measurements of fish

Much research has been conducted to quantify, in terms of target strength, the efficiency with which fish scatter sound (Midttun, 1984). Studies include measurement of target strengths *in situ* and *ex situ*, with multiple and single targets. *In situ* measurements are conducted in the natural environment yet present the challenge of unknown target size, orientation and position relative to the acoustic beam; *ex situ* measurements, however, provide greater control over these factors (Foote, 1997). *Ex situ* measurements of tethered fish (similar to the method presented in Chapter 3 of this thesis) include those conducted by Jones and Pearce (1958), Haslett (1969, 1977), Diercks and Goldsberry (1970), Love (1969, 1970, 1971), and Nakken and Olson (1977). In spite of the fact that these measurements were performed at a limited number of angles of orientation (mostly dorsal), they were performed on a variety of species of different sizes and at a number of different frequencies and demonstrate complicated variability that is dependent upon morphology, orientation and acoustic wavelength.
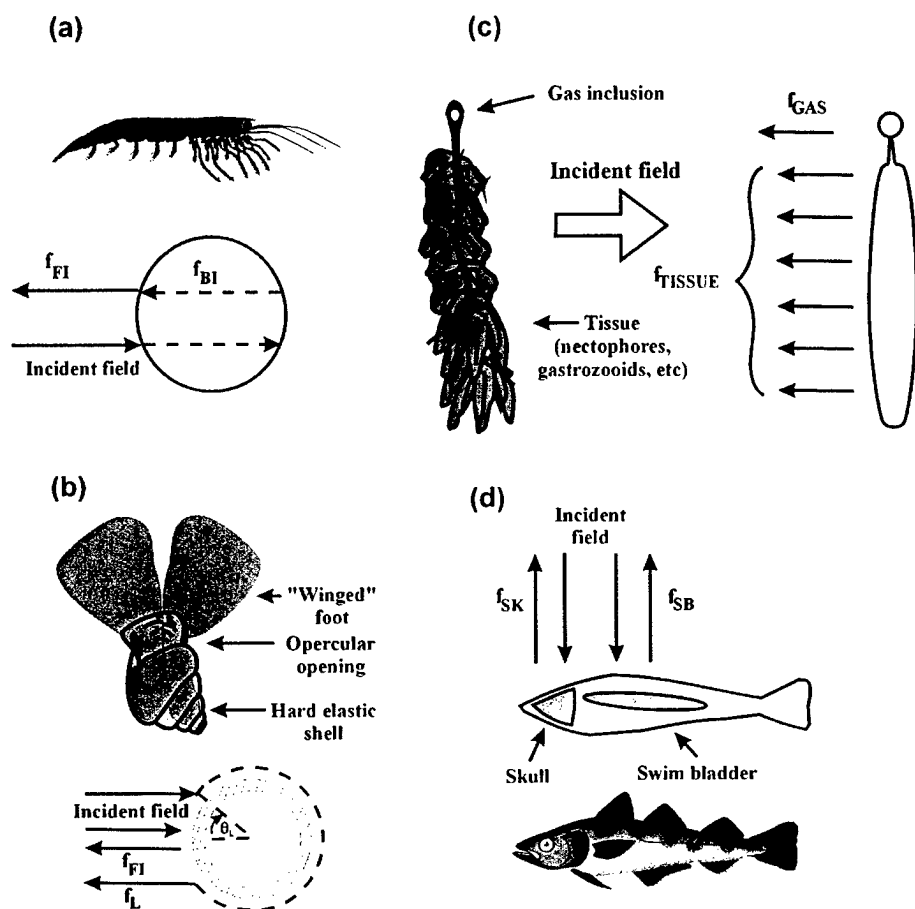
Figure 1-1: Several anatomical groups of zooplankton and fish, and certain important scattering components: (a) fluid-like, (b) elastic-shelled, (c) gas-bearing zooplankton, and (d) gas-bearing (swimbladder) fish. The scattering amplitude from the various anatomical features is indicated by an $f(...)$. Adapted from Stanton *et al.*, 1998b.

Modeling scattering from fish

Attempts have been made to empirically quantify the relationship between echo amplitude and actual fish length (Love, 1977; Foote, 1987). Although linear regression curves have been used with some success, they are constrained to certain frequencies and species, and by the system's ability to acoustically resolve individuals within aggregations (Horne and Jech, 1999). More sophisticated scattering models are required to better account for the complexities introduced by shape, orientation and material properties. As mentioned earlier, the existence of numerous species with different shape and material properties requires some simplification in the modeling.

For low frequency applications, the acoustically dominant swimbladder has been modeled as a sphere (Andreyeva, 1964; Love, 1978; Ye and Farmer, 1994; Feuillade and Nero, 1998) and as a prolate spheroid (Weston, 1967; Ye, 1996). Scattering from simple spherical shapes is not sufficient to describe scattering from animals with more irregular shapes, particularly at high frequencies. Efforts have been made to describe the scattering by more realistic, elongated shapes. For example, Clay (1991) modified Stanton's (1988a, 1989a) deformed finite cylinder model and derived a ray-mode model for fish using a combination of gas- and fluid-filled cylinders.

Including the exact shape and size of the dominant scattering components of the animal is a crucial, yet very difficult aspect of building an accurate backscattering model. Modeling of the scattering of sound by complex body shapes is a difficult problem due to the mathematical challenge of exact solutions and the computational difficulties of

19

numerical approaches, as mentioned above. A number of approaches have been used to more closely represent the exact shape of the dominant scattering mechanisms. Arrays of point scatterers (Clay and Heist, 1984) have been used to model the fish body form. Clay (1991) developed the Kirchhoff ray-mode (KRM) model of finite cylinders that combines a modal solution for $ka < 0.15$ and a Kirchhoff approximation for $ka > 0.15$ to take advantage of the performance of the two models as a function of ka. Note that ka is a non-dimensional form of frequency, and a is the radius of the cylinder. Clay and Horne (1994) modeled acoustic backscatter of Atlantic cod (*Gadus morhua*) using the KRM model. Do and Surti (1990) used a series of cylinders and cones similar in concept to the KRM. Jones and Pearce (1958) and Haslett (1962b) attempted to experimentally approximate the shape of a fish swimbladder as a cylinder and ellipsoid, respectively. Foote (1985) computed the target strength of fish by applying the Kirchhoff approximation to a more realistic 3-dimensional model of the swimbladder based on the digitized microtomed swimbladder of pollack (*Pollachius pollachius*) and saithe (*Pollachius virens*). Foote and Francis (1999) modeled the target strength of swim-bladdered fish using the boundary element method based on the same swimbladder shapes in Foote (1985). Models using the exact shape of the animal's morphology are desired because they are more realistic and promise greater accuracy over models based on simple geometric shapes, especially in the geometric scattering region (high ka). As in the case of general scattering models, fish scattering models are generally limited with respect to frequency range, class of surfaces, types of boundary conditions, eccentricity of shape and/or numerical efficiency.

Complexities of scattering from marine life

Morphology

In the case of fish, morphology (size, shape and material properties) creates sound speed and density contrasts that have significant effect upon the scattering. Swimbladders have been considered to be the dominant scattering mechanism based on estimates that swimbladders cause as much as 90-95% of the target strength of fish under certain conditions due to the large acoustic contrast between the air-filled swimbladder and the surrounding tissue and water (Foote, 1980). Their influences on the acoustic signatures have been studied intensively by Jones and Pearce (1958), Andreyeva (1964), Weston (1967), Haslett (1962c), Hawkins (1977), Love (1978) and Foote (1980, 1985). While the size and shape of swimbladders may dominate the scattering properties of fish, other parts of the anatomy create acoustic impedance contrasts which contribute, particularly for fish without swimbladders, to the overall scattering, e.g., skull, vertebral column, muscle tissue and gonads. The extent to which each of these individual anatomical features contributes to the scattering from the whole fish is generally unknown, although some studies have illustrated their importance (Sun *et al.*, 1985).

Orientation

Orientation has a profound effect upon scattering (Nakken and Olsen, 1977; Foote, 1985) at the higher frequencies. The effect of angle of orientation on scattering from the animal is further complicated by the movement of the animal during measurement (Zakharia, 1990). Slight movements of the animal in the laboratory setting reflect the

greater complexity of *in situ* measurements and acoustic surveys, where animal orientation influences the received scattered signal.

Behavior and physiological changes

The physical parameters of morphology and orientation mentioned above are also influenced by behavior, further complicating the process of accurately measuring their acoustic properties. Those factors include depth excursions, swimming motion that changes aspect, ingesting and expelling of air to change buoyancy, size of the gut after feeding, seasonal effects such as spawning, and physiological effects such as voluntary muscular tension on the swimbladder wall (Hawkins, 1981; Feuillade and Nero, 1998).

Frequency

Generally, the scattering strength of a fish varies with frequency (Haslett, 1962a; Love, 1969, 1971). At very low frequencies in the Rayleigh scattering region, the backscattering cross section is proportional to the fourth power of frequency. At swimbladder resonance frequencies, backscattering cross section varies with fish size and frequency. In the geometric scattering region at higher frequencies, it depends on multiple scattering features in the fish which will cause interference in a manner specific to its anatomy, and that interference pattern is dependent upon frequency (Haslett, 1962c). In other words, the physical separation of scattering features in the fish relative to acoustic wavelength determines the interference pattern.

Broadband

The vast majority of acoustic measurements on fish are in terms of target strengths

at single frequencies. Although this level of information can be invaluable for fishery population estimates, traditional target strength measurements lack coherent information necessary for extracting more detailed information, such as size and species identification. Specifically, narrowband measurements are performed at discrete frequencies, thus frequency dependencies are missing from the data, although this has been addressed in part by use of multiple discrete frequencies. Since an animal's scattering properties vary considerably with the frequency of the transmitted signal, the use of broadband transducers would offer continuous coverage over a significant range of frequencies, thus increasing the amount of information contained in the signal. Furthermore, the broadband signals inherently have high temporal resolution (which varies with inverse bandwidth of the transmitted signal) which can be realized through the use of an impulse signal or pulse compression of a longer signal (Chu and Stanton, 1998). With high temporal resolution, scattering features can be realized in the time domain. In spite of the great advantages of broadband signals, relatively few studies have investigated the finer structure of the animal's spectral characteristics (Kjaergaard *et al.*, 1990; Simmonds *et al.*, 1996; Zakharia *et al.*, 1996). Characterizing an animal's scattering properties over a broad bandwidth is made difficult by the lack of well-performing and affordable broadband transducers in the desired frequency ranges, but advances in the field are being made.

1.6   Purpose of this thesis

As demonstrated by the research outlined above, predicting and modeling the scattering of sound by irregular finite objects is formidable. Successful use of acoustics by the biologist, commercial fisherman, fisheries manager and military sonar engineer requires accurate scattering models for each category of object or animal, verification of the models through accurate measurements of scattering from those objects or animals, and reliable inversion algorithms.

In particular, a general acoustic scattering model is needed that is numerically efficient over a wide range of frequencies for all angles of orientation (three-dimensional), for realistic shapes and boundary conditions. In addition, high-resolution measurements of the morphology of fish are needed to accurately represent the exact shapes of the scattering features in the fish on which the models are based. Furthermore, high-quality acoustic backscattering measurements of fish are needed for the identification of dominant scattering mechanisms of fish and testing and refinement of the scattering models. The acoustic measurements need to be performed under the following conditions: (1) live, healthy fish in an environment that mimics their natural environment, (2) control of the position of the fish within the acoustic beam to allow measurements of target strength, (3) control of angle of orientation with high angular resolution, (4) measurements in more than one plane, and (5) the use of broadband signals to make possible spectral and time-domain processing techniques. The measurements, analysis and modeling presented in this thesis seek to meet these needs.

Chapter 2 of this thesis describes the development of an advanced acoustic scattering model that can be used in a wide variety of applications, including scattering from fish. The scattering model is an extension to axisymmetric finite-length bodies of a two-dimensional general scattering model, called the Fourier matching method (FMM) (DiPerna and Stanton, 1994). It involves conformally mapping the scatterer surface, which can be irregular, to a new coordinate system in which the locus of points describing the radial coordinate being a constant coincides with the scatterer surface. It is a numerically efficient solution that is valid for a wide range of frequencies, over all angles of orientation, for smooth and irregular surfaces, and all scalar boundary conditions.

Chapter 3 describes the experiment and analysis portion of the project. As outlined above, detailed knowledge of the morphology of fish is critical to gaining an accurate knowledge of its scattering properties. Two imaging techniques which are used to exactly measure the morphometry of the scattering features of fish include very high-resolution Phase Contrast X-rays (PCX) and Computerized Tomography (CT) scans, the images from which are incorporated into the FMM scattering model. The results of an extensive, high-quality set of broadband acoustic backscattering measurements conducted on alewife fish over a wide frequency band and over all angles of orientation (1° increments) in two planes of rotation are presented, including the use of both spectral and time-domain analysis techniques to extract unique features from the backscattering acoustic signals from the fish to aid the inference of its acoustic scattering characteristics.

Chapter 4 provides a summary of the thesis, conclusions, a concise list of significant

contributions of the thesis, and recommendations for future work.

A final note about the format of this thesis is in order. Chapters 2 and 3 were written as manuscripts for submission to the Journal of the Acoustical Society of America and were, therefore, written as self-contained articles. Consequently, some discontinuity and redundancy in the thesis is unavoidable; however, such organization involving independent chapters benefits the reader who is interested in only a portion of the thesis.

Chapter 2

Acoustic scattering by axisymmetric finite-length bodies: An extension of a 2-dimensional conformal mapping method[1]

2.1 Introduction

The prediction of acoustic scattering from finite and infinitely long bodies has been pursued for many years, starting with Lord Rayleigh's work on scattering from a sphere (Rayleigh, 1945). Exact analytical solutions to the acoustic wave equation require the

---

[1]This chapter is based on an article submitted to the Journal of the Acoustical Society of America (Reeder and Stanton, submitted).

scatterer's surface to exactly match the locus of all points for which the radial coordinate is a constant. Such exact analytical solutions exist only for a limited number of cases for which the separation of variables is possible (Morse and Feshbach, 1953; Bowman *et al.*, 1987). In all of these cases, the boundary is simple; e.g., a sphere, infinitely long cylinder and prolate spheroid.

For complex shapes, approximate analytical solutions, including the perturbation method, and approximate asymptotic formulations, such as physical optics (Gaunaurd, 1985) and the geometric theory of diffraction (Levy and Keller, 1959; Yamashita, 1990) have been developed. Numerical solutions have also been developed, including the boundary element method (Tobacman, 1984; Francis, 1993), T-matrix (Waterman, 1968; Varadan *et al.*, 1982; Lakhtakia *et al.*, 1984; Hackman and Todoroff, 1985) and the mode matching methods (Yamashita, 1990). All of these approaches are limited in one or more of the following: frequency range, class of surfaces, types of boundary conditions, eccentricity of shape and/or computational implementation and numerical efficiency.

DiPerna and Stanton (1994) introduced a conformal mapping approach to predicting far-field sound scattering by infinitely long cylinders of noncircular cross section. The approach, termed the Fourier Matching Method (FMM), involves a conformal mapping of variables to a new coordinate system in which the constant radial coordinate exactly matches the scatterer surface. The method makes use of the Newton-Raphson algorithm to execute the mapping. The boundary conditions are satisfied by requiring the Fourier coefficients in the new angular variable of the total field to be zero and then the resultant

scattered field is expressed in terms of circular eigenfunctions.

The FMM proved to be accurate over a wide range of frequencies, shapes of cross section, and penetrable (fluid) as well as impenetrable boundary conditions. Furthermore, the approach is inherently numerically efficient due to the nature of its formulation. For example, the FMM was shown by DiPerna and Stanton (1994) to be more efficient than the T-matrix method for the case of the high-aspect-ratio elliptic cylinder because fewer terms were needed for the numerical integrations. Even after incorporating the FMM basis functions into the T-matrix calculations, the FMM required 85% fewer integration points.

A major limitation of the two-dimensional FMM was the fact that it was formulated for the case of an infinitely long cylinder–a two-dimensional scattering solution. Many practical scattering problems involve scattering from finite bodies and cannot be accurately modeled by the two-dimensional solution. In order to address this need, the FMM is extended in this paper to predict the scattering from finite-length bodies. In order for this particular approach to be used for finite bodies, the outer boundary of the bodies must be described by a function rotated about the length-wise axis. Hence, although the function is arbitrary and these bodies are three-dimensional, they are restricted to axisymmetric shapes. As with the two-dimensional formulation, this approach is intrinsically numerically efficient and is valid over a wide range of frequencies and shapes as well as both monostatic and bistatic scattering geometries. The extension has been formulated for three boundary conditions–Dirichlet (soft, or pressure-release), Neumann

(rigid) and Cauchy (fluid). In all three cases, the surrounding material is fluid.

In Section II, the theoretical basis for the formulation is presented, which includes the development of the new orthogonal coordinate system to which the body is mapped, the conformal mapping procedure, modal series solutions to the transformed Helmholtz equation, and resulting equations for the modal series coefficients after satisfying the three boundary conditions. In Section III, several practical numerical issues that arise in the solution of the scattering problem are explored, including the effect of machine precision, truncation of the modal series, and the choice of numerical methods. In Section IV, the numerical results are presented for various shapes (spheres, smooth prolate spheroids and two finite bodies with irregular surfaces), boundary conditions (soft, rigid and fluid), and over a wide range of frequencies and scattering angles. The results are compared with various previously published results using other approaches. Section V contains a summary and concluding remarks.

2.2 Theory

The derivation of the extended formulation for scattering by an axisymmetric finite-length body is conceptually very similar to the corresponding derivation of the two-dimensional solution described by DiPerna and Stanton (1994); in fact, some of the elements are identical. Both solutions begin with the wave equation in a known coordinate system and conformally map the coordinate variables to a new, orthogonal coordinate system in which the locus of all points where the new radial coordinate is a constant exactly

coincides with the scatterer surface. The difference in the coordinate systems between the two cases concerns the fact that one involves two-dimensional coordinates while the other involves an additional coordinate dimension with a new geometry defined for the finite body. Both solutions use mapping functions that are identical in form, transform the Helmholtz equation to the new coordinate system, and then satisfy the boundary conditions using identical techniques to arrive at differing, yet structurally similar, expressions for the scattered pressure. The two-dimensional solution includes a mapping function that corresponds to the shape of the boundary of a cross-sectional slice of the cylinder, while the three-dimensional solution uses a mapping function that corresponds to the shape of the boundary of a *length-wise* slice of the body (specifically, the function that is rotated about the longitudinal axis). Furthermore, the two-dimensional solution includes circular eigenfunctions while the three-dimensional solution for the scattered pressure is expressed in terms of spherical wave functions; i.e., spherical Bessel and Hankel functions and associated Legendre functions. Due to these similarities, the original work will be referred to quite regularly in the development that follows.

Consider the scalar wave equation:

$$\nabla^2 P = \frac{1}{c^2} \frac{\partial^2 P}{\partial t^2} \tag{2.1}$$

where $P(x, y, z)$ is the acoustic pressure in three dimensions, ∇^2 is the Laplacian operator, c is the speed of sound, and t is time. Assuming a harmonic time dependence, $e^{-i\omega t}$, where ω is the angular frequency, the wave equation becomes the scalar Helmholtz differential

31

equation in Cartesian coordinates:

$$\nabla^2 P(x, y, z) + k^2 P(x, y, z) = 0. \qquad (2.2)$$

Here, $k = \omega/c = 2\pi/\lambda$ is the spatially independent acoustic wave number and λ is the acoustic wavelength. In all cases considered here, the body does not support shear waves and is surrounded by a fluid medium. By a conformal (angle- and orientation-preserving) transformation of coordinates, the transformed Helmholtz equation in the new coordinate system becomes:

$$\nabla^2 P(u, w, v) + k^2 F(u, w) P(u, w, v) = 0, \qquad (2.3)$$

where (u, w, v) are the new coordinates, and $F(u, w)$ is a function which depends on the specific transformation (Morse and Feshbach, 1953; DiPerna and Stanton, 1994). With the exception that the wave number is now a function of position, the new Helmholtz equation is formally identical to the Helmholtz equation in Cartesian coordinates.

2.2.1 Conformal mapping

Since x, y and z are mutually orthogonal in the Cartesian coordinate system, conformally mapping them into a new coordinate system guarantees that the new coordinates (u, w, v) will be mutually orthogonal, which eases the computation of the normal particle velocity on the boundary. Additionally, the conformal mapping generates a new set of angular

32

functions which fit the scatterer surface more naturally; that is, points along the surface that change rapidly in (x, y, z) are sampled at a higher spatial rate yet are equally spaced in (u, w, v). A new coordinate system must first be established, and then the conformal mapping function is defined and expanded to provide a method by which the body may be mapped to the new coordinate system.

Orthogonal coordinate system

An orthogonal coordinate system can be generated for a three-dimensional body of revolution from a two-dimensional conformal mapping. Consider the geometry in Fig. 2-1, in which ϕ is the azimuthal angular coordinate ranging from 0 to 2π (measured from the positive x-axis in the xy-plane), θ is the polar angular coordinate ranging from 0 to π (measured from the positive z-axis), and r is the radial coordinate ranging from 0 to ∞. This body is one of revolution that is formed by rotating the contour of the body about the z axis, in the same way that the prolate spheroidal coordinate system is created from an ellipse rotated about the major axis (Flammer, 1957). Consider a new coordinate system whose azimuthal angular coordinate, v, corresponds to ϕ in the original coordinate system. The new polar angular coordinate, w, is measured from the polar axis, z, and ranges from 0 to π, as does the original polar angular coordinate, θ. The scatterer surface in the original coordinate system is defined by the vector, $\vec{r}$, but in the new coordinate system the scatterer surface is defined by the locus of all points where the new radial coordinate is a constant; specifically, $u = 0$. Defining the functions,
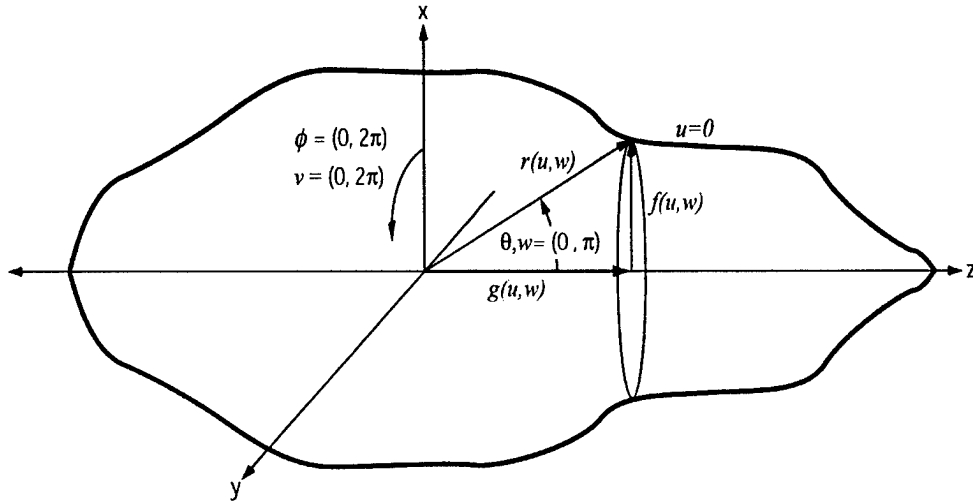
Figure 2-1: Scattering geometry for an irregular, axisymmetric finite-length body. The body is symmetric about the z-axis. The azimuthal angular coordinates, ϕ and v, range from 0 to 2π in the xy-plane, and the polar angular coordinates, θ and w, range from 0 to π, measured from the z-axis. The radial coordinate in the (u, w, v) coordinate system equals zero on the surface. Broadside incidence corresponds to θ=90 degrees. End-on incidence corresponds to 0 and 180 degrees. In the new coordinate system, $g(u,w)$ is the length along the z-axis, and $f(u,w)$ is the projection in the xy-plane.

$f(u, w)$ and $g(u, w)$, of the new coordinate system as shown in Fig. 2-1, trigonometry prescribes dimensions of the body in the x, y and z directions to be:

$$x(u, w, v) = f(u, w) \cos(v) \tag{2.4}$$

$$y(u, w, v) = f(u, w) \sin(v) \tag{2.5}$$

$$z(u, w, v) = g(u, w). \tag{2.6}$$

The position vector, $\vec{r}$, is defined in the new coordinate system by:

$$\vec{r}(u, w, v) = x(u, w, v)\widehat{i} + y(u, w, v)\widehat{j} + z(u, w, v)\widehat{k}, \tag{2.7}$$

where $\widehat{i}$, $\widehat{j}$, and $\widehat{k}$ are unit vectors along the coordinate axes. The position vector can be alternatively expressed by substituting Eqs. (2.4)-(2.6) into Eq. (2.7):

$$\vec{r} = f(u, w) \cos(v)\widehat{i} + f(u, w) \sin(v)\widehat{j} + g(u, w)\widehat{k}. \tag{2.8}$$

The local projection of $\vec{r}$ in each of the coordinate directions is given by the partial derivative of $\vec{r}$ with respect to each of the variables:

$$\vec{r}_u = f_u(u, w) \cos(v)\widehat{i} + f_u(u, w) \sin(v)\widehat{j} + g_u(u, w)\widehat{k} \tag{2.9}$$

$$\vec{r}_w = f_w(u, w) \cos(v)\widehat{i} + f_w(u, w) \sin(v)\widehat{j} + g_w(u, w)\widehat{k} \tag{2.10}$$

$$\vec{r}_v = -f(u,w)\sin(v)\hat{i} + f(u,w)\cos(v)\hat{j}, \tag{2.11}$$

where the subscript denotes the variable with respect to which the partial derivative is taken.

As mentioned earlier, an orthogonal coordinate system is desirable since it facilitates the computation of the normal particle velocity on the boundary necessary for satisfying the boundary conditions, and more naturally fits the scatterer surface. An orthogonal coordinate system requires the following condition to be satisfied:

$$\vec{r}_u \cdot \vec{r}_v = 0 \tag{2.12}$$

$$\vec{r}_w \cdot \vec{r}_v = 0 \tag{2.13}$$

$$\vec{r}_u \cdot \vec{r}_w = 0, \tag{2.14}$$

which can be expanded as:

$$f_u(u,w)f(u,w)\cos(v)\sin(v)(-1+1) = 0 \tag{2.15}$$

$$f_w(u,w)f(u,w)\cos(v)\sin(v)(-1+1) = 0 \tag{2.16}$$

$$f_u(u,w)f_w(u,w)(\cos^2(v) + \sin^2(v)) + g_u(u,w)g_w(u,w) = 0. \tag{2.17}$$

The first two conditions are automatically satisfied. The third condition simplifies to:

$$f_u(u, w)f_w(u, w) + g_u(u, w)g_w(u, w) = 0, \qquad (2.18)$$

which will be satisfied if:

$$f_u(u, w) = g_w(u, w) \qquad (2.19)$$

and

$$f_w(u, w) = -g_u(u, w). \qquad (2.20)$$

These are precisely the Cauchy-Riemann equations for an analytic function (Hildebrand, 1964). Therefore, if $f(u, v)$ and $g(u, v)$ are chosen to be harmonic, then the Cauchy-Riemann conditions will be satisfied, making them analytic functions which represent a conformal transformation. A shape initially plotted in the (x, y, z) coordinate system will be transformed into a shape in the (u, w, v) coordinate system with changes in position and size while preserving angles and proportions (Morse and Feshbach, 1953). Orthogonality of the coordinate system as well as the form of the Helmholtz equation will be preserved (Strang, 1986).

Mapping function

As discussed above, a conformal mapping function must be developed to map the scatterer from the old coordinate system to the new orthogonal, axisymmetric coordinate system just developed. It must be noted at this point that, to the authors' knowledge, a

37

general three-dimensional mapping does not exist in the field of mathematics. Due to the fact that conformal mappings are currently limited to two dimensions, the geometry for the finite body must be axisymmetric about one of the axes, using the two-dimensional function that is to be conformally mapped to form the body by revolution about the axis. The particular mapping used herein is a two-dimensional mapping developed by DiPerna and Stanton (1994) extended to a finite body of revolution which is axisymmetric about the longitudinal axis. The infinitely long cylindrical geometry in DiPerna and Stanton (1994) was described in circular cylindrical coordinates with the radial coordinate, r, being a function of θ, the azimuthal angular coordinate ranging from 0 to 2π. The conformal mapping in that case applied to the function, $r(\theta)$, which corresponded to the shape of the boundary of a cross-sectional slice. In this work, θ is now the *polar* angular coordinate ranging from 0 to π, and ϕ is the azimuthal angular coordinate ranging from 0 to 2π. The function, $r(\theta)$, and associated conformal mapping is now associated with the shape of the boundary of a *length-wise* slice.

The category of surfaces described by Eqs. (2.4)-(2.6) has the additional limitation that r be single-valued; i.e., there can be only one value of r for each w. Following DiPerna and Stanton (1994), the mapping procedure for the axisymmetric finite body is commenced by expanding r in a Fourier series relative to the polar angle, θ, shown in Fig. 2-1:

$$r(\theta) = a + \sum_{n=1}^{\infty}[r_n^c \cos(n\theta) + r_n^s \sin(n\theta)], \tag{2.21}$$

where a is the average radius of the body and r_n^c and r_n^s are the usual Fourier series

coefficients that in this case correspond to the deviation of the surface from the shape of a circle. Note that the series requires more terms to converge for a high aspect ratio (ratio of length to width) prolate spheroid compared to the Fourier series for a shape that varies little from the shape of a circle. Rewriting the $\cos(n\theta)$ and $\sin(n\theta)$ functions in terms of exponentials and using the expression:

$$R_n \equiv \frac{1}{2}[r_n^c + ir_n^s], \tag{2.22}$$

gives

$$re^{i\theta} = ae^{i\theta} + \sum_{n=1}^{\infty}[R_n^* e^{i(1+n)\theta} + R_n e^{i(1-n)\theta}]. \tag{2.23}$$

For a conformal mapping from the (x, y, z) coordinate system to the new coordinate system in (u, w, v):

$$M(\rho) = M(u + iw), \tag{2.24}$$

where $M(\rho)$ is the analytic mapping function in terms of u, the radial variable, and w, the polar angular variable, and ρ is the distance between the axis and outer boundary (i.e., the radius of a given cross-sectional slice). It is desirable to make scattering predictions using this model without inversely mapping the results of this model back to the original coordinate system. The potentially difficult inverse mapping is avoided by choosing $M(\rho)$ such that the coordinate system becomes spherical as the radial coordinate is increased. While the choice of such a mapping function allows predictions of this model to be easily compared to existing solutions, it restricts direct comparisons to the far-

39

field. The general approach can certainly be used in the near-field, but comparisons of near-field scattering between this formulation and other solutions would require an inverse mapping. Note also that there will be two different mapping functions: $G(\rho)$ for the exterior problem and $T(\rho)$ for the interior problem. For the interior problem, $T(\rho)$ is chosen such that the coordinate system becomes spherical as the radial coordinate is decreased.

For the exterior problem, $G(\rho)$ must be chosen such that:

(1) As $u \to \infty$, the coordinate system becomes spherical,

(2) the transformed Helmholtz equation is solvable, and

(3) $u = 0$ is the scatterer surface.

The first two conditions can be satisfied by choosing the form of the exterior mapping function (DiPerna and Stanton, 1994) to be:

$$G(\rho) = c_{-1}e^{\rho} + \sum_{n=0}^{\infty} c_n e^{-n\rho}, \qquad (2.25)$$

which can be decomposed into the complex components:

$$g(u,w) \equiv \text{Re}(G(\rho)) = c_{-1}e^{u}\cos(w) + \sum_{n=0}^{\infty} c_n e^{-nu}\cos(nw) \qquad (2.26)$$

and

$$f(u,w) \equiv \text{Im}(G(\rho)) = c_{-1}e^{u}\sin(w) + \sum_{n=0}^{\infty} c_n e^{-nu}\sin(nw). \qquad (2.27)$$

The coefficients of the mapping function must be chosen such that $u = 0$ defines the

40

scatterer surface in the new coordinate system. Setting the surface, as represented in the two coordinate systems, equal to one another with $u = 0$ gives:

$$G(\rho)|_{u=0} = c_{-1}e^{iw} + \sum_{n=0}^{\infty} c_n e^{-inw}, \qquad (2.28)$$

and substituting further from Eq. (2.23):

$$ae^{i\theta} + \sum_{n=1}^{\infty}[R_n^* e^{i(1+n)\theta} + R_n e^{i(1-n)\theta}] = c_{-1}e^{iw} + \sum_{n=0}^{\infty} c_n e^{-inw}. \qquad (2.29)$$

Since the left-hand side contains positive and negative frequency components while the right-hand side contains only negative frequency components (with the exception of $c_{-1}e^{iw}$), θ and w are not equal; therefore, it is necessary to determine the extent to which θ depends on w. Since it was assumed earlier that the surface is periodic and can be represented as a Fourier series, the deviation of θ from w will be periodic and can be represented as a Fourier series. Specifically, assume:

$$\theta(w) = w + \sum_{l=1}^{\infty}[\delta_l^c \cos(lw) + \delta_l^s \sin(lw)]. \qquad (2.30)$$

The conformal mapping relies on the choice of δ_l^c and δ_l^s such that Eq. (2.29) is satisfied. Using the orthogonality relationships of complex exponential functions, multiplying both

sides by $(1/2\pi)e^{-ijw}$ and integrating over w from 0 to 2π:

$$\frac{1}{2\pi}\int_0^{2\pi} e^{-ijw}\left(ae^{i\theta(w)} + \sum_{n=1}^{\infty}[R_n^*e^{i(1+n)\theta(w)} + R_ne^{i(1-n)\theta(w)}]\right)dw = \left\{\begin{array}{ll} 0, & j > 1 \\ c_j, & j \leq 1 \end{array}\right\},$$

(2.31)

where j is an integer. This set of nonlinear constraints is identical in form to that of DiPerna and Stanton (1994) and is solved by use of an extension of the Newton-Raphson method, the details of which are laid out in Appendix A of DiPerna and Stanton (1994). Note, however, that even though the integral in Eq. (2.31) is performed from 0 to 2π, w is defined in the scattering geometry from 0 to π only (not 2π). Consequently, the mapping coefficients are computed based on the periodic extension from 0 to 2π, but only half of them are used. The upper result in the right hand side of Eq. (2.31) is used to solve for the values of δ_l^c and δ_l^s, which are then used to solve for the mapping coefficients, c_n, through use of the lower result in the right hand side of Eq. (2.31).

The uniqueness of the transformation is tested by verifying that the Jacobian of the transformation is nonzero. This ensures that there exists only one (x, z) for each (u, w). Specifically:

$$|G'(\rho)|^2 \neq 0, \qquad u \geq 0.$$

(2.32)

The interior mapping procedure is identical to the exterior mapping procedure with the exception that the interior mapping function, $T(\rho)$, is different from $G(\rho)$; specifically, $T(\rho)$ is chosen such that the coordinate system becomes spherical as the radial

42

coordinate is decreased. The remaining two conditions mentioned above in the choice of $G(\rho)$ remain the same for the interior problem. These conditions are satisfied by:

$$T(\rho) = \sum_{n=0}^{\infty} t_n e^{n\rho}.$$

(2.33)

To summarize, the procedure described above to conformally map the scatterer shape from the original coordinate system to a new coordinate system is identical in form to the procedure presented in DiPerna and Stanton (1994). In this study, the same mapping procedure is extended to a different (finite-length, axisymmetric) scattering geometry; specifically, it is extended to the shape of the boundary in the length-wise slice. The results of this mapping will be used in solving the Helmholtz equation in three-dimensions in the next section.

2.2.2 Solutions to the Helmholtz equation

The 3-dimensional Helmholtz equation from Eq. (2.2) in spherical coordinates is:

$$\nabla^2 P(r, \theta, \phi) + k^2 P(r, \theta, \phi) = 0,$$

(2.34)

the general solution to which is:

$$P^{ext}(r,\theta,\phi) = \sum_{n=-\infty}^{\infty}\sum_{m=-\infty}^{\infty} a_{nm}j_n(kr)P_n^m(\cos(\theta))e^{im\phi} \tag{2.35}$$

$$+ \sum_{n=-\infty}^{\infty}\sum_{m=-\infty}^{\infty} b_{nm}h_n^{(1)}(kr)P_n^m(\cos(\theta))e^{im\phi},$$

where $j_n(kr)$ is the spherical Bessel function of the first kind of order n, $h_n^{(1)}(kr)$ is the spherical Hankel function of the first kind of order n, and $P_n^m(\cos(\theta))$ is the associated Legendre function of degree n and order m. The radial coordinate is r, the polar angular coordinate is θ, and the azimuthal angular coordinate is ϕ. The scattered field coefficients, b_{nm}, are to be determined by satisfying the boundary conditions using the known coefficient, a_{nm}, of the incident plane wave field traveling from the θ_0 direction:

$$a_{nm} = i^n \epsilon_m (2n+1)\frac{\Gamma(n-m+1)}{\Gamma(n+m+1)}P_n^m(\cos(\theta_0)), \tag{2.36}$$

where ϵ_m is the Neumann factor, Γ is the gamma function, and θ_0 is the angle of incidence of the incident wave relative to the z-axis.

$P^{ext}(r,\theta,\phi)$ is the total pressure external to the scatterer in the original coordinate system (i.e. before transformation): the first term in Eq. (2.35) represents the incident pressure and the second term represents the scattered pressure. Quantities in the original coordinate system can be expressed in terms of the new coordinate system defined in Sec. II.A.1 and Fig. 2-1:

$$\phi = v \tag{2.37}$$

44

$$r(u, w) = \sqrt{f^2(u, w) + g^2(u, w)} \tag{2.38}$$

$$\cos(\theta(u, w)) = \frac{g(u, w)}{r(u, w)}. \tag{2.39}$$

Using these relations, the conformal mapping transforms the Helmholtz equation (Eq. (2.34)) into:

$$\nabla^2 P(u, w, v) + k^2 F(u, w) P(u, w, v) = 0, \tag{2.40}$$

the solution to which is:

$$\begin{aligned} P^{ext}(u, w, v) &= \sum_{n=-\infty}^{\infty} \sum_{m=-\infty}^{\infty} a_{nm} j_n(kr(u, w)) P_n^m \left(\frac{g(u, w)}{r(u, w)} \right) e^{imv} \\ &+ \sum_{n=-\infty}^{\infty} \sum_{m=-\infty}^{\infty} b_{nm} h_n^{(1)}(kr(r, w)) P_n^m \left(\frac{g(u, w)}{r(u, w)} \right) e^{imv}, \end{aligned} \tag{2.41}$$

which is now the expression for the total far-field pressure in the new coordinate system as the sum of the incident and scattered pressure fields, respectively.

The procedure to determine the pressure field inside the scatterer is identical in nature to the exterior problem, but since there is a different mapping function for the interior problem, there will be a Helmholtz equation that is identical in form, but incorporates a different wave number, k_1, to accurately characterize the material properties of the scatterer's interior. The expression for the interior pressure field becomes:

$$P^{int}(u, w, v) = \sum_{n=-\infty}^{\infty} \sum_{m=-\infty}^{\infty} l_{nm} j_n(k_1 r(u, w)) P_n^m \left(\frac{g(u, w)}{r(u, w)} \right) e^{imv}, \tag{2.42}$$

45

where l_{nm} are the internal field coefficients. Only the spherical Bessel function is included in the expression for the internal field since the spherical Hankel function becomes infinite at the origin.

In the limit of great distances from the scatterer, the coordinate system becomes spherical and the asymptotic form of the Hankel function varies inversely with distance. The scattered pressure (the second term in Eq. (2.41)) in this far-field limit has the form:

$$P^{scat} \underset{u\to\infty}{\to} P^{inc}\frac{e^{ikr}}{r}f_s, \tag{2.43}$$

where the scattering amplitude, f_s, having units of length, is a measure of the efficiency with which an object scatters sound and is a function of the object's size, shape, orientation, material properties and the wavelength of the incident wave. The far-field scattering amplitude is given in general form as:

$$f_s = \sum_{n=-\infty}^{\infty} \sum_{m=-\infty}^{\infty} b_{nm} i^{-n-1} P_n^m \left(\frac{g(u,w)}{r(u,w)}\right) e^{imv}. \tag{2.44}$$

The far-field scattered energy evaluated in the backscatter direction is often expressed in terms of the target strength (TS) with units of decibels (dB) relative to 1 m (Urick, 1983), which is given by:

$$TS = 10 \log \sigma_{bs} = 10 \log |f_{bs}|^2, \tag{2.45}$$

where f_{bs} is the far-field scattering amplitude evaluated in the backscattering direction, and $\sigma_{bs} = |f_{bs}|^2$ is the differential backscattering cross section, which differs from the often-used backscattering cross section σ by a factor of 4π ($\sigma = 4\pi\sigma_{bs}$). In order to compare scattering from objects of different sizes but similar proportions, target strength is often normalized by the the square of some typical dimension. Using the length (L) of the elongated scatterer as the normalization constant, the "reduced" target strength (RTS) is:

$$RTS = 10\log\left(\frac{\sigma_{bs}}{L^2}\right) = 10\log|f_{bs}|^2 - 10\log(L^2) = 10\log\left|\frac{f_{bs}}{L}\right|^2. \qquad (2.46)$$

In the case of a sphere, the target strength is normalized by πa^2 instead of L^2. An alternative expression often used to represent the energy scattered in three dimensions is the normalized, steady-state pressure amplitude, or form function, defined by Neubauer, 1986:

$$f_\infty = \frac{2}{a}f_s. \qquad (2.47)$$

To summarize, a new orthogonal coordinate system has been established to which the original coordinate system is mapped via a conformal mapping function. The scatterer surface in the new coordinate system is defined by the locus of all points where the radial coordinate is a constant. The solution to the Helmholtz equation in the new coordinate system will have the same form as the original solution, but with new coordinates using the realizations of Eqs. (2.37) - (2.39). This can be confirmed by inspecting the case

47

of the exterior field for the spherical scatterer: $r(u,w) = c_{-1}e^u$, $\theta(u,w) = w$ and $\phi = v$, resulting in the same solution as in spherical coordinates using separation of variables. Also, for the case far ($u \to \infty$) from the non-spherical scatterer: $r(u,w) \to c_{-1}e^u$, $\theta(u,w) \to w$ and $\phi = v$, resulting in the same solution as in spherical coordinates in the far-field. Equations (2.41) and (2.42) are a general solution for the total pressure in the case of acoustic scattering from a finite-length, axisymmetric body for all frequencies, all angles (bistatic scattering) and for impenetrable (soft and rigid) and penetrable (fluid) boundary conditions. All the quantities needed to satisfy soft, hard and fluid boundary conditions have now been established. Each boundary condition generates a different set of modal series coefficients, b_{nm}, which are used in Eq. (2.44) to compute the far-field scattering amplitude. These coefficients will be determined for three boundary conditions in the following section.

2.2.3 Boundary conditions

The solution for the scattered field in Eqs. (2.41) and (2.44) depends on the boundary conditions. For each boundary condition, there is a different set of scattered field coefficients, b_{nm}, which needs to be evaluated. These coefficients are determined in the normal approach in which the pressures and/or velocities are matched at the boundaries. This matching is specific to the material properties on each side of the boundary. For each of the different boundary conditions, expressions are derived in the following sections for b_{nm}, all of which are in terms of the parameters of the new coordinate system.

The challenge presented by an irregular body is finding a solution to a system of equations in order to satisfy the boundary conditions; specifically, a set of functions, $\psi(w)$, must be determined by which the basis functions are multiplied to generate the system of equations. For a separable geometry, $\psi(w)$ is chosen to be the angular eigenfunction to yield a closed-form solution based on the orthogonality of the eigenfunctions. In the case of irregular surfaces that do not conform to coordinate surfaces, a set of functions, $\psi(w)$, must be chosen to solve the system of equations. DiPerna and Stanton (1994) chose the eigenfunctions in the new (cylindrical) coordinate system, $\psi_m = e^{-imv}$. It is in this choice of eigenfunctions that the FMM derives its name. Without the conformal change of variables to (u, w, v), this choice of functions would not be possible. For the three-dimensional case, the eigenfunctions in the spherical coordinate system are chosen; specifically (Morse and Feshbach, 1953):

$$\psi_n^m = P_n^m(\cos(w)) \sin(w) e^{-imv}. \tag{2.48}$$

Using this choice for ψ, a system of equations is generated to satisfy each of the boundary conditions discussed herein (soft, rigid and fluid). The system of equations is solved for the scattered field coefficients, b_{nm}, which are then used in Eq. (2.44) to determine the far-field scattering amplitude.

Dirichlet boundary conditions

For soft (pressure release or Dirichlet) boundary conditions, the total pressure vanishes on the surface of the scatterer; i.e., $P^{ext}(u_0, w, v) = 0$. Using Eq. (2.41), the series solution for the total exterior pressure field evaluated at the boundary with pressure release boundary conditions is set equal to zero:

$$\sum_{n=-\infty}^{\infty} \sum_{m=-\infty}^{\infty} a_{nm} j_n(kr(u_0, w)) P_n^m \left(\frac{g(u_0, w)}{r(u_0, w)} \right) e^{imv} \tag{2.49}$$

$$+ \sum_{n=-\infty}^{\infty} \sum_{m=-\infty}^{\infty} b_{nm} h_n^{(1)}(kr(u_0, w)) P_n^m \left(\frac{g(u_0, w)}{r(u_0, w)} \right) e^{imv} = 0.$$

The system of equations necessary to satisfy this boundary condition is generated by multiplying both sides of this equation by ψ_n^m from Eq. (2.48) and integrating over the range of w and v (Morse and Feshbach, 1953):

$$\int_0^\pi \int_0^{2\pi} \left\{ \left(\sum_{n=-\infty}^{\infty} \sum_{m=-\infty}^{\infty} a_{nm} j_n \left(kr \left(u_0, w \right) \right) P_n^m \left(\frac{g \left(u_0, w \right)}{r \left(u_0, w \right)} \right) e^{imv} \right. \right.$$

$$\left. + \sum_{n=-\infty}^{\infty} \sum_{m=-\infty}^{\infty} b_{nm} h_n^{(1)} \left(kr \left(u_0, w \right) \right) P_n^m \left(\frac{g \left(u_0, w \right)}{r \left(u_0, w \right)} \right) e^{imv} \right) \tag{2.50}$$

$$\times P_n^m \left(\cos \left(w \right) \right) \sin \left(w \right) e^{-imv} \right\} \, dv dw = 0.$$

Performing the integration on v gives:

$$\sum_{n=-\infty}^{\infty} a_{nm} \int_0^\pi \left(j_n(kr(u_0, w)) P_n^m \left(\frac{g(u_0, w)}{r(u_0, w)} \right) P_n^m(\cos(w)) \sin(w) \right) dw \tag{2.51}$$

50

$$+ \sum_{n=-\infty}^{\infty} b_{nm} \int_0^{\pi} \left(h_n^{(1)}(kr(u_0,w)) P_n^m \left(\frac{g(u_0,w)}{r(u_0,w)} \right) P_n^m(\cos(w)) \sin(w) \right) dw = 0,$$

for each azimuthal order m. This system of equations for pressure release boundary conditions can be written in compact form:

$$\sum_{n=-\infty}^{\infty} a_{nm} R_n^m + \sum_{n=-\infty}^{\infty} b_{nm} Q_n^m = 0, \tag{2.52}$$

where a_{nm} is given in Eq. (2.36), and R_n^m and Q_n^m are defined, using Eq. (2.51) as:

$$R_n^m \equiv \int_0^{\pi} \left(j_n(kr(u_0,w)) P_n^m \left(\frac{g(u_0,w)}{r(u_0,w)} \right) P_n^m(\cos(w)) \sin(w) \right) dw \tag{2.53}$$

$$Q_n^m \equiv \int_0^{\pi} \left(h_n^{(1)}(kr(u_0,w)) P_n^m \left(\frac{g(u_0,w)}{r(u_0,w)} \right) P_n^m(\cos(w)) \sin(w) \right) dw. \tag{2.54}$$

Using Eq. (2.52), the series coefficient, b_{nm}, for the far-field scattered field due to a soft boundary is:

$$b_{nm} = - \left(Q_n^m \right)^{-1} R_n^m a_{nm}. \tag{2.55}$$

Neumann boundary conditions

With rigid, or Neumann, boundary conditions, the normal particle velocity vanishes on the scatterer surface; i.e., $\widehat{n} \cdot \nabla P^{ext}(u_0, w, v) = 0$, where $\widehat{n}$ is the unit vector normal to the surface and ∇ is the gradient operator. The method to solve for b_{nm} is broadly similar to the previous case, although several new terms are necessary to satisfy this particular boundary condition. The unit vectors in the u, v, and w directions are (Hildebrand,

51

1964):

$$\widehat{a}_u = \frac{\overrightarrow{r}_u}{|\overrightarrow{r}_u|} \tag{2.56}$$

$$\widehat{a}_w = \frac{\overrightarrow{r}_w}{|\overrightarrow{r}_w|} \tag{2.57}$$

$$\widehat{a}_v = \frac{\overrightarrow{r}_v}{|\overrightarrow{r}_v|}. \tag{2.58}$$

Using Eqs. (2.9) - (2.11), the scale factors of each of the new coordinates (Morse and Feshbach, 1953) can be rewritten using the new coordinates:

$$h_u = |\overrightarrow{r}_u| = \sqrt{f_u^2(u,w) + g_u^2(u,w)} = \sqrt{f_u^2(u,w) + f_w^2(u,w)} \tag{2.59}$$

$$h_w = |\overrightarrow{r}_w| = \sqrt{f_w^2(u,w) + g_w^2(u,w)} = \sqrt{f_w^2(u,w) + f_u^2(u,w)} \tag{2.60}$$

$$h_v = |\overrightarrow{r}_v| = f(u,w). \tag{2.61}$$

Note that

$$h_u(u,w) = h_w(u,w) = h(u,w). \tag{2.62}$$

In the new coordinate system, the unit vectors become:

$$\widehat{a}_u = \frac{f_u(u,w)}{h(u,w)}\cos(v)\widehat{i} + \frac{f_u(u,w)}{h(u,w)}\sin(v)\widehat{j} + \frac{g_u(u,w)}{h(u,w)}\widehat{k} \tag{2.63}$$

$$\widehat{a}_w = \frac{f_w(u,w)}{h(u,w)}\cos(v)\widehat{i} + \frac{f_w(u,w)}{h(u,w)}\sin(v)\widehat{j} + \frac{g_w(u,w)}{h(u,w)}\widehat{k} \tag{2.64}$$

$$\widehat{a}_v = -\sin(v)\widehat{i} + \cos(v)\widehat{j}. \tag{2.65}$$

The scatterer surface has been defined by $u = u_0$; therefore, $\widehat{n} = \widehat{a}_u$. The gradient of P is:

$$\nabla P(u,w,v) = \frac{1}{h_u(u,w)}\frac{\partial P}{\partial u}\widehat{a}_u + \frac{1}{h_w(u,w)}\frac{\partial P}{\partial w}\widehat{a}_w + \frac{1}{h_v(u,w)}\frac{\partial P}{\partial v}\widehat{a}_v. \tag{2.66}$$

Using $\widehat{n} = \widehat{a}_u$ and $h_u(u,w) = \sqrt{f_w^2(u,w) + f_u^2(u,w)}$:

$$\widehat{n}\cdot\nabla P(u,w,v) = \frac{1}{\sqrt{f_w^2(u,w) + f_u^2(u,w)}}\frac{\partial P}{\partial u}. \tag{2.67}$$

Using Eq. (2.41), the series solution for the normal particle velocity of the total external field for rigid boundary conditions evaluated at the boundary is set equal to zero:

$$\widehat{n}\cdot\nabla\left(\sum_{n=-\infty}^{\infty}\sum_{m=-\infty}^{\infty} a_{nm}j_n\left(kr\left(u_0,w\right)\right)P_n^m\left(\frac{g\left(u_0,w\right)}{r\left(u_0,w\right)}\right)e^{imv}\right) \tag{2.68}$$

$$+\widehat{n}\cdot\nabla\left(\sum_{n=-\infty}^{\infty}\sum_{m=-\infty}^{\infty} b_{nm}h_n^{(1)}\left(kr\left(u_0,w\right)\right)P_n^m\left(\frac{g\left(u_0,w\right)}{r\left(u_0,w\right)}\right)e^{imv}\right) = 0.$$

The system of equations necessary to satisfy this boundary condition is generated by multiplying both sides of the equation by ψ_n^m in Eq (2.48) and integrating over the range

of w and v:

$$\int_0^\pi \int_0^{2\pi} \left\{ \left(\widehat{n} \cdot \nabla \left(\sum_{n=-\infty}^\infty \sum_{m=-\infty}^\infty a_{nm} j_n \left(kr \left(u_0, w \right) \right) P_n^m \left(\frac{g \left(u_0, w \right)}{r \left(u_0, w \right)} \right) e^{imv} \right) \right. \right.$$

$$\left. \left. + \widehat{n} \cdot \nabla \left(\sum_{n=-\infty}^\infty \sum_{m=-\infty}^\infty b_{nm} h_n^{(1)} \left(kr \left(u_0, w \right) \right) P_n^m \left(\frac{g \left(u_0, w \right)}{r \left(u_0, w \right)} \right) e^{imv} \right) \right) \right. \quad (2.69)$$

$$\left. \times P_n^m(\cos(w)) \sin(w) e^{-imv} \right\} \, dv \, dw = 0.$$

Using Eq. (2.67) and performing the integration on v gives:

$$\sum_{n=-\infty}^\infty a_{nm} \int_0^\pi \left(j_n(kr(u_0, w)) P_{n,u}^m \left(\frac{g(u_0, w)}{r(u_0, w)} \right) \frac{r(u_0, w) g_u(u_0, w) - g(u_0, w) r_u(u_0, w)}{r^2(u_0, w)} \right.$$

$$(2.70)$$

$$\left. + j_{n,u}(kr(u_0, w)) P_n^m \left(\frac{g(u_0, w)}{r(u_0, w)} \right) kr_u(u_0, w) \right) \frac{P_n^m(\cos(w))}{\sqrt{f_w^2(u_0, w) + f_u^2(u_0, w)}} \sin(w) dw$$

$$+ \sum_{n=-\infty}^\infty b_{nm} \int_0^\pi \left(h_n^{(1)}(kr(u_0, w)) P_{n,u}^m \left(\frac{g(u_0, w)}{r(u_0, w)} \right) \frac{r(u_0, w) g_u(u_0, w) - g(u_0, w) r_u(u_0, w)}{r^2(u_0, w)} \right.$$

$$\left. + h_{n,u}^{(1)}(kr(u_0, w)) P_n^m \left(\frac{g(u_0, w)}{r(u_0, w)} \right) kr_u(u_0, w) \right) \frac{P_n^m(\cos(w))}{\sqrt{f_w^2(u_0, w) + f_u^2(u_0, w)}} \sin(w) dw = 0,$$

where, as with the other terms, the subscript, u, also indicates the partial derivative of the Legendre functions with respect to u.

As in the previous section, the system of equations for rigid boundary conditions can be written in compact form:

$$\sum_{n=-\infty}^\infty a_{nm} R_n'^m + \sum_{n=-\infty}^\infty b_{nm} Q_n'^m = 0, \quad (2.71)$$

54

where a_{nm} is given in Eq. (2.36), $R_n'^m$ is the integral in the first half of Eq. (2.70), and $Q_n'^m$ is the integral in the second half of Eq. (2.70). Using Eq. (2.71), the series coefficient, b_{nm}, for the far-field scattered field due to a rigid boundary is:

$$b_{nm} = -\left(Q_n'^m\right)^{-1} R_n'^m a_{nm}. \tag{2.72}$$

Cauchy boundary conditions

Fluid (Cauchy) boundary conditions is the case in which the body consists of a fluid with material properties other than that of the surrounding fluid; that is, the body does not support a shear wave. In this case, the exterior and interior pressure fields and normal components of particle velocity are required to be equal on the surface. The fluid boundary conditions take the form:

Pressure:

$$
\begin{aligned}
&\sum_{n=-\infty}^{\infty} \sum_{m=-\infty}^{\infty} a_{nm} j_n(kr(u_0, w)) P_n^m \left(\frac{g(u_0, w)}{r(u_0, w)}\right) e^{imv} \\
&+ \sum_{n=-\infty}^{\infty} \sum_{m=-\infty}^{\infty} b_{nm} h_n^{(1)}(kr(u_0, w)) P_n^m \left(\frac{g(u_0, w)}{r(u_0, w)}\right) e^{imv} \\
&= \sum_{n=-\infty}^{\infty} \sum_{m=-\infty}^{\infty} l_{nm} j_n(k_1 r(u_0, w)) P_n^m \left(\frac{g(u_0, w)}{r(u_0, w)}\right) e^{imv}
\end{aligned}
\tag{2.73}
$$

Particle Velocity:

55

$$\hat{n} \cdot \nabla \left(\sum_{n=-\infty}^{\infty} \sum_{m=-\infty}^{\infty} a_{nm} j_n(kr(u_0, w)) P_n^m \left(\frac{g(u_0, w)}{r(u_0, w)} \right) e^{imv} \right)$$

$$+ \hat{n} \cdot \nabla \left(\sum_{n=-\infty}^{\infty} \sum_{m=-\infty}^{\infty} b_{nm} h_n^{(1)}(kr(u_0, w)) P_n^m \left(\frac{g(u_0, w)}{r(u_0, w)} \right) e^{imv} \right) \qquad (2.74)$$

$$= \hat{n} \cdot \nabla \left(\sum_{n=-\infty}^{\infty} \sum_{m=-\infty}^{\infty} l_{nm} j_n(k_1 r(u_0, w)) P_n^m \left(\frac{g(u_0, w)}{r(u_0, w)} \right) e^{imv} \right),$$

where l_{nm} are the interior field coefficients. The system of equations necessary to satisfy this boundary condition is generated by multiplying both sides of the equation by ψ_n^m in Eq (2.48) and integrating over the range of w and v:

Pressure:

$$\int_0^\pi \int_0^{2\pi} \left\{ \left(\sum_{n=-\infty}^{\infty} \sum_{m=-\infty}^{\infty} a_{nm} j_n(kr(u_0, w)) P_n^m \left(\frac{g(u_0, w)}{r(u_0, w)} \right) e^{imv} \right. \right. \qquad (2.75)$$

$$\left. + \sum_{n=-\infty}^{\infty} \sum_{m=-\infty}^{\infty} b_{nm} h_n^{(1)}(kr(u_0, w)) P_n^m \left(\frac{g(u_0, w)}{r(u_0, w)} \right) e^{imv} \right)$$

$$\times P_n^m(\cos(w)) \sin(w) e^{-imv} \bigg\} \, dv dw$$

$$= \int_0^\pi \int_0^{2\pi} \left\{ \left(\sum_{n=-\infty}^{\infty} \sum_{m=-\infty}^{\infty} l_{nm} j_n(k_1 r(u_0, w)) P_n^m \left(\frac{g(u_0, w)}{r(u_0, w)} \right) e^{imv} \right) \right.$$

$$\times P_n^m(\cos(w)) \sin(w) e^{-imv} \bigg\} \, dv dw$$

Particle Velocity:

56

$$\int_0^\pi \int_0^{2\pi} \left\{ \left(\widehat{n} \cdot \nabla \left(\sum_{n=-\infty}^{\infty} \sum_{m=-\infty}^{\infty} a_{nm} j_n(kr(u_0,w)) P_n^m \left(\frac{g(u_0,w)}{r(u_0,w)} \right) e^{imv} \right) \right. \right. \tag{2.76}$$

$$\left. + \widehat{n} \cdot \nabla \left(\sum_{n=-\infty}^{\infty} \sum_{m=-\infty}^{\infty} b_{nm} h_n^{(1)}(kr(u_0,w)) P_n^m \left(\frac{g(u_0,w)}{r(u_0,w)} \right) e^{imv} \right) \right)$$

$$\left. \times P_n^m(\cos(w)) \sin(w) e^{-imv} \right\} dv dw$$

$$= \int_0^\pi \int_0^{2\pi} \left\{ \widehat{n} \cdot \nabla \left(\sum_{n=-\infty}^{\infty} \sum_{m=-\infty}^{\infty} l_{nm} j_n(k_1 r(u_0,w)) P_n^m \left(\frac{g(u_0,w)}{r(u_0,w)} \right) e^{imv} \right) \right.$$

$$\left. \times P_n^m(\cos(w)) \sin(w) e^{-imv} \right\} dv dw.$$

Using Eq. (2.67) and performing the integration on v for both Eqs. (2.75) and (2.76) gives:

Pressure:

$$\sum_{n=-\infty}^{\infty} a_{nm} \int_0^\pi j_n(kr(u_0,w)) P_n^m \left(\frac{g(u_0,w)}{r(u_0,w)} \right) P_n^m(\cos(w)) \sin(w) dw$$

$$+ \sum_{n=-\infty}^{\infty} b_{nm} \int_0^\pi h_n^{(1)}(kr(u_0,w)) P_n^m \left(\frac{g(u_0,w)}{r(u_0,w)} \right) P_n^m(\cos(w)) \sin(w) dw \tag{2.77}$$

$$= \sum_{n=-\infty}^{\infty} l_{nm} \int_0^\pi j_n(k_1 r(u_0,w)) P_n^m \left(\frac{g(u_0,w)}{r(u_0,w)} \right) P_n^m(\cos(w)) \sin(w) dw$$

Particle Velocity:

$$\sum_{n=-\infty}^{\infty} a_{nm} \int_0^{\pi} \left(j_n(kr(u_0,w)) P_{n,u}^m \left(\frac{g(u_0,w)}{r(u_0,w)} \right) \frac{r(u_0,w)g_u(u_0,w) - g(u_0,w)r_u(u_0,w)}{r^2(u_0,w)} \right.$$

$$\left. + j_{n,u}(kr(u_0,w)) P_n^m \left(\frac{g(u_0,w)}{r(u_0,w)} \right) kr_u(u_0,w) \right) \frac{P_n^m(\cos(w))}{\sqrt{f_w^2(u_0,w) + f_u^2(u_0,w)}} \sin(w) dw$$

$$+ \sum_{n=-\infty}^{\infty} b_{nm} \int_0^{\pi} \left(h_n^{(1)}(kr(u_0,w)) P_{n,u}^m \left(\frac{g(u_0,w)}{r(u_0,w)} \right) \frac{r(u_0,w)g_u(u_0,w) - g(u_0,w)r_u(u_0,w)}{r^2(u_0,w)} \right.$$

$$(2.78)$$

$$\left. + h_{n,u}^{(1)}(kr(u_0,w)) P_n^m \left(\frac{g(u_0,w)}{r(u_0,w)} \right) kr_u(u_0,w) \right) \frac{P_n^m(\cos(w))}{\sqrt{f_w^2(u_0,w) + f_u^2(u_0,w)}} \sin(w) dw$$

$$= \sum_{n=-\infty}^{\infty} l_{nm} \int_0^{\pi} \left(j_n(k_1 r(u_0,w)) P_{n,u}^m \left(\frac{g(u_0,w)}{r(u_0,w)} \right) \frac{r(u_0,w)g_u(u_0,w) - g(u_0,w)r_u(u_0,w)}{r^2(u_0,w)} \right.$$

$$\left. + j_{n,u}(k_1 r(u_0,w)) P_n^m \left(\frac{g(u_0,w)}{r(u_0,w)} \right) k_1 r_u(u_0,w) \right) \frac{P_n^m(\cos(w))}{\sqrt{f_w^2(u_0,w) + f_u^2(u_0,w)}} \sin(w) dw.$$

Writing Eqs. (2.77) and (2.78) in compact form:

$$\sum_{n=-\infty}^{\infty} a_{nm} R_n^m + \sum_{n=-\infty}^{\infty} b_{nm} Q_n^m = \sum_{n=-\infty}^{\infty} l_{nm} S_n^m \qquad (2.79)$$

$$\sum_{n=-\infty}^{\infty} a_{nm} R_n'^m + \sum_{n=-\infty}^{\infty} b_{nm} Q_n'^m = \sum_{n=-\infty}^{\infty} l_{nm} S_n'^m, \qquad (2.80)$$

where a_{nm} is given in Eq. (2.36); R_n^m, Q_n^m, and S_n^m are the first, second and third integrals in Eq. (2.77); and $R_n'^m$, $Q_n'^m$, and $S_n'^m$ are the first, second and third integrals

in Eq. (2.78). In contrast to the above two cases of impenetrable boundary conditions, b_{nm} must be solved for in two simultaneous equations. Solving for b_{nm} in Eqs (2.79) and (2.80):

$$b_{nm} = -\left(Q_n'^m S_n^m - Q_n^m S_n'^m\right)^{-1}\left(R_n^m S_n'^m - R_n'^m S_n^m\right)a_{nm}. \qquad (2.81)$$

In summary, the far-field scattering amplitude (Eq. (2.44)) of a particular body is determined by conformally mapping the scatterer surface to a new coordinate system by solving Eq. (2.31), then solving for the far-field scattering coefficients, b_{nm}, for the appropriate boundary condition as specified in the equations of this section.

2.3 Numerical implementation

2.3.1 General approach

Prediction of the scattering by an axisymmetric finite-length body using the above formulation requires a series of steps involving numerical methods. Given the complexity of the procedure, it is summarized briefly in this section, with some of the challenges elaborated upon in the next section. The shape of the scatterer is first described by the array of points, (r, θ), in polar coordinates in the (x, z) plane (Fig. 2-1). The terms, r and θ, are then expanded in a Fourier series using Eqs. (2.21) and (2.30). The conformal mapping is based upon determining the values of δ_i^c and δ_i^s, which are determined by solving the upper result in the right hand side of Eq. (2.31). This is a set of nonlinear constraints which are solved in an iterative, numerical manner by an extension of the

Newton-Raphson method. The details of the Newton-Raphson method can be found in the Appendix of DiPerna and Stanton (1994) or in many math texts. Once the values of δ_l^c and δ_l^s are determined, the lower result in the right hand side of Eq. (2.31) is used to determine the mapping coefficients, c_n, which are then used to compute functions, $g(u, w)$ and $f(u, w)$, of the new coordinate system (Eqs. (2.26) and (2.27)). After the values of $g(u, w)$ and $f(u, w)$ are determined, the conformal mapping is complete, and the solution to the Helmholtz equation in the new coordinate system can be determined. The number of terms included in the summations in Eqs. (2.21), (2.30) and (2.31) are chosen in an arbitrary manner and iterated until a sufficient number of terms are used to accurately map the scatterer to the new coordinate system. The mapping can be verified visually by using $g(u, w)$ and $f(u, w)$ to plot on top of the shape in the original coordinate system (Fig. 2-1). In the case of a smooth prolate spheroid, the conformal mapping method can be avoided by using the fact that $f = a\sin(w)$ and $g = b\cos(w)$ in Eqs. (2.26) and (2.27), where a and b are the semi-minor and semi-major axes of the prolate spheroid, respectively. In the new coordinate system, the external far-field pressure (Eq. (2.41)) is solved by use of Eqs. (2.37) - (2.39). For soft boundary conditions, solve Eq. (2.55) by numerical integration of Eqs. (2.53) and (2.54). The numerical integration can be performed by use of one of numerous integration techniques, many of which are described in Press *et al.*, (1992). In this work, simple matrix summation was used. Likewise for rigid and fluid boundary conditions, solve Eqs. (2.72) and (2.81) by performing the numerical integrations in Eq. (2.70) and Eqs. (2.77) - (2.78), respectively. With the

scattered field coefficients, b_{nm}, the far-field scattering amplitude is finally computed Eq. (2.44). The point at which the summations in Eq. (2.44) are truncated is determined in an iterative manner. The issues and challenges involved in truncation and performing the matrix inversions in Eqs. (2.55), (2.72) and (2.81) are discussed in the next section.

2.3.2 Numerical issues

In general, there exist significant inherent difficulties in the numerical implementation of infinite series solutions. For series solutions for simple geometries such as a sphere or cylinder, and with currently available computers, the series converges relatively rapidly. However, as the shape deviates from a simple geometry, higher modes are required for a converged solution. The problem is particularly complicated for objects of high aspect ratio and irregularity (roughness) on the boundary. The accuracy of the solution must be balanced with accounting for the degree of roughness and elongation of the boundary.

Precision

Some of the problem in the numerical calculation of the wave functions is merely the time required for the computer to compute the wave functions. Beyond this issue of time, the limiting factors in the numerical implementation are machine precision and matrix manipulation.

The FMM generates a transition matrix, much like the T-matrix model (Waterman, 1968), that relates the incident field coefficients to the scattered field coefficients. For a

61

spherical scatterer, the transition matrix is diagonal and each non-zero term on the main diagonal is an eigenvalue for each mode computed. If the scatterer shape deviates from spherical, the matrix contains off-diagonal terms. The additional higher modal terms required to represent the scattering become extremely small, falling below the value that can be accurately represented numerically, resulting in a singular matrix in which the true values of its elements are below the precision of the machine. Thus, machine roundoff error is introduced into the solution and quickly dominates the results as it propagates through the solution via repetitive matrix manipulation.

The fundamental problem is the finite machine precision. The number of modes required to accurately represent the scattering involves matrix elements that are numerically smaller than the machine can accurately compute. Little can be done to improve precision since it is a hardware limitation. Future technology may afford greater precision, but the extent to which it improves the solution is difficult to estimate. The relationship between greater precision and increased accuracy in the solution is not necessarily linear, but could be a rapidly decaying one instead.

Besides hardware limitations, numerical accuracy is very dependent upon accurate and efficient numerical implementation of the theory. There are a number of numerical algorithms that improve matrix manipulation and handling of roundoff error that have been investigated in this work, including orthogonal triangular decomposition, LU factorization, balancing of matrices and scaling strategies (Press *et al.*, 1992). The single most important algorithm investigated and used in the implementation of this formulation is

the well-known singular value decomposition (SVD) algorithm (Press *et al.*, 1992).

For an ill-conditioned matrix in which some elements are below machine precision, the SVD algorithm sets those numerically indiscernible elements to zero. Eliminating one or more linear combinations of the set of equations that is to be solved is justified because those subspaces are dominated by roundoff error and contribute negligible energy to the solution and contribute principally to error; indeed, the error can be amplified. Singular values whose ratio to the largest singular value is less than N times the machine precision are set to zero (Press *et al.*, 1992). This threshold value is equivalent to the rank of the matrix, which is an estimate of the number of linearly independent rows or columns of a matrix. Eliminating erroneous subspaces yields a more stable numerical result and a convergent solution at higher frequencies; however, a disadvantage of the method is the potential of removing some energy that contributes to the solution, thereby diminishing the amplitude and structure of the results at higher frequencies. Therefore, the threshold used for SVD must be set with care.

Truncation

Regardless of whether the wave functions are difficult to compute and are susceptible to limitations of machine precision, numerical computation of an infinite series such as in Eqs. (2.41) and (2.44), cannot be performed exactly due to the fact that there are an infinite number of terms. Furthermore, the point at which the series must be truncated is not necessarily obvious. For lower frequencies and smooth spherical or smooth low-

63

aspect-ratio spheroids (i.e., low eccentricity), reaching a converged solution before the onset of singularity is typically not a problem using currently available personal computers. As the frequency, aspect ratios or degree of irregularity are increased, roundoff error begins to increase as a factor in preventing the solution from being converged.

Given the importance of these numerical issues, a study was conducted to explore the conditions under which the solution would be reliable once numerically evaluated. The "performance envelope" of the FMM for broadside backscattering by smooth prolate spheroids of varying aspect ratios for soft and rigid boundary conditions was investigated (Figs. 2-2 and 2-3).

In this study, a "converged" solution is defined as one in which the computation of additional modes does not significantly change the result for a given value of ka. Specifically, the scattering amplitude for a converged solution (although strictly a truncated form of the exact solution) changed by less than 0.1% (an amount chosen arbitrarily in this study) with the computation of additional modes, which correlated very well with visual inspection. "Truncated" and "numerically stable" approximations are less objective and are a relative indication of the degree of reliability. Truncated approximations, as defined in this paper, employ a sufficient number of modes to represent the scattering to a lesser degree of accuracy than the above-defined converged solution, but still generally predicts the overall scattering levels and finer structure. Numerically stable approximations use a sufficient number of modes to adequately represent the overall amplitude, if not the finer structure, of the majority of the scattering. For both the soft (Fig. 2-2)

Soft Spheroid Performance Envelope--Broadside Backscatter

Figure 2-2: Performance envelope for broadside backscatter for a smooth prolate spheroid with soft boundary conditions as a function of ka and aspect ratio. A converged solution is defined in this paper as one in which the computation of additional modes changed the scattering amplitude by less than 0.1% for a given value of ka. As the aspect ratio or value of ka is increased, converged solutions are more difficult to obtain. Aspect ratio (AR) is the ratio of length to width of the prolate spheroid (AR=1 for a sphere). The semi-minor axis of the prolate spheroid is designated as a.
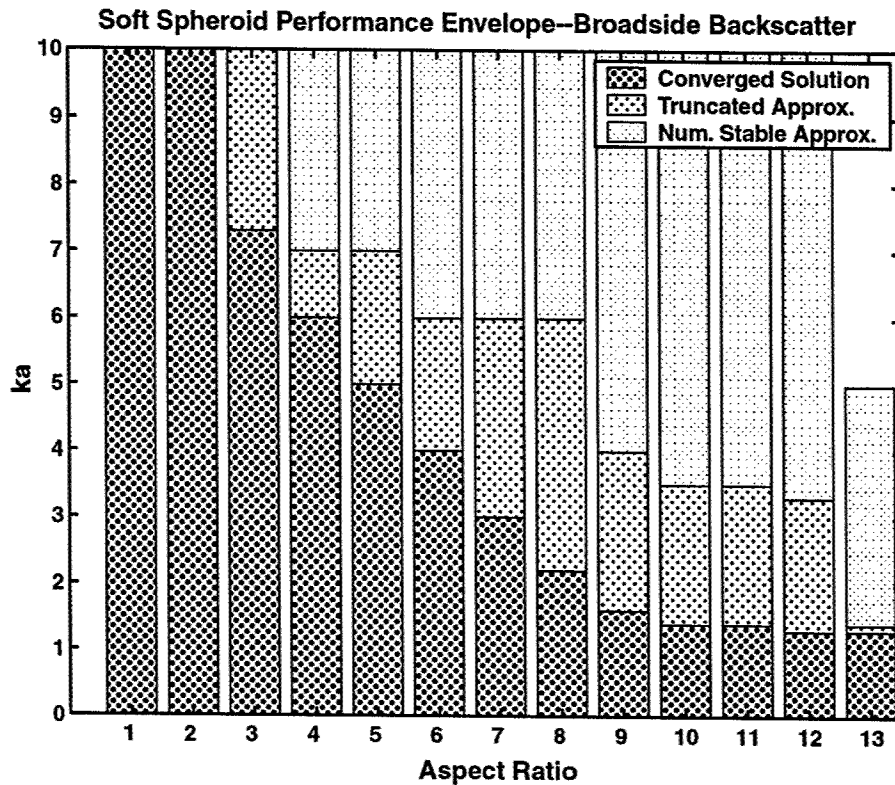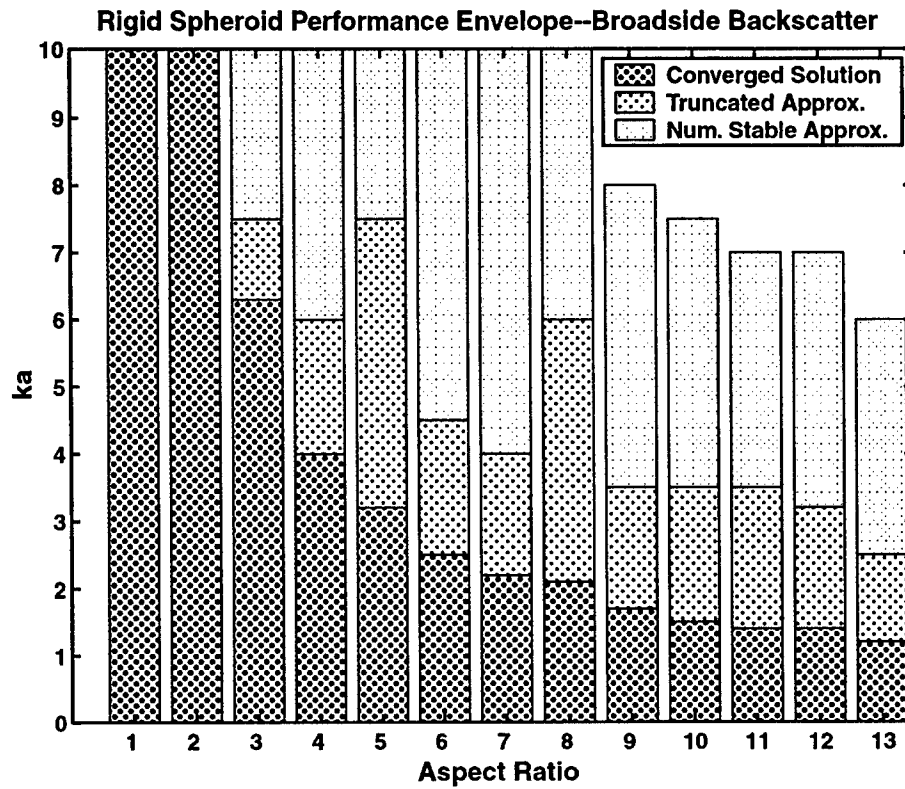
Figure 2-3: Performance envelope for broadside backscatter by a smooth prolate spheroid with rigid boundary conditions as a function of ka and aspect ratio. Converged solutions are defined in the caption of Fig. 2-2.

and rigid (Fig. 2-3) cases, the solution was obtained for prolate spheroids with aspect ratios ranging from 1:1 (i.e., a sphere) to 13:1, and ka ranging from 0 to 10. Note that a is the semi-minor axis of the prolate spheroid, b is the semi-major axis, and the aspect ratio is b/a. This assignment of notation (a and b) differs from that in some literature, as a in this paper is intended to correspond to a cylindrical radius for the elongated bodies. For each of the two boundary conditions, a converged solution is reached for the sphere and 2:1 aspect ratio prolate spheroid for values of ka up to 10. As the aspect ratio is increased beyond 2:1, the value of ka at which the solution is converged falls off rapidly down to levels of 1.3 (soft) and 1.2 (rigid) at an aspect ratio of 13:1. The truncated approximation and numerically stable approximation behave less predictably as a function of ka and aspect ratio, but indicate generally decreasing convergence values of ka with increasing aspect ratio. The value of ka at which a converged solution is reached in the soft case is generally higher than that of the rigid case, particularly for aspect ratios of 8:1 or less. This is consistent with the fact that the soft case does not include an expression for the derivative of pressure as in the rigid case (Eq. (2.67)), thus requiring fewer matrix manipulations that would propagate roundoff error.

2.4 Numerical results

All of the results plotted in Sec. IV were generated using Eqs. (2.44)-(2.47), (2.55), (2.72) and (2.81) to illustrate predictions as well as demonstrate the accuracy of the FMM in a wide variety of applications. Predictions using the FMM are first compared to those

using the exact solution for soft, rigid and fluid spheres. Predictions are then compared between the FMM and various formulations for smooth prolate spheroids for a variety of aspect ratios, frequencies, and incidence and scattering angles. Thirdly, computations are presented for scattering from a realistic, irregular body. Lastly, predictions are presented for scattering by gaseous smooth prolate spheroids in the region of resonance for various aspect ratios.

2.4.1 Spheres: comparison with exact solution

Computing the scattering from the sphere is an essential benchmark for the FMM since the exact solutions exist. The results for the soft, rigid and fluid spheres produced by the FMM are identical to the exact solutions (Anderson, 1950) in all three cases (Fig. 2-4). In the case of fluid boundary conditions, material properties for a weak scatterer (i.e., one having properties resembling that of the surrounding fluid) were used. The specific values were chosen to resemble zooplankton tissue.

2.4.2 Prolate spheroids: comparison with various solutions

As mentioned earlier, accurately computing the scattering from a prolate spheroid is a difficult task, particularly at high aspect ratios and high frequencies. Every scattering model has its strengths and weaknesses, so to thoroughly test the scope of applicability for the FMM, it is compared to a variety of models within their ranges of performance. The approaches used for comparison are the Deformed Finite Cylinder (DFC) model, the T-
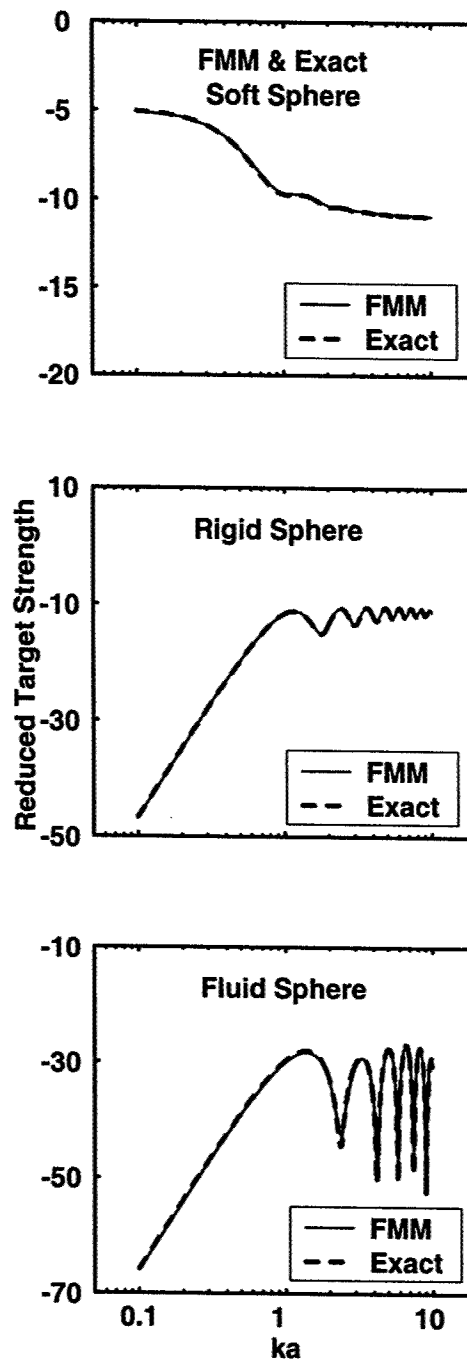
Figure 2-4: FMM and Exact Solutions: Reduced Target Strength as a function of ka for soft, rigid and fluid spheres. Mass and sound speed contrasts for the (weakly scattering) fluid case are $g=1.043$ and $h=1.052$, respectively. Exact solution calculation based on formulation from Anderson (1950).

69

matrix formulation, the Boundary Element Method (BEM), the exact prolate spheroidal solution, and the Kirchhoff approximation.

Deformed finite cylinder model (DFC)

Stanton adapted his formulation for the finite cylinder (Stanton, 1988a, b) to finite cylinders of deformation; e.g., prolate spheroids and uniformly bent finite cylinders (Stanton, 1989a). The model, which is based on the modal series solution for an infinitely long cylinder, has proven to be accurate at broadside and near-broadside orientations to the prolate spheroid for aspect ratios of 5:1 and higher (Partridge and Smith, 1995). The FMM compares well to the DFC for the case of broadside backscatter from a rigid prolate spheroid of aspect ratios 2:1, 5:1 and 10:1 (Fig. 2-5). As the aspect ratio is increased, results for the FMM are limited to lower frequencies to maintain a converged solution. In the Rayleigh region ($ka \leq 1$), the TS increases as expected, proportional to $(ka)^4$. Note also that the agreement between the FMM and the DFC in the Rayleigh region improves as the aspect ratio increases, reflecting the fact that the accuracy of the DFC improves with aspect ratio, eventually coinciding with the FMM results.

T-matrix method

The T-matrix method is a formally exact, numerical solution that has been the focus of much research to date and has proven to be an accurate model for numerous scattering problems. In two earlier studies, the T-matrix approach has been applied to backscatter and bistatic scattering by rigid prolate spheroids with an aspect ratio of 2:1 (Varadan

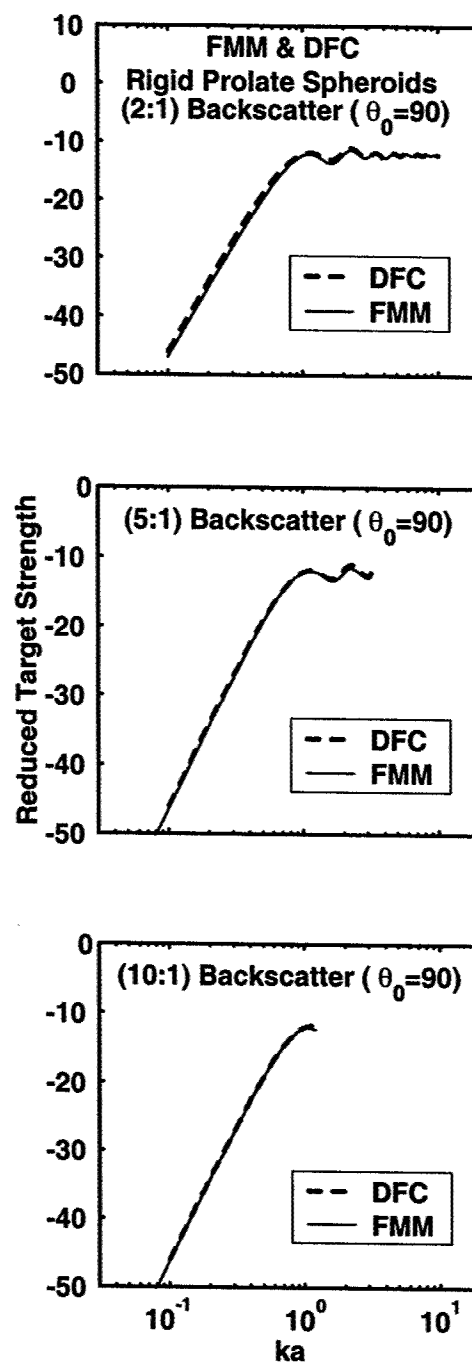Figure 2-5: FMM and DFC: Reduced Target Strength of rigid prolate spheroids at broadside incidence as a function of ka for aspect ratios of 2:1, 5:1 and 10:1. DFC calculations are based on the formulation from Stanton (1989a). The agreement between the FMM and DFC improves as the aspect ratio increases, which is consistent with the fact that the DFC is valid in the limit of high aspect ratio geometries.

71

et al., 1982) and 10:1 (Hackman, 1993) and will be compared with FMM predictions. There is excellent agreement between the FMM and the T-matrix method in the cases of backscatter for a 2:1 aspect ratio prolate spheroid at broadside ($\theta_0 = 90°$) and oblique ($\theta_0 = 45°$) angles of incidence, as well as in the bistatic geometry of broadside incidence ($\theta_0 = 90°$) and end-on reception ($\theta_r = 0°$) (Fig. 2-6). There is also excellent agreement between the T-matrix and the FMM after increasing the aspect ratio from 2:1 to 10:1 for the rigid prolate spheroid in the case of broadside and end-on backscatter (Fig. 2-7). All of the cases in Figs. 2-6 and 2-7 illustrate the interference between the specular reflection and a Franz or creeping wave and the associated shifts in the peaks and nulls for the different angles of incidence and reception (Uberall *et al.*, 1966).

Boundary element method (BEM)

Francis (1993) developed a numerical method of computing the scattering by a finite body using a boundary element method based on a partial application of a Helmholtz gradient formulation. The FMM and BEM agree perfectly to high frequencies ($ka = 10$) in the case of end-on backscatter for a 2:1 aspect ratio rigid prolate spheroid (Fig. 2-8).

Exact prolate spheroidal solution

The exact solution for a prolate spheroid in prolate spheroidal coordinates has been used by various investigators (Yeh, 1967; Furusawa, 1988; and Ye *et al.*, 1997). While this is formally an exact solution, it encounters the same numerical challenges mentioned in

72

Figure 2-6: FMM and T-matrix: Backscattered and bistatic form function of a 2:1 rigid prolate spheroid as a function of ka for the case of broadside backscatter, backscatter at oblique incidence and bistatic scattering. T-matrix results are from Figs. 3, 4 and 5 of Varadan *et al.* (1982). The form function is given in Eq. (2.47).
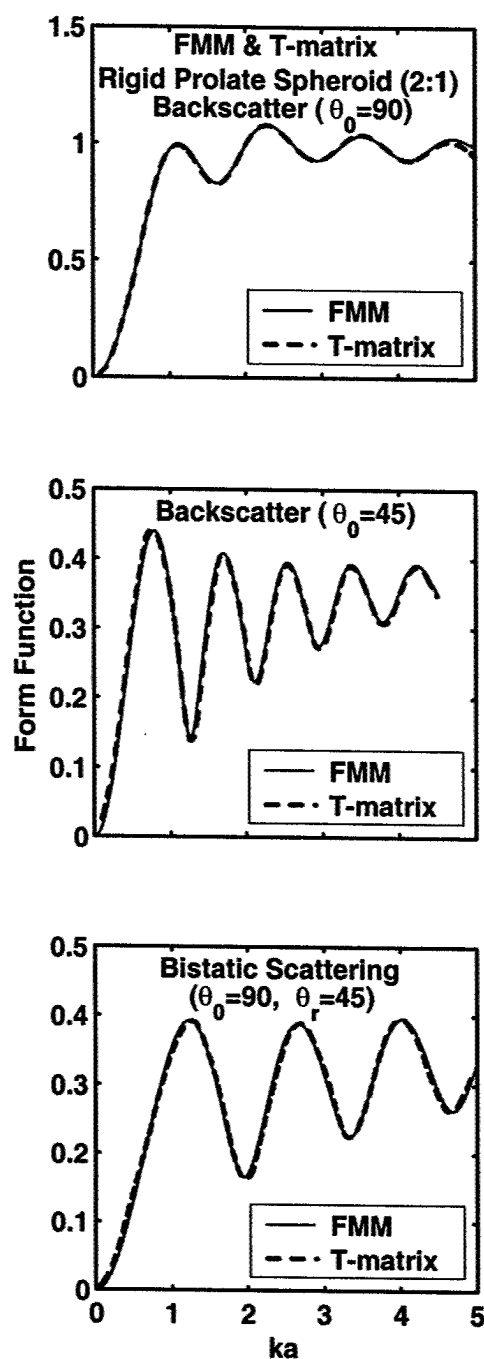
73
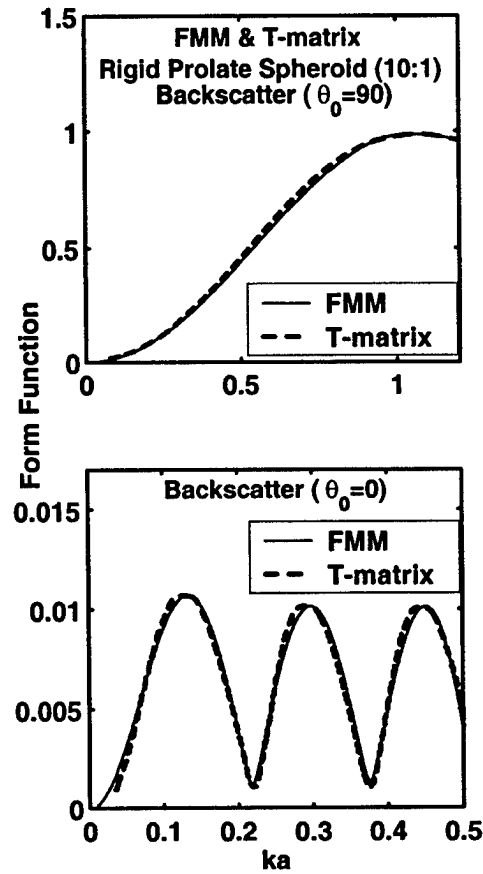
Figure 2-7: FMM and T-matrix: Backscattered form function for a 10:1 rigid prolate spheroid as a function of ka for the case of broadside incidence and end-on incidence. T-matrix results are from Fig. 37(a) of Hackman (1993). The form function is given in Eq. (2.47).
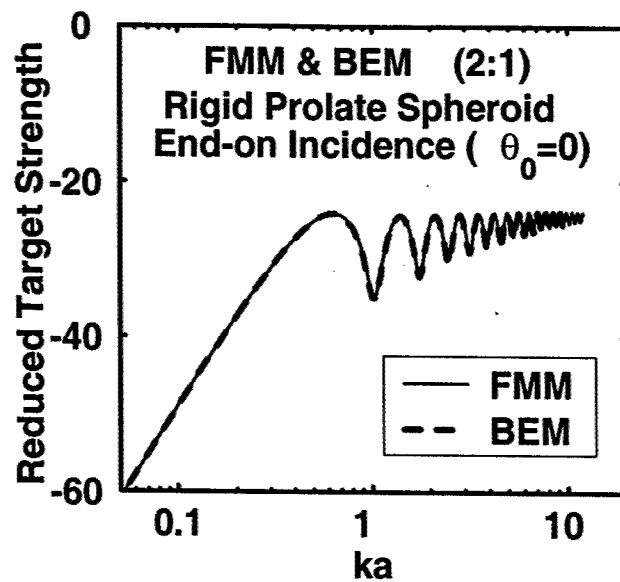
Figure 2-8: FMM and BEM: Reduced Target Strength as a function of ka for a 2:1 rigid prolate spheroid at end-on incidence. The agreement continues well past $ka=10$. BEM results are from Francis (2001).

Sec. III. Comparisons of the FMM to the exact solution in the case of backscatter and forward scatter for a range of incidence angles ($\theta_0 = 30°, 70°, 90°$) demonstrate good to excellent agreement in all cases (Fig. 2-9).

Kirchhoff approximation

The Kirchhoff approximation is a frequently used approximation for backscattering; however, it is generally limited to the geometric scattering region ($ka \gg 1$), perfectly reflecting boundary conditions (soft and rigid) and near-broadside incidence (Born and Wolf, 1999). It is a convenient approximation for the amplitude of the backscatter, but does not accurately represent the oscillations in the amplitude due to the interac-

Figure 2-9: FMM and Exact Prolate Spheroidal Solution: Reduced Target Strength as a function of ka for a 10:1 rigid prolate spheroid at incidence angles of 30, 70 and 90 degrees for backscatter and forward scatter. Exact prolate spheroidal solutions are from Fig. 7 of Ye *et al.* (1997).
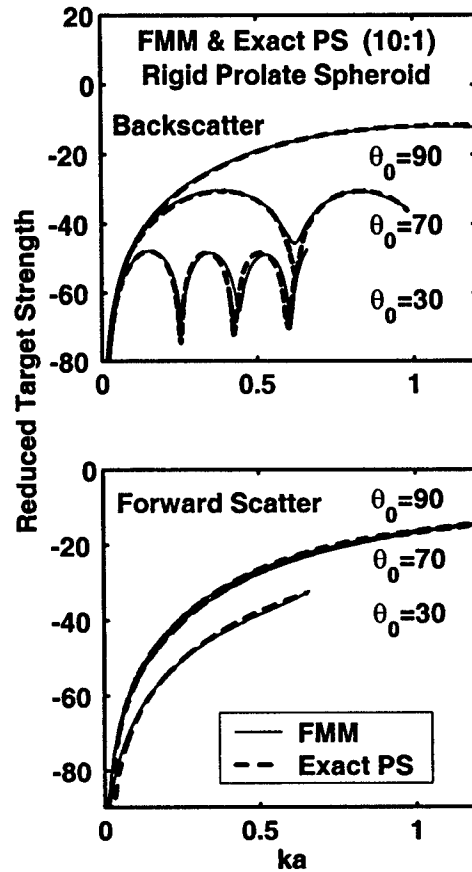
tion between the specular reflections and Franz waves. Comparisons of the FMM to this approximation within the range of reliability of the Kirchhoff approximation further establish the consistency of the FMM. Specifically, the reduced target strengths for broadside backscattering generally agree well for the single frequencies presented, with improved agreement as the frequency increases (Fig. 2-10). At $ka = 1$, the Kirchhoff approximation is near the limit of its range of validity and under-estimates the amplitude. Additionally, it can be seen that the Kirchhoff approximation falls off much more rapidly than the FMM for all ka as the incidence angle moves away from broadside.

2.4.3 Irregular bodies: comparison with Kirchhoff approximation

As emphasized earlier, accurate computation of the scattering by smooth elongated bodies is not a simple task, particularly as the aspect ratio and frequencies increase. The additional complexity of an irregular surface further complicates an already difficult problem. A key distinction of the FMM is its ability to conformally map an irregular axisymmetric surface to an orthogonal coordinate system that better fits the scatterer surface. To demonstrate the practical application of the FMM to a realistic, asymmetrical, irregular body with non-Gaussian roughness, the acoustic scattering by a gas-filled swimbladder from an alewife fish (*Alosa pseudoharengus*) has been modeled and compared with the Kirchhoff approximation for two representative shapes (Figs. 2-11 and 2-12). This particular problem was chosen as fish are a significant scatterer of sound in the ocean and

77
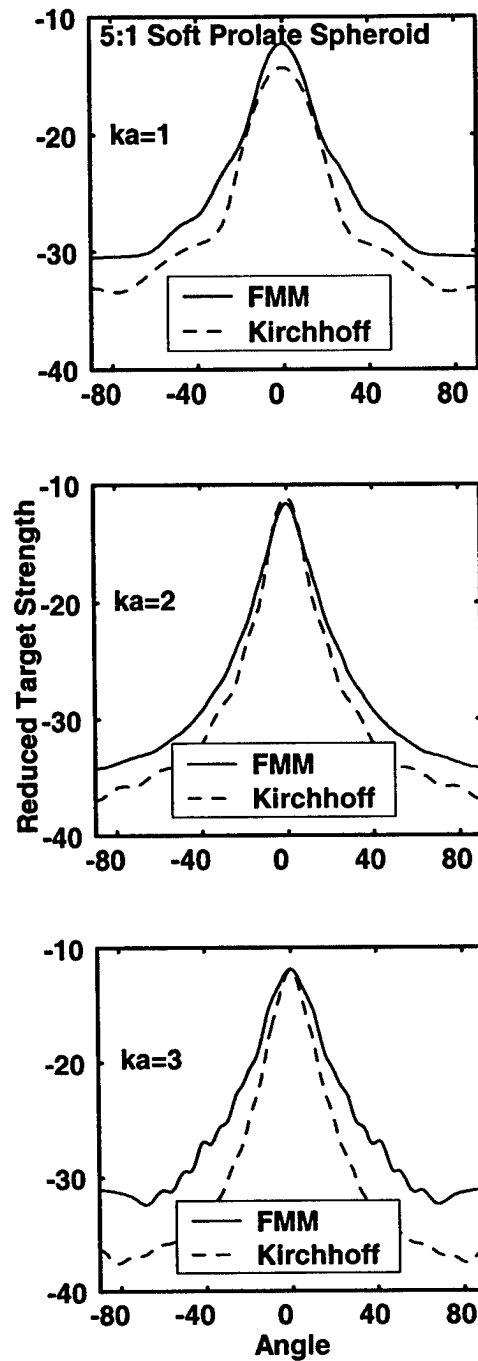
Figure 2-10: FMM and Kirchhoff Approximation: Reduced Target Strength as a function of angle for a 5:1 soft prolate spheroid at ka =1, ka =2 and ka =3. Kirchhoff approximation results are based on the formulation from Born and Wolf (1999). The largest differences occur well off broadside, where the Kirchhoff approximation characteristically underpredicts the scattering.

78

Figure 2-11: FMM and Kirchhoff Approximation: Target Strength as a function of angle for irregular Shape #1 at $ka =1$, $ka =2$, $ka =3$ and $ka =4$. Kirchhoff approximation results are based on the formulation from Clay and Horne (1994). Shape #1 is shown in the bottom frame. The vertical axis is exaggerated to better illustrate the irregularity of the surface. Broadside corresponds to 0 degrees.

79

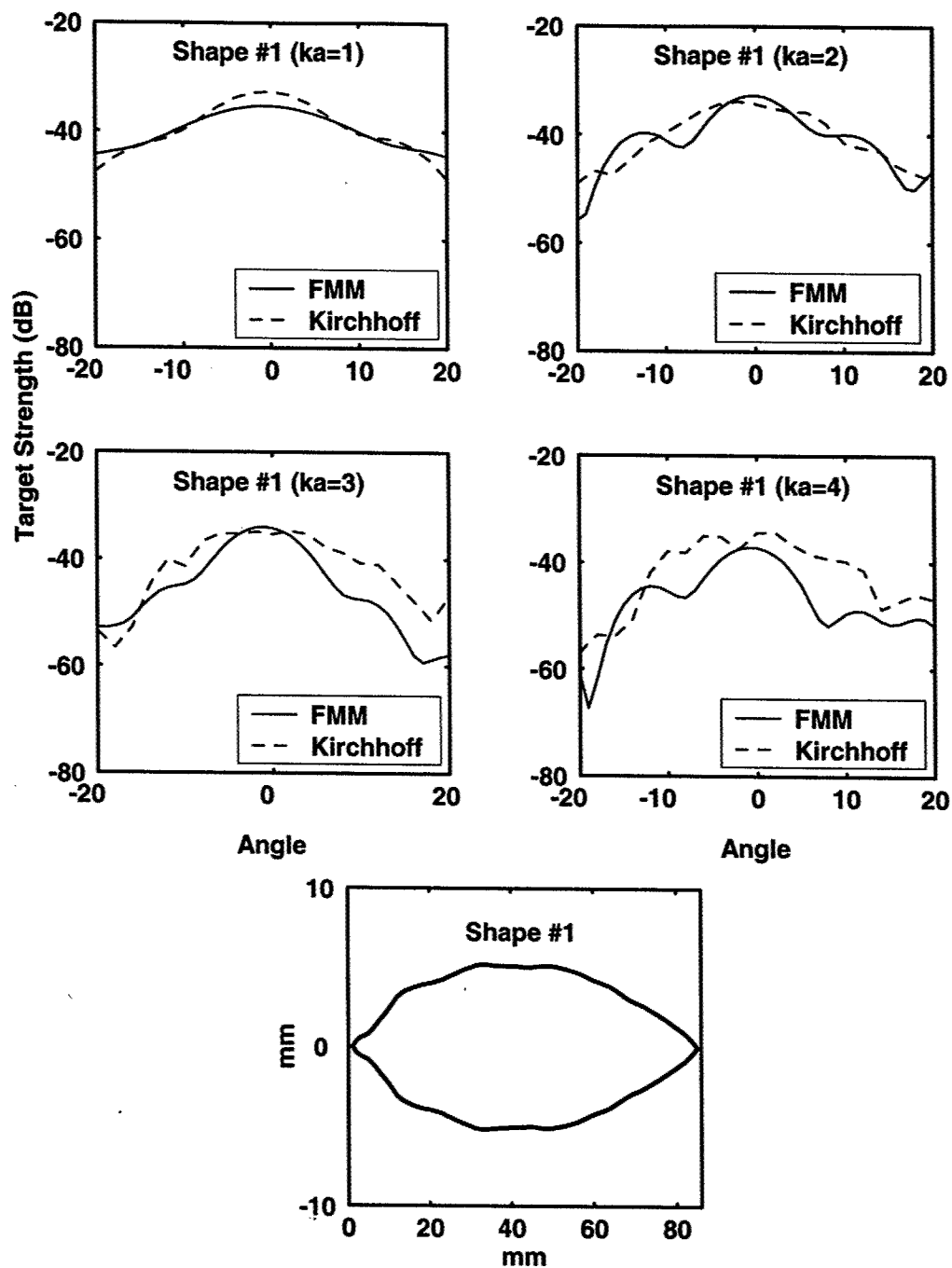Figure 2-12: FMM and Kirchhoff Approximation: Target Strength as a function of angle for irregular Shape #2 at ka =1, ka =2, ka =3, ka =4 and ka =5. Kirchhoff approximation results are based on formulation from Clay and Horne (1994). Shape #2 is shown in the bottom right frame. The vertical axis is exaggerated to better illustrate the irregularity of the surface. Broadside corresponds to 0 degrees.
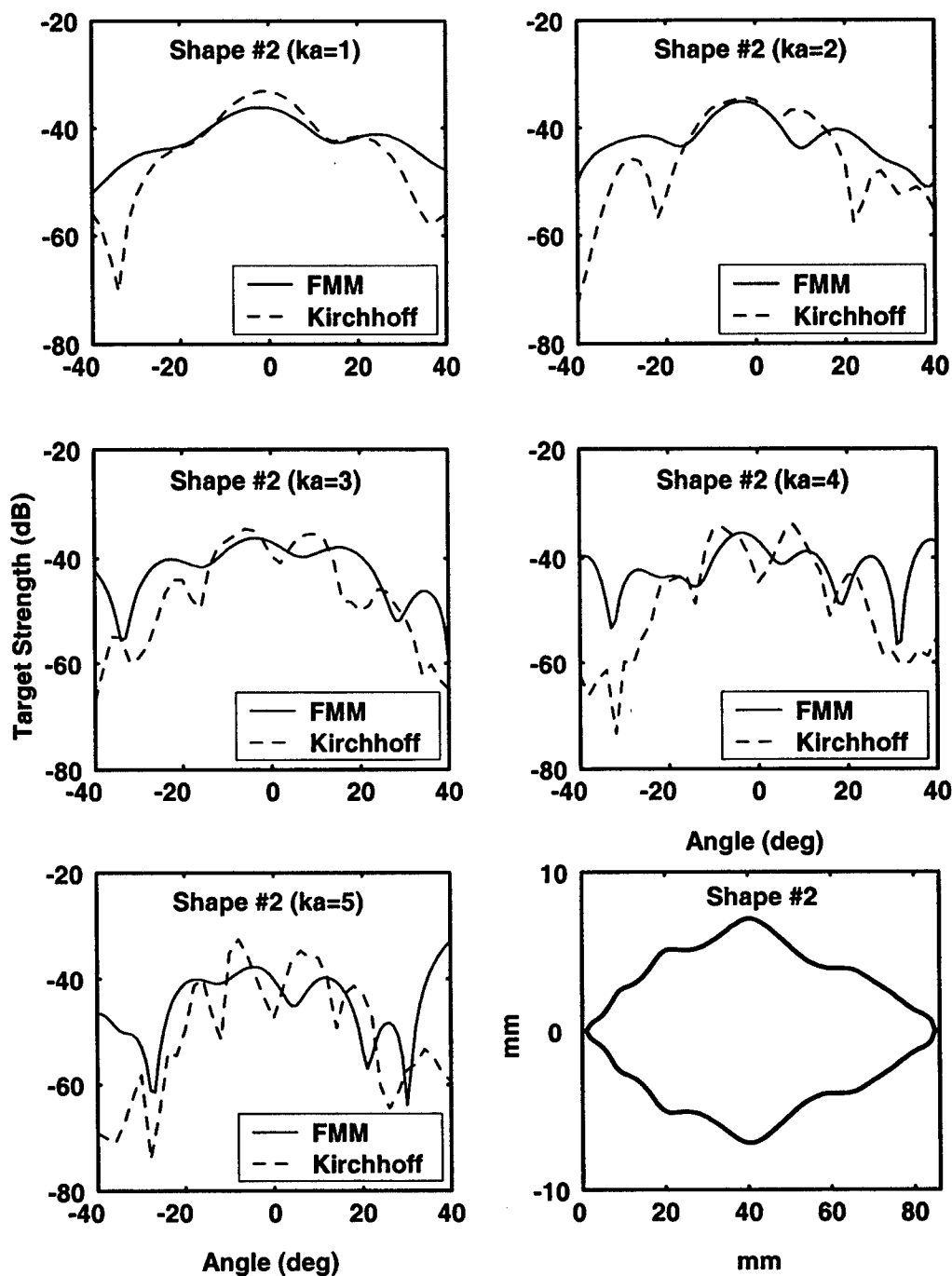
the swimbladder is the organ in the fish that generally dominates the scattering. A more extensive treatment of this application is given in Reeder *et al.* (submitted). At these values of ka the soft boundary condition was used given the high contrast in material properties between the gas and surrounding tissue. There is reasonable agreement between FMM and Kirchhoff for most values of ka for Shape #1 in Fig. 2-11, but for Shape #2 in Fig. 2-12, the Kirchhoff predictions generally under-estimate relative to the FMM at angles well off broadside.

2.4.4 Low ka resonance scattering for gaseous bodies: comparison with T-matrix and exact prolate spheroidal solutions

In contrast to the cases of rigid and weakly-scattering objects described above whose scattering levels decrease dramatically in the $ka \ll 1$ region, gaseous bodies have a strong resonance in that region and have been the subject of many earlier studies. Although in the low ka region there are fewer restrictions in the calculations, challenges still remain in the prediction of scattering from gaseous bodies with high aspect ratios. In this study, the FMM is directly compared with the T-matrix method and the exact prolate spheroidal solution over a range of aspect ratios up to 20:1 for constant volume prolate spheroids. Predictions from the T-matrix method and FMM are compared in Fig. 2-13 for aspect ratios up to 16:1; however, results for aspect ratios up to 20:1 were presented by Feuillade and Werby (1994) using the T-matrix method, as well as Ye and Hoskinson (1998) using the exact prolate spheroidal solution. In addition, low ka res-
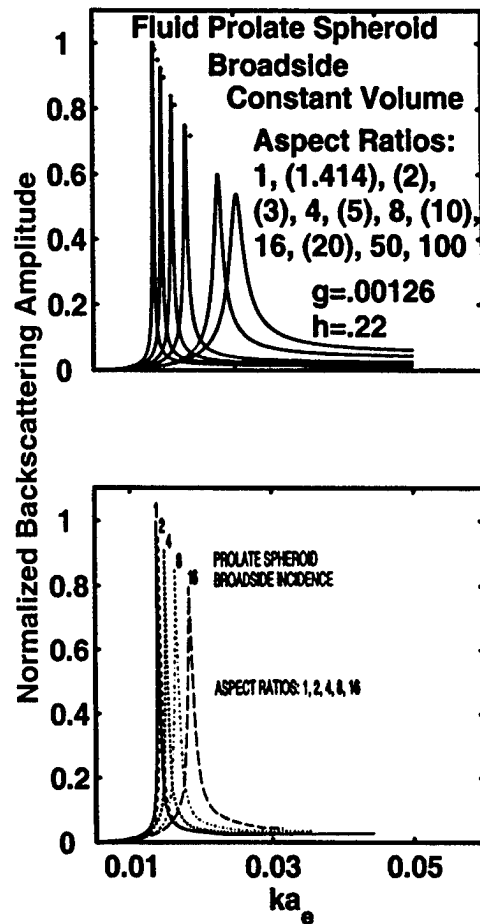
Figure 2-13: FMM and T-matrix: Normalized backcattering amplitude as a function of ka_e for a gaseous (g=0.00126, h=0.22) prolate spheroid at broadside incidence. Results from the FMM (top panel) are compared to results from the T-matrix method (bottom panel) from Fig. 4(a) of Feuillade and Werbe (1994). The single dots in the top panel are peak amplitudes for aspect ratios listed in parentheses. The backscattering amplitude on the vertical axis is normalized to the peak amplitude of the sphere. As the aspect ratio of the spheroid is increased beyond 1:1, the dimensions of the spheroid are changed to maintain a volume equal to that of the original sphere. Thus, the a_e in ka_e is the equivalent spherical radius of the object, corresponding to the radius of the sphere (the 1:1 case shown) that has the same volume as the prolate spheroid. Results for aspect ratios up to 20:1 were tabulated by Feuillade and Werby (1994) using the T-matrix method, as well as Ye and Hoskinson (1998) using the exact prolate spheroidal solution. There is excellent agreement among predictions from all three formulations for aspect ratios up to 20:1.

82

onance scattering by gaseous bodies of higher aspect ratio (up to 100:1) was calculated with no difficulties relative to the numerical issues cited earlier. These ratios are much higher than what has previously appeared in the literature (Strasberg, 1953; Weston, 1967; Feuillade and Werby, 1994; Ye and Hoskinson, 1998). The FMM accurately predicts the scattering in the resonance region—the increase in the resonance frequency, the decrease in the resonance amplitude and the broadening of the resonance peaks for prolate spheroids of constant volume and increasing aspect ratio within the verifiable range of aspect ratios presented in the literature (up to 20:1 aspect ratios).

2.5 Summary and conclusions

An extension of a two-dimensional conformal mapping approach to scattering by irregular, finite-length bodies of revolution has been presented for three boundary conditions. The model conformally maps the coordinate variables of the original coordinate system to a new orthogonal coordinate system in which the locus of all points where the new radial coordinate is a constant exactly coincides with the scatterer surface. The solutions to the transformed Helmholtz equation are a general solution for the total pressure in the case of far-field scattering from a finite body of revolution. This model has been shown to be very accurate in the prediction of scattering from smooth, symmetric bodies for a wide range of frequencies (Rayleigh through geometric scattering region), scattering angles (monostatic and bistatic), aspect ratios and boundary conditions, and for all angles. Good agreement has also been demonstrated for irregular, realistic shapes

when compared to the Kirchhoff approximation. This work represents a significant advancement by providing a numerically efficient formulation that is applicable over a wide range of frequencies, scattering angles and geometries for soft, rigid and fluid boundary conditions.

There is great potential for further development of this model, including application to acoustic scattering by elastic solids and shells. The implementation of better numerical integration techniques, the use of extended precision format of floating point arithmetic or various smoothing techniques (Yamashita, 1990) could delay the onset of ill-conditioned matrices, accelerating convergence. New scaling techniques based upon the physical scattering mechanisms could also increase accuracy (Schmidt, 1993).

Chapter 3

Broadband acoustic backscatter and high-resolution morphology of fish: Measurement and modeling[1]

3.1 Introduction

Acoustic surveys of marine organisms have long been used to rapidly and synoptically survey the ocean for organisms of ecological and economic importance. Acoustic methods complement traditional methods such as direct sampling with nets. Direct sampling furnishes biological data such as abundance, biomass, direct measurements of organism size and species identification, but encounters problems such as net avoidance, small

---

[1]This chapter is based on an article submitted to the Journal of the Acoustical Society of America (Reeder *et al.*, submitted).

sampling volumes, catch destruction of delicate specimens, and costs in time and money. Acoustically surveying the ocean for marine organisms could avoid these problems, particularly with respect to large-scale synoptic surveys while obtaining high-resolution data (Gunderson, 1993; Medwin and Clay, 1998). Since acoustic sampling does not directly produce biological data, inference of biological information from acoustic scattering by marine organisms requires an understanding of the process by which those organisms scatter sound.

Understanding the scattering mechanisms of marine organisms is a challenge due to the fact that fish anatomy is complex and the acoustic scattering characteristics are correspondingly complex. Nash *et al.* (1987) illustrated the influence of the various anatomical components of fish on the scattering by performing length-wise acoustic scans of whole fish and dissected swimbladders, heads and vertebrae (Fig. 3-1).

Given the complexities of the scattering characteristics of marine organisms as illustrated in that and other studies, detailed investigations must be made into the scattering mechanisms of the animals in order to determine and decipher the extent to which each dependency contributes to the overall scattering characteristics. Studies must consist of careful, accurate measurement of the acoustic scattering and associated modeling to effectively elucidate these mechanisms. Due to the large number of organisms that exist in the ocean, it is not possible to study the scattering by all species; however, organisms can generally be categorized according to morphological groups. For example, fish can be categorized by morphological characteristics, such as size, shape and the presence or
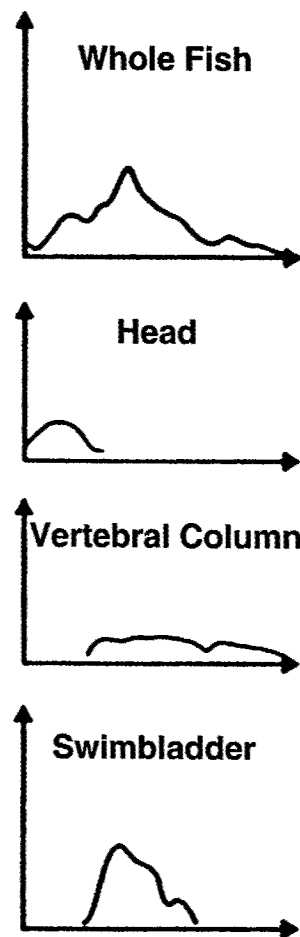
Figure 3-1: Curves of relative acoustic pressure vs. length for a largemouth bass showing relative scattering contributions by the whole fish, head, vertebral column and swimbladder. This qualitative illustration of the dependence of fish target strength on changes in morphology was generated through the use of a focused array transducer system that scanned the length of the object at 220 kHz in the near-field. Adapted from Nash *et al.* (1987).

absence of swimbladders (Foote, 2001). Regarding zooplankton, Stanton *et al.* (1994a, 1998a, 1998b) identified three major categories: fluid-like (e.g., euphausiids, shrimp, copepods), gas inclusions (e.g., siphonophores), and elastic shells (e.g., pteropods).

Much research has been directed toward making measurements of the scattering of sound by fish, usually in terms of target strength (Midttun, 1984; Foote, 2001). Studies have included measurement of target strengths *in situ* and *ex situ*, with both multiple and single targets. *In situ* measurements present the challenge of unknown target size, orientation and sometimes position relative to the acoustic beam, while *ex situ* measurements provide greater control over these factors, although in an unnatural environment (Foote, 1997). *Ex situ* measurements of tethered fish include those conducted by Jones and Pearce (1958), Diercks and Goldsberry (1970), Haslett (1969), Love (1969, 1970, 1971), Nakken and Olson (1977), Miyanohana *et al.* (1990), and Benoit-Bird and Au (2001). Although most of these measurements were performed at single frequencies and at a limited number of angles of orientation (mostly dorsal), they were performed on a variety of species of different sizes and demonstrate complicated variability that is dependent upon morphology, orientation and acoustic wavelength. Attempts have been made to empirically quantify the relationship between echo amplitude and actual fish length (Love, 1977; Foote, 1987). Although linear regression curves have been used with some success, they are constrained to certain ranges of frequencies and species, and lack the ability to make predictions outside those bounds (Horne and Jech, 1999). More sophisticated scattering models have been required to better account for the complexities

introduced by shape, orientation and material properties.

Modeling of the scattering of sound by complex body shapes is a difficult problem due to the mathematical challenge of exact solutions and the computational difficulties of numerical approaches. A number of approaches have been used to represent the shape of the dominant scattering mechanisms. For low frequency applications, the acoustically dominant swimbladder has been modeled as a sphere (Andreyeva, 1964; Love, 1978; Ye and Farmer, 1994; Feuillade and Nero, 1998) and as a prolate spheroid (Weston, 1967). At high frequencies, the elongation of the scatterers has increasing importance and efforts in this frequency region have been made to describe the scattering by more realistic, irregular shapes. For example, Jones and Pearce (1957) and Haslett (1962b) attempted to experimentally approximate the shape of a fish swimbladder as a cylinder and ellipsoid, respectively, and Do and Surti (1990) used a series of cylinders and cones in a similar fashion. Furusawa (1988) and Ye (1996) modeled acoustic scattering by fish using prolate spheroids. Arrays of point scatterers (Clay and Heist, 1984) have been used to model the fish body form. Foote (1985) computed the target strength of fish by applying the Kirchhoff approximation to a realistic 3-dimensional model of the swimbladder based on the digitized microtomed swimbladder of pollack (*Pollachius pollachius*) and saithe (*Pollachius virens*). Clay (1991) combined a component of Stanton's (1988a, 1989a) deformed finite cylinder model (based on a modal series solution) in the $ka < 0.15$ region with the Kirchhoff approximation for $ka > 0.15$ to create the Kirchhoff-ray mode (KRM) model to account for the irregular shape of the swimbladder

and fish body and make predictions over all of ka. Clay and Horne (1994) modeled acoustic backscatter of Atlantic cod (*Gadus morhua*) using the KRM model. Foote and Francis (2002) modeled the target strength of swimbladdered fish using the boundary element method based on the same swimbladder shapes in Foote (1985). Models using the exact shape of the animals' morphology are desired because they are more realistic and promise greater accuracy over models based on simple geometric shapes, especially in the geometric scattering region (high ka). Each of the above-mentioned scattering models are limited with respect to frequency range, class of surfaces, types of boundary conditions, eccentricity of shape and/or numerical efficiency.

As shown in the above studies, successful use of acoustics in ocean observations requires accurate scattering models for each category of animal, verification and refinement of the models through accurate, extensive measurements of scattering from fish, and reliable algorithms for numerical implementation of the models. Very importantly, advanced scattering models must include scatterer shapes that closely resemble the dominant scattering features within the fish. This information requires high-resolution morphological measurements of the fish to be made. Another important requirement is that the acoustic scattering measurements be conducted over a wide range of frequencies, preferably with continuous coverage over the frequency band.

In spite of the need for broad spectral coverage in the scattering measurements, the majority of acoustic measurements on fish are in terms of target strengths at single frequencies. Although this level of information has been proven to be very useful for certain

applications, such as fishery population estimates, traditional target strength measurements lack spectral coverage for rigorous model development. Specifically, narrowband measurements are performed at discrete frequencies, thus frequency dependencies are missing from the data, although this has been addressed in part by use of multiple discrete frequencies. Since an animal's scattering properties vary considerably with the frequency of the transmitted signal, the use of broadband transducers offer continuous coverage over a significant range of frequencies, thus increasing the amount of information contained in the signal. Furthermore, the broadband signals inherently have high temporal resolution (which varies with inverse bandwidth of the transmitted signal) which can be realized through the use of an impulse signal or pulse compression of a longer signal (Chu and Stanton, 1998). With high temporal resolution, scattering features can possibly be resolved in time and identified. In spite of the great advantages of broadband signals, relatively few studies have investigated and/or exploited the animal's spectral characteristics (Kjaergaard *et al.*, 1990; Simmonds *et al.*, 1996; Zakharia *et al.*, 1996).

The needs for broadband acoustic measurements and advanced scattering models that incorporate high-resolution morphology are addressed in this study. Extensive broadband acoustic measurements were conducted on live, adult alewife (*Alosa pseudoharengus*), which were tethered while being rotated in 1-degree increments of orientation angle over all angles in two planes of rotation (lateral and dorsal/ventral). Spectral and time-domain analyses identify dominant scattering mechanisms and demonstrate the extent to which the scattering depends on size, shape, acoustic frequency and orientation angle.

91

Traditional x-rays and advanced techniques involving CT scans were used to rapidly and non-invasively image the anatomy of the fish so that digitizations of swimbladder shape could be incorporated into two scattering models–the KRM model referenced above (using traditional x-rays), as well as a newly developed scattering formulation, the Fourier Matching Method (FMM) for axisymmetric finite-length bodies (Reeder and Stanton, submitted) The FMM formulation is a versatile model applicable over a wide range of shapes, all angles and all frequencies. Predictions by the two scattering models, using the morphological information, are compared to the acoustical backscattering laboratory measurements of the alewife.

This chapter is organized as follows. In Sec. II, basic descriptions of target strength and pulse compression (PC) processing of broadband signals are delineated, followed by a synopsis of the Kirchhoff-Ray Mode and Fourier Matching Method models. In Sec. III, the laboratory setup, methods used for data collection and measurements of animal morphology are presented. Acoustic scattering results are presented in Sec. IV. Comparisons between model predictions and measurements are made in Sec. V, followed by a summary and conclusions in Sec. VI.

3.2 Theory

3.2.1 Definitions

The far-field scattered sound wave is expressed as:

$$P^{scat} \underset{r \to \infty}{\to} P^{inc} \frac{e^{ikr}}{r} f, \tag{3.1}$$

where P^{inc} is the pressure amplitude of the acoustic wave incident upon the object, r is the distance between the object and receiver, k ($= 2\pi/\lambda$, where λ = wavelength) is the acoustic wavenumber of the incident field and f is the scattering amplitude. The far-field scattering characteristics of the object are fully described by the scattering amplitude. Given the sometimes large dynamic range of the backscattering amplitude, it is often expressed in logarithmic terms as target strength (TS), expressed in units of decibels (dB) relative to 1 m (Urick, 1983):

$$TS = 10 \log_{10} |f_{bs}|^2 = 10 \log_{10} \sigma_{bs}, \tag{3.2}$$

where $\sigma_{bs} \equiv |f_{bs}|^2$ is the differential backscattering cross section and differs from the often-used backscattering cross section , σ, by a factor of 4π ($\sigma = 4\pi\sigma_{bs}$). The term, f_{bs}, is the scattering amplitude evaluated in the backscatter direction. Target strength is often normalized by the square of some typical dimension to give the reduced target

93

strength (RTS):

$$RTS = 10 \log_{10} \left| \frac{\sigma_{bs}}{L^2} \right| = 10 \log_{10} |f_{bs}|^2 - 10 \log_{10} \left| L^2 \right|, \qquad (3.3)$$

where L is, in the case of elongated scatterers, the length of the scattering object. In the case of a sphere, the target strength is often normalized by πa^2 instead of L^2. The average target strength is expressed in terms of the value of the average backscattering cross section:

$$\langle TS \rangle = 10 \log_{10} \langle \sigma_{bs} \rangle, \qquad (3.4)$$

where the average, denoted $\langle \rangle$, is performed over the frequency band and before the logarithm operation is performed.

3.2.2 Pulse compression

In order to resolve major scattering features such as the head and swimbladder of the fish, the received signal is compressed in time by cross correlating the echo with the received calibration signal. The result is a short, high-amplitude signal with increased signal-to noise ratio (SNR). This type of process is enhanced for long, wideband signals such as those used in this study. This approach is similar to the commonly used matched filter that involves cross correlating the received signal plus noise with the signal without the noise (Turin, 1960). In the case of scattering from marine organisms, however, the exact scattering characteristics of the animal are not known; therefore, the "replicate"

94

signal (corresponding to the signal without the noise) used in the correlation process for a true matched filter, is not known. Chu and Stanton (1998) suggested using a different signal in the cross-correlation: the received calibration signal obtained during calibration. This modified matched filter process is referred to as pulse compression and its output is referred to as the compressed pulse output (CPO). The resultant output is a series of echoes, corresponding to the dominant scattering features of the target.

3.2.3 Models

Two scattering models that are valid for elongated scatterers and for a wide range of frequencies and orientations are used to compare with the experimental data: the Kirchhoff-Ray Mode (KRM) model which has previously been applied to fish acoustics and the newly developed Fourier Matching Method (FMM).

KRM

The Kirchhoff-Ray Mode (KRM) model has been used to compute the scattering from fish with a hybrid approach by predicting the scattering in the low ka region with a monopole ($m = 0$) mode to a cylinder solution and predicting the high ka region with the Kirchhoff, or "ray", approximation. For both components of the solution, the scattering object is approximated by 1-mm long cylindrical volume elements, $v(j)$, constructed from digitized shape of the body and swimbladder using traditional x-ray images. For the swimbladder scattering in the low ka region ($ka < 0.15$), the cylindrical monopole solution is written

as the sum of the scatter from N_e elements:

$$f_{bs}^{(sb)} = \frac{-i}{\pi} \sum_j^{N_e} b_0 e^{-i2kv(j)} dx(j), \qquad (ka < 0.15) \qquad (3.5)$$

where $f_{bs}^{(sb)}$ is the scattering amplitude as a function of frequency (notation of L (script) in Clay and Horne (1994) is replaced by $f_{bs}^{(sb)}$), b_0 is the zero-order mode scattering coefficient, and dx is the incremental element along the length of the swimbladder. For the swimbladder scattering in the high ka region ($ka > 0.15$), the Kirchhoff ray approximation is used. The above equation is modified to sum the backscatter from N_e swimbladder elements:

$$f_{bs}^{(sb)} = -i\frac{R_{fs}(1 - R_{wf}^2)}{2\sqrt{\pi}} \sum_{j=0}^{N_e-1} A_{sb}(k_{fb}a(j)+1)^{1/2} e^{-i(2k_{fb}v_U(j)+\Psi_{sb})} \triangle u(j), \qquad (ka > 0.15)$$

$$(3.6)$$

where R_{fs} is the reflection coefficient, U and L indicate the upper and lower surfaces, wf refers to the water-fish interface, fs denotes the swimbladder-fish body interface, fb denotes the fish body, sb refers to the swimbladder, $\triangle u(j)$ is the incremental distance between elements, and A_{sb} and Ψ are empirical amplitude and phase adjustments for small ka. A similar expression using the Kirchhoff approximation describes the scattering

for the fish body in the high ka region ($ka > 0.15$):

$$f_{bs}^{(fb)} = -i\frac{R_{wf}}{2\sqrt{\pi}} \sum_{j=0}^{N_e-1} \{(ka(j))^{1/2} \qquad\qquad (ka > 0.15)$$

$$\times [e^{-i(2kv_U(j))} - (1 - R_{wf}^2)e^{i(-2kv_U(j)+2k_{fb}(v_U(j)-v_L(j))+\Psi_{fb})}] \qquad (3.7)$$

$$\times \triangle u(j)\},$$

The total scattering from the fish body and swimbladder is the coherent sum of the scattering amplitudes:

$$f_{bs}^{(tot)} = f_{bs}^{(sb)} + f_{bs}^{(fb)}, \qquad\qquad (3.8)$$

where the choice of expressions using either Eq. (3.5) or (3.6) for $f_{bs}^{(sb)}$ is implicit and depends on the particular value of ka.

FMM

The Fourier matching method (FMM) used herein to describe the scattering by the swimbladder involves the use of a two-dimensional conformal mapping approach to describe scattering by axisymmetric, irregular, finite-length bodies of revolution (Reeder and Stanton, submitted). The model conformally maps the coordinate variables of the original coordinate system to a new orthogonal coordinate system in which the new radial coordinate being a constant exactly coincides with the scatterer surface. The solutions to the transformed Helmholtz equation are a general solution for the total pressure in the

case of far-field scattering by a finite body of revolution. This model has been shown to be very accurate in the prediction of scattering by smooth, symmetric bodies for a wide range of frequencies (resonance in the Rayleigh region through the geometric scattering region), scattering angles (monostatic and bistatic), aspect ratios and boundary conditions. Good agreement has also been demonstrated for irregular, realistic shapes when compared to the Kirchhoff approximation (Reeder and Stanton, submitted).

Using a conformal mapping function of the form:

$$G(\rho) = c_{-1}e^{\rho} + \sum_{n=0}^{\infty} c_n e^{-n\rho}, \tag{3.9}$$

where c_n are the conformal mapping coefficients determined by solving a system of nonlinear constraints using the Newton-Raphson method, the coordinate system is mapped to a new, orthogonal coordinate system in which the constant radial coordinate exactly coincides with the scatterer surface (in this case, the swimbladder outer boundary). The scattering amplitude in the new coordinate system is:

$$f = \sum_{n=-\infty}^{\infty} \sum_{m=-\infty}^{\infty} b_{nm} i^{-n-1} P_n^m \left(\frac{g(u,w)}{r(u,w)} \right) e^{imv}, \tag{3.10}$$

where b_{nm} are the far-field scattering coefficients that depend on the shape and material properties of the scatterer, P_n^m are associated Legendre functions, $r(u,w)$ is the new radial coordinate, and $g(u,w)$ is a function of the new system. The far-field scattering coefficients, b_{nm}, are determined after solving the transformed Helmholtz equation and

satisfying the boundary conditions at the surface of the scatterer. Details and definitions of the parameters are in Reeder and Stanton (submitted). The FMM results presented here are based upon the scattering by the swimbladder alone—they do not include the computation of scattering from the fish body. As a consequence, the FMM will expectedly underpredict the scattering.

3.3 Experimental methods

Seventeen adult alewife fish were used in the acoustic backscattering measurements. The morphology of the fish was characterized through a combination of dissection and three x-ray technologies. The scattering measurements were performed on individual fish secured in a tether in a laboratory tank.

3.3.1 Animals

Alewife were chosen because they are readily caught and are similar to the important fish, Atlantic herring (*Clupea harengus*), in their body size, shape and swimbladder construction (Fig. 3-2). Both alewife and Atlantic herring expand and contract their swimbladders primarily by transferring air via a pneumatic duct between their esophagus and swimbladder. Other methods of maintaining buoyancy include diffusion and secretion of gases via a network of blood vessels and gas glands in contact with the swimbladder.
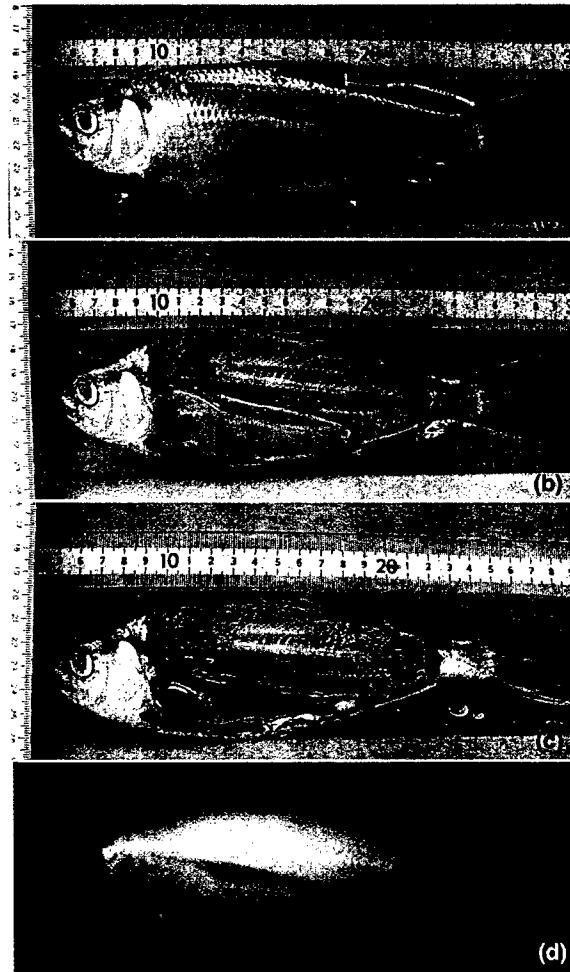
Figure 3-2: Images of alewife used in the acoustic scattering experiments: (a) whole fish, (b) dissected fish showing enlarged gonads, (c) dissected fish with gonads removed to expose the swimbladder, and (d) traditional x-ray of whole fish showing (dark) outline of swimbladder. The fish were collected as they swam upstream to spawn in the freshwater ponds of Cape Cod, Massachusetts; consequently, their gonads were enlarged as seen in (d). All of the fish were adults with an average caudal length of 22 *cm* and an average body weight of 144 grams.

Table 3-1. Dimensions, weights and availability of acoustic, x-ray and dissection data for each of the alewife used in the acoustic scattering measurements. Total length (TL) is the distance from the nose to the tip of the tail. Caudal (standard) length (CL) is the distance from the nose to the end of the flesh near the tail.

Animal Desig	Animal Tag #	Gender	TL (mm)	CL (mm)	Height (mm)	Width (mm)	Weight (g)	Acoustic:X-ray:Dissection
10	152	F	259	215	59.7	25.2	159	Yes:No:Yes
11	153	M	255	217	52.4	21.3	120	Yes:No:Yes
12	154	M	255	225	54.3	23.8	133	Yes:Yes:Yes
13	155	F	268	225	60.8	27.3	172	Yes:Yes:Yes
14	156	M	258	220	59.0	26.0	151	Yes:Yes:Yes
15	157	F	256	216	54.7	23.0	135	Yes:Yes:Yes
16	158	M	260	220	62.8	25.8	168	Yes:Yes:Yes
17	159	F	244	215	59.4	22.8	120	Yes:Yes:Yes
18	160	M	241	200	59.7	23.7	121	Yes:Yes:Yes
19	161	M	257	217	56.7	24.5	141	Yes:Yes:Yes
20	162	F	259	216	63.5	26.1	165	Yes:Yes:Yes
21	163	M	254	217	59.6	24.0	147	Yes:Yes:Yes
22	164	*	254	223	56.6	24.7	148	Yes:Yes:No
23	165	F	277	235	56.4	23.3	150	Yes:Yes:Yes
24	166	F	255	217	57.0	23.8	139	Yes:Yes:Yes
25	167	*	250	213	50.9	22.2	116	Yes:Yes:No
26	168	*	265	225	56.5	26.0	157	Yes:Yes:No

The fish were collected in May, 2000 as they were migrating upstream to spawn in the freshwater ponds of Cape Cod, MA. The standard (caudal) lengths (measured between the nose and end of the flesh near the tail) of these fish were quite uniform, averaging 22 cm. Their body weights averaged 144 grams. Since these fish were ready to spawn, their gonads were enlarged. The males' gonads were approximately 10% of their body weight, while the females' gonads equaled as much as 15% of their body weight. The animals' physical dimensions and weights are summarized in Table 1.

3.3.2 Morphometry of animal shapes: PCX and CT scans

In addition to visual inspection of the fish (both whole and in dissected form), the morphology was investigated through quantitative use of various x-ray technologies–the traditional x-ray, phase contrast x-rays (PCX) and computerized tomography (CT) scans. After the acoustic measurements were recorded, traditional x-rays (Fig. 3-2d) of the fish were performed at the Falmouth Animal Hospital in N. Falmouth, Massachusetts. These x-ray images were later used to generate hand-traced digitized objects of the swimbladder and fish body for use in the KRM model. Traditional x-rays are gray-scale images produced on a film that is sensitive to the amplitude of energy absorbed by an object. However, x-rays change not only in amplitude, but also in phase as the material distorts the wave as it passes through the material is ignored. Traditional x-ray imagery ignores this distortion, yet the newly developed PCX process captures these extremely small phase changes, resulting in a high-resolution image with contains much finer detail than

tradition x-ray images (Wilkins, 1996; Davis and Stevenson, 1996; Gureyev *et al.*, 2000). PCX imaging, performed on an alewife at the Commonwealth Scientific and Industrial Research Organisation (CSIRO) in Melbourne, Australia, is sensitive to, and illustrates well, the small-scale anatomical features of alewife such as fins, ribs, striations in muscle tissue, gills and weakly scattering soft tissue (Fig. 3-3). Such high-resolution imagery dramatically aids the determination of the scattering features in fish.

Additionally, high-resolution computerized tomography (CT) scans were performed on an alewife at the Falmouth Hospital in Falmouth, Massachusetts (Fig. 3-4). The images produced by the scans were used to generate a three-dimensional digital object of the swimbladder to be incorporated into the FMM scattering model. The alewife was scanned along the longitudinal axis of the animal, producing 112 images 2 mm apart. "Slices" of the fish were created to examine the morphology of the animal in each cross section. The original CT images contained 500 x 900 pixels, but were then cropped (referenced to a common pixel to maintain accurate physical proportions) for ease of numerical manipulation. The CT images were then converted to a three-dimensional binary matrix, each element of which contained a "1" for each element of the original matrix whose value was above a certain threshold. Thus, a three-dimensional digital object of the fish was produced (Fig. 3-5a). A wire-cage diagram was then created of the fish body to better illustrate the exact physical morphology of the fish and its swimbladder (Fig. 3-5b). Coordinate points were then extracted from the top, bottom and side boundaries of the digital object of the swimbladder. Each of these boundaries
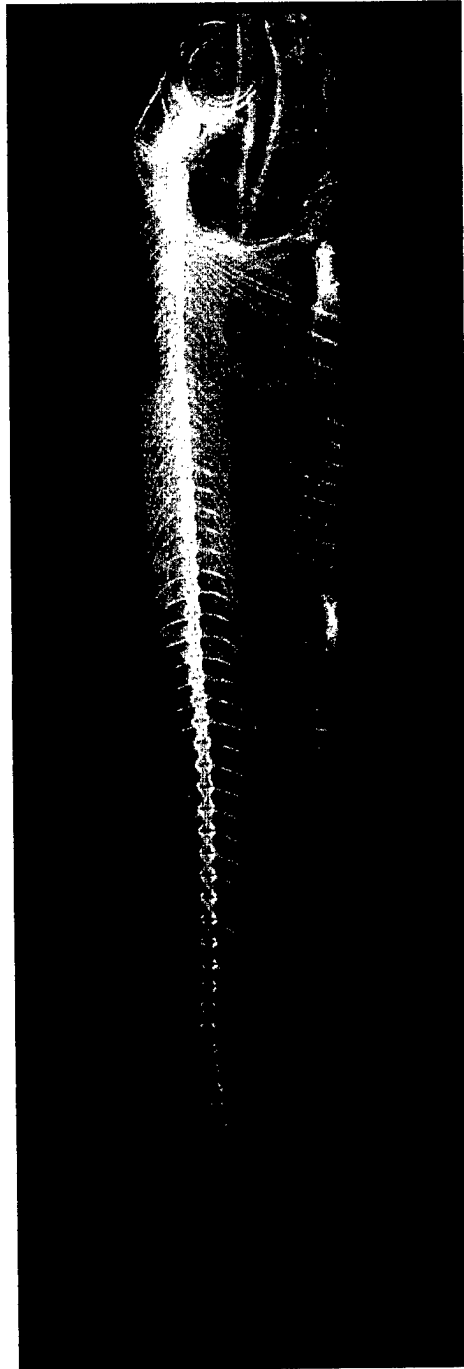
Figure 3-3: Phase Contrast X-ray (PCX) of an alewife. Imaging was performed at the Commonwealth Scientific and Industrial Research Organisation (CSIRO) in Melbourne, Australia. The PCX process is an extremely high-resolution imaging technique which is sensitive to weakly scattering body tissue. Slight morphological details can be detected, such as the gills, fins, ribs, striations in the muscle tissue, gonads and gut (Stevenson, 2002).
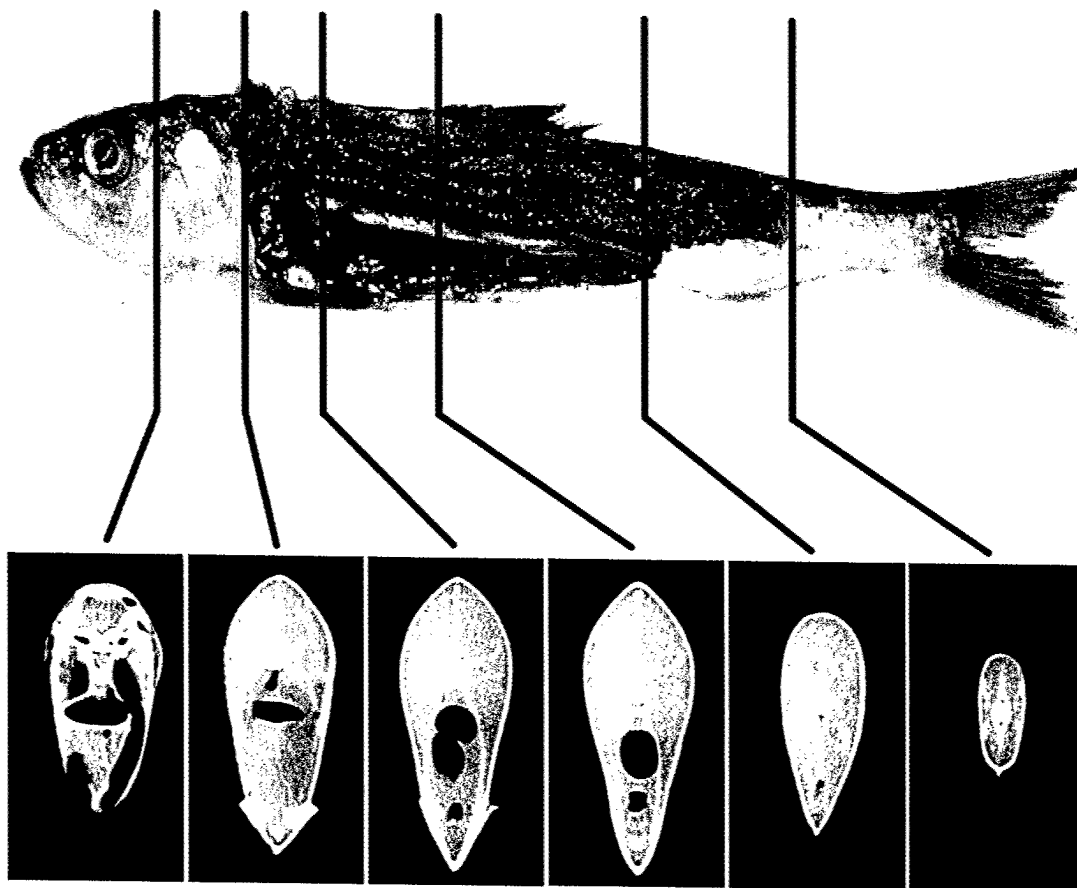
Figure 3-4: High-resolution Computerized Tomography (CT) scan images of an alewife with their placement indicated along the fish body. The black areas within the cross-sectional slices include the swimbladder and gas-inclusions in the gut, which is connected to the esophagus near the head. The vertebral column and muscle tissue can also be seen in the images.
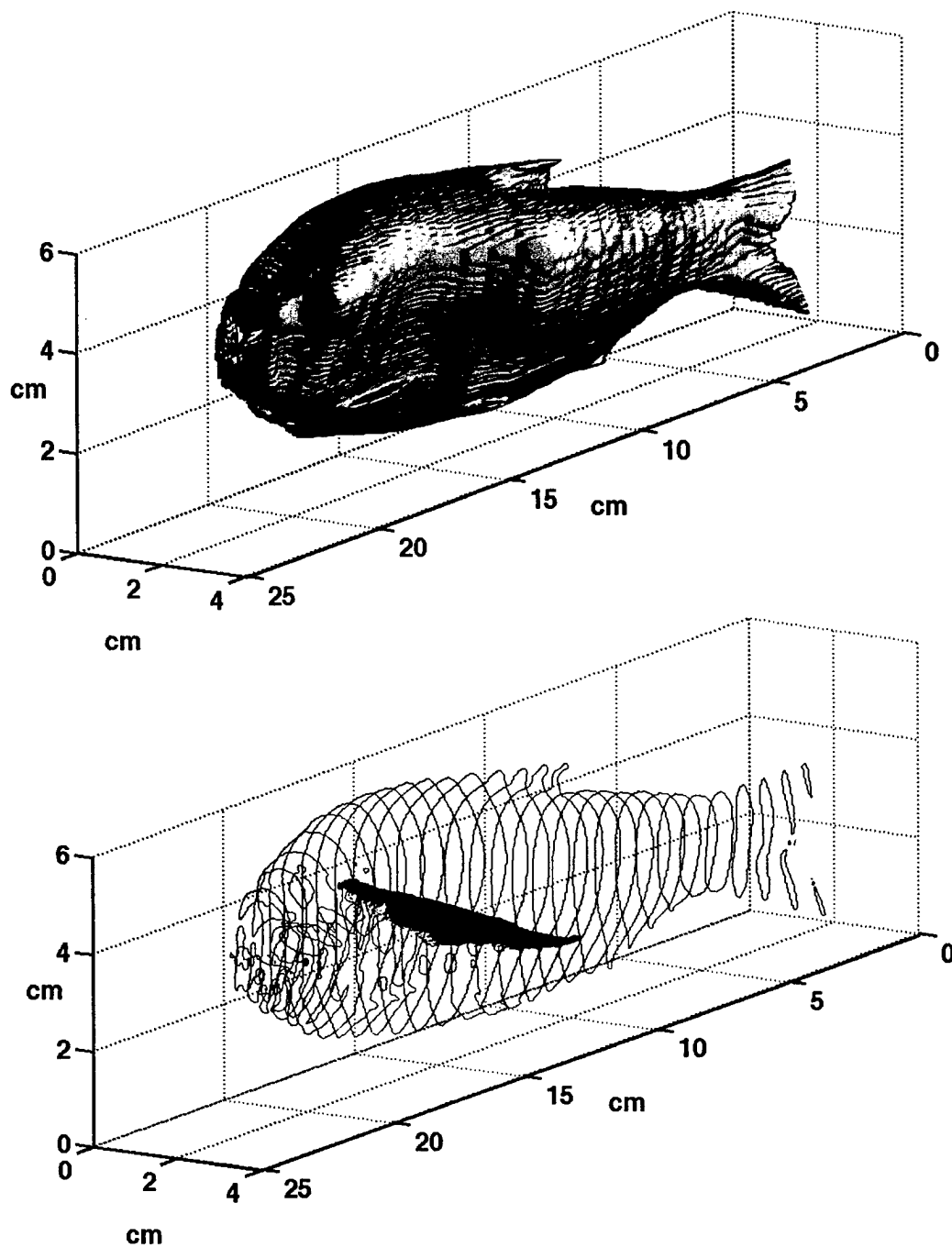
Figure 3-5: Three-dimensional digital objects generated from CT scan imagery: whole fish (upper panel) and wirecage diagram of fish body with swimbladder object inside (lower panel). The 112 images generated during the CT scan were processed by a digital image processing algorithm to generate the exact shapes to incorporate into the FMM for scattering predictions.

were rotated about the axis to form three bodies of revolution to model each of the scattering planes–dorsal, ventral and lateral. These points were used by the FMM to conformally map the swimbladder objects into a new coordinate system in which the new radial coordinate exactly matches the surface of the body. The CT scans are an efficient and non-invasive method of producing high-resolution images of fish. This method is in contrast to the direct, but time-consuming, method of microtoming (Foote, 1985; Ona, 1990).

3.3.3 Acoustic data acquisition

The acoustic backscattering measurements were conducted in a large freshwater tank at Benthos, Inc. in North Falmouth, MA (Fig. 3-6). The experimental setup, similar in concept to that described in Stanton *et al.* (2000), included the use of a power amplifier, signal generator, a pair of transducers, pre-amplifier, band-pass filter, oscilloscope and personal computer. During the measurements, the individual fish were secured in a harness in the center of the acoustic beam and rotated. Although all animals were alive and in good condition at the beginning of each measurement, some died part-way into the measurement. The data presented here are from nine data sets on three animals (15, 17 and 26), all of which remained alive for the entire measurement.

A pair of Reson TC2116 broadband acoustic transducers was mounted horizontally in the tank facing the fish in the tethering system, the center of which was attached to a computer-controlled stepper motor which rotated the assembly in 1^0 increments through

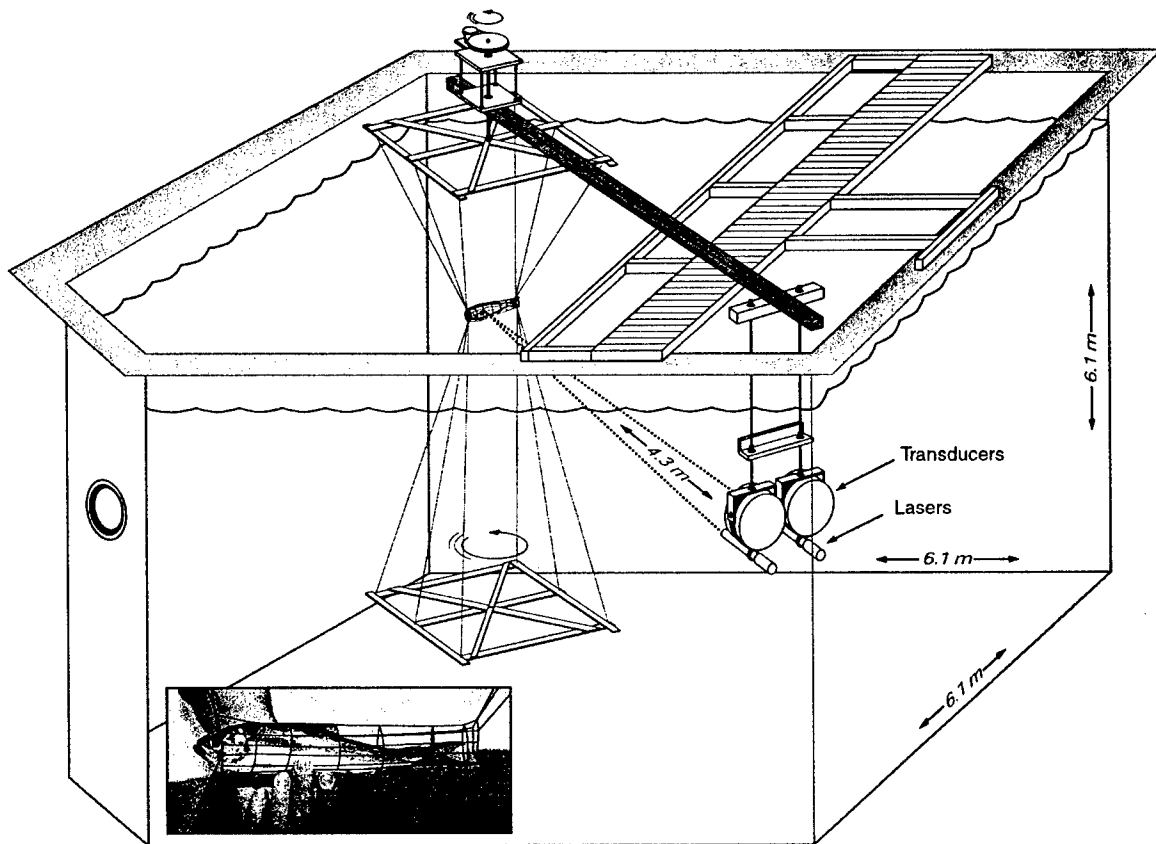Figure 3-6: Schematic of the laboratory system used for measuring acoustic backscattering by live, individual fish as a function of angle of orientation and frequency: tank, transducers, lasers used for alignment, stepper motor to rotate the animal in the acoustic beam and acoustically transparent tether system. The photograph of the harness, shown in the inset, was enhanced so the thin monofilament can be seen.

two full rotations (720 pings per data set). The two transducers were identical and closely spaced, one used as the transmitter and one as the receiver, approximating a monostatic configuration. The use of two transducers allows closer scattering ranges, minimizes the effect of transmitter ringing and makes the system easier to calibrate. The fish were insonified with a shaped chirp signal with a usable frequency spectrum ranging from 40kHz to 95kHz (Fig. 3-7).

The transmitted signal was shaped to make the composite response of the transducer pair approximately uniform over the usable bandwidth. The transmitted voltage time series, $v_{bs}^T(t)$, and the received voltage time series (the backscattered return echo from the animal), $v_{bs}^R(t)$, were stored on a personal computer for later analysis.

The tethering system consisted of a specially designed, hand-made harness (Fig. 3-6 inset) made of 4 lb. test fishing line suspended in the tank by six lines to a frame mounted just above the surface of the water and by six lines to a frame near the bottom of the tank. The harness was designed to hold the fish in the center of the acoustic beam and at a constant range ($r_{bs} = 4.3$ m) from the transducers as the fish was rotated. The harness uses the least amount of material possible in order to be acoustically transparent. It provided just enough restriction to prevent escape while allowing the fish to move as freely as possible to minimize stress. The harness has six longitudinal lines, one on the top, one on the bottom and two along each side. The vertical members of the harness are spaced more closely together near the head of the fish to prevent escape, and spaced farther apart toward the rear of the fish to allow for freedom of movement. The vertical

109
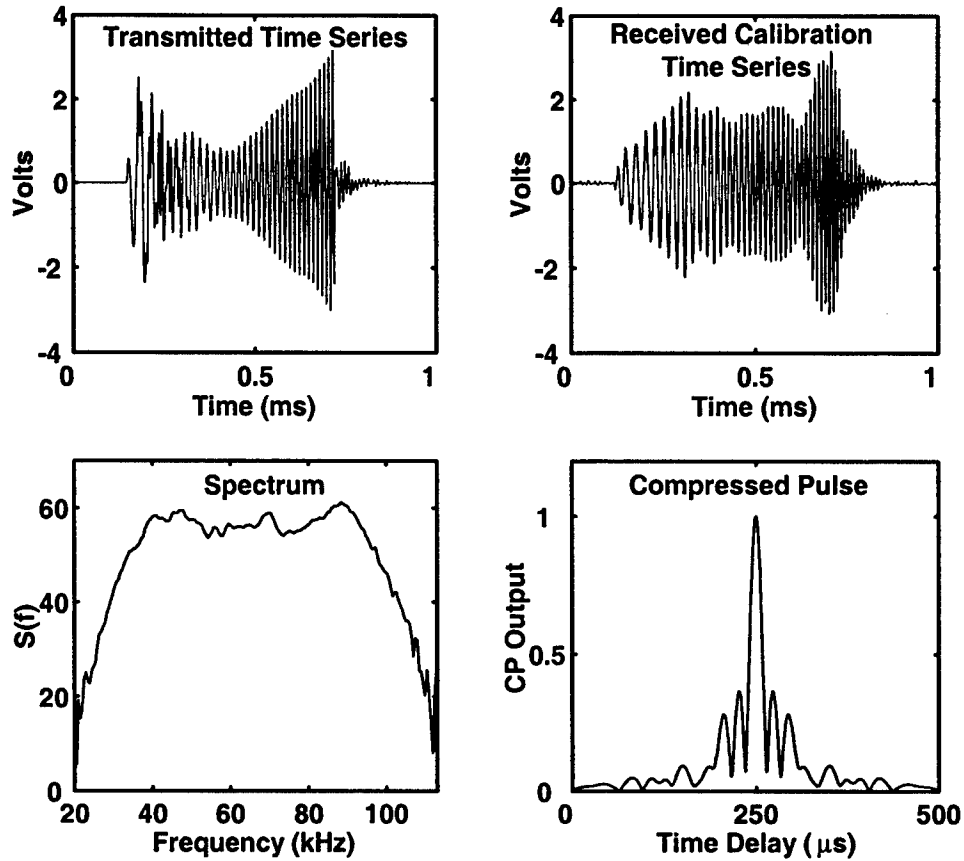
Figure 3-7: Broadband chirp signals: time series of voltage signal as applied to the transmitting transducer and used during both the scattering experiment and calibration; time series of calibration signal as measured at the output of receiving transducer; frequency spectrum of received calibration signal; and auto-correlation function (compressed pulse) of the received calibration signal which corresponds to matched filter output. The transmitted signal was shaped to flatten the composite response of the transducer pair across the frequency band of 40-95kHz. The received calibration signal was stored for later use in the analysis to generate absolute target strengths on a ping-by-ping basis. The normalized compressed pulse output has sidelobes which are numerical processing artifacts with maximum peaks of 0.365. These sidelobes can introduce spurious artificial echoes in the analysis which must be taken into account.

members near the gills are spaced so as not to restrict the gills. The harness has a cinch at the front that is tightened before the fish is slipped into the harness from the back. Once the experiment is complete, the cinch is loosened and the fish can be removed by slipping it through the front of the harness, avoiding damage to the fins and scales of the fish. The lines to each of the points on the top and bottom frames can be used to adjust the precise position of the harness in the tank. The bottom frame is suspended just above the bottom of the tank by the six bottom lines so that it is outside of the acoustic beam but does not drag on the bottom of the tank.

Before each fish was placed in the tether, much attention was given to ensuring that the harness was located in the center of the acoustic beam and was free of bubbles. Underwater lasers were mounted and aligned on the bottom of the transducers to aid in the alignment of the transducers (Fig. 3-6). Due to the relatively large distances involved, these lasers proved to be indispensable in the process of alignment. The tether system was adjusted so that when the fish was placed in the harness for measurement, the system would pivot about the approximate center of its swimbladder. To eliminate bubbles coalescing on the harness, all of the lines on the tethering system were thoroughly wetted and rubbed with a soap solution prior to measurement. This process was done each time the tethering system was taken out of the water for any reason. Additionally, a small amount of soap was applied to each transducer face before calibration and measurement to ensure good contact with the seawater and to minimize adherence of bubbles that could contaminate the acoustic signals.

The background reverberation of the tank was taken into account for the scattering measurements. The background reverberation signals (with no fish in the tank) were summed over hundreds of pings and the resultant (unwanted) coherent echo was then stored in the digital oscilloscope. While collecting backscattering signals from the fish, the stored background reverberation signal was subtracted from the echo in real time by the oscilloscope. The difference signal that was stored, $v_{bs}^R(t)$, during the experiment consisted of the echo from the fish and random noise of the entire system.

The system was carefully calibrated prior to each set of backscattering measurements following the pseudo-self-reciprocity calibration procedure referred to by Urick (1983) and outlined in detail by Stanton *et al.* (1998a). The system was calibrated by mounting the transducers such that they faced each other and were separated by a range of $r_{cal} = 4.1$ m. The time series of the shaped, chirp transmitted calibration ($v_{cal}^T(t)$) voltage and the average of hundreds of received ($v_{cal}^R(t)$) calibration voltages were stored on a computer and used later in order to calculate fish target strengths. The received calibration signal was also used in the pulse compression analysis discussed in Section II.

Taking into account the calibration information, the scattering amplitude of the fish was computed for each ping:

$$f_{bs} = \frac{V_{bs}^R}{V_{cal}^R} \frac{V_{cal}^T}{V_{bs}^T} \frac{r_{bs}^2}{r_{cal}}, \tag{3.11}$$

where V_{bs}^R, V_{bs}^T, V_{cal}^R and V_{cal}^T are the absolute values of the Fourier transforms of the band-pass filtered voltage time series v_{bs}^R, v_{bs}^T, v_{cal}^R and v_{cal}^T (Fig. 3-7).

3.4 Experimental results

The broadband signals have been analyzed in both the frequency and time domains. The orientation dependence of the scattering has been examined for each Fourier component of the signal, and the spectral and temporal patterns have been examined for every orientation angle. Given the great difference in shape of the swimbladder in the dorsal/ventral and lateral planes, the results from these different planes are analyzed.

3.4.1 Spectral domain

Acoustic backscattering strength was observed to be strongly dependent upon acoustic frequency and animal orientation (Figs. 3-8, 3-9, 3-10 and 3-11). These relationships are demonstrated in both planes of scattering–dorsal/ventral and lateral. Generally, the target strength is maximum near broadside incidence. Also, at fixed angles of orientation, the target strength varies with frequency, represented by a series of peaks and nulls (Fig. 3-11).

The beamwidth of the main scattering lobes from the fish generally become more narrow with increasing frequency (Figs. 3-8, 3-8 and 3-10). Ventral aspect scattering is generally less directional than corresponding dorsal aspects (Figs. 3-9 and 3-10).

3.4.2 Time domain

The compressed pulse output (CPO) shows separation of the echo into multiple highlights, apparently due to different dominant scattering features in the fish (Figs. 3-12, 3-13
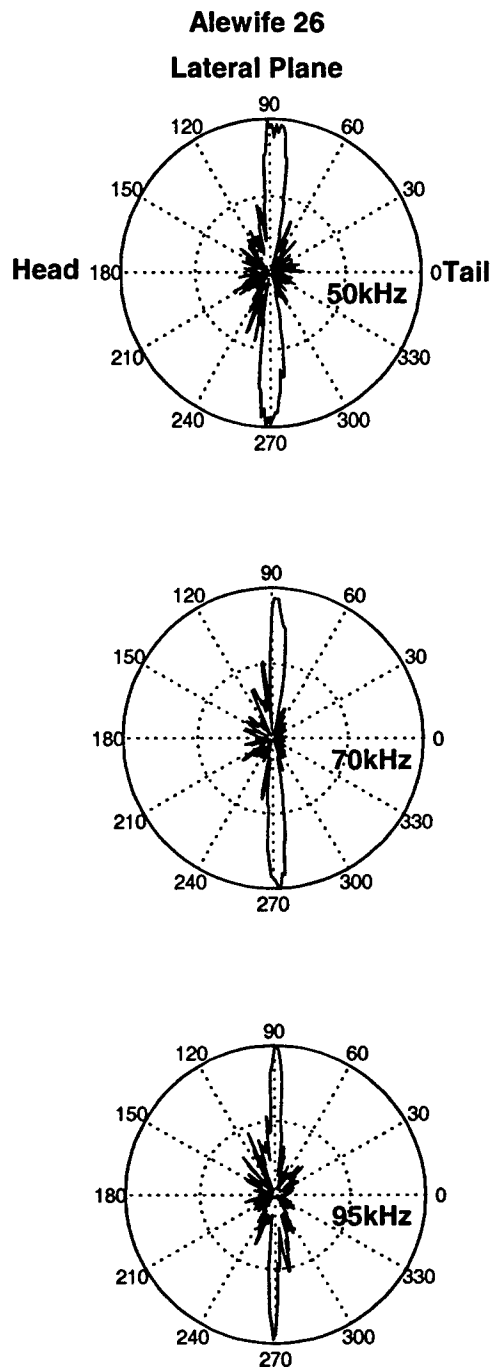
Figure 3-8: Magnitude of backscattering amplitude as a function of angle as measured for Alewife 26 in the lateral plane at 50 kHz, 70 kHz and 95 kHz. Tail-on orientation corresponds to 0 degrees. Each plot is on a linear scale, normalized to unity and based on a one-ping recording for each one-degree increment of rotation.
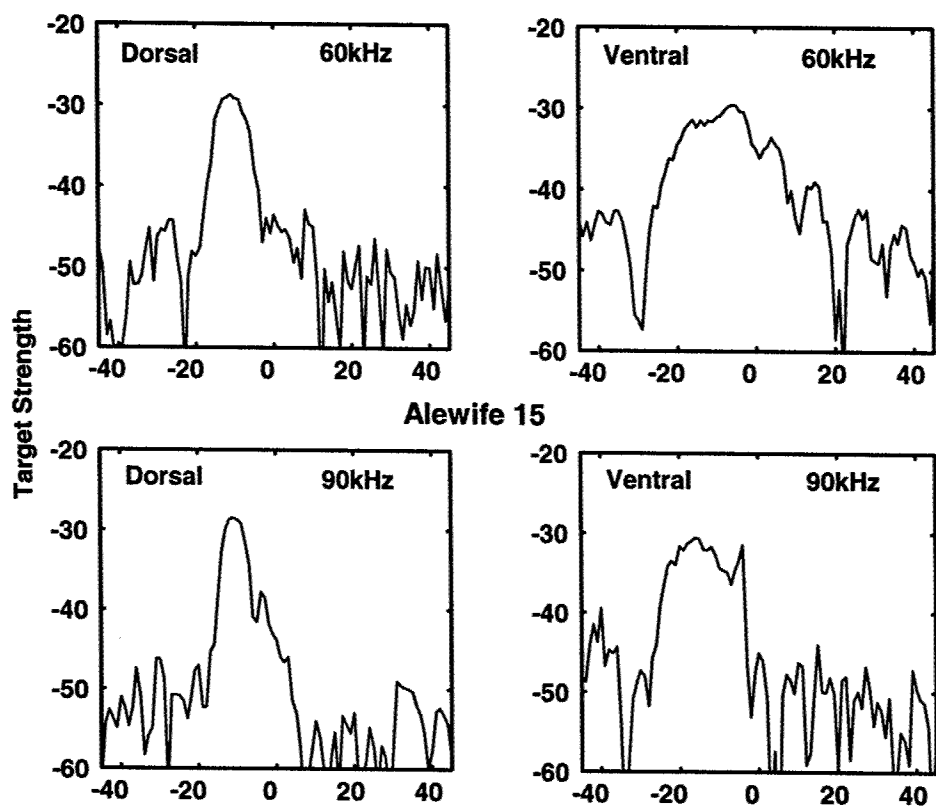
Figure 3-9: Target strength as a function of angle of orientation as measured for Alewife 15 in the dorsal/ventral plane at 60 kHz and 90 kHz. Zero degrees corresponds to normal incidence relative to the dorsal or ventral sides for the left and right panels, respectively. For a free-swimming, horizontally oriented fish, 0 degrees dorsal and 0 degrees ventral angles would correspond to a downward- and upward-looking acoustic transducer.
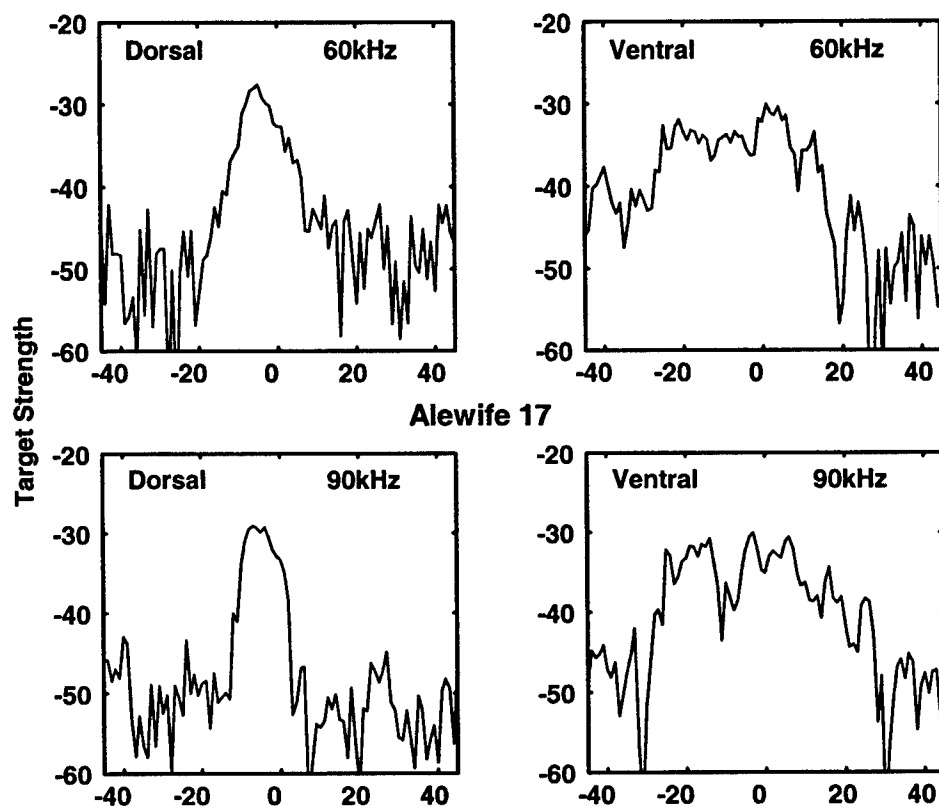
Figure 3-10: Target strength as a function of angle of orientation as measured for Alewife 17 in the dorsal/ventral plane at 60 kHz and 90 kHz. The plotting convention is the same as in Fig. 3-9.
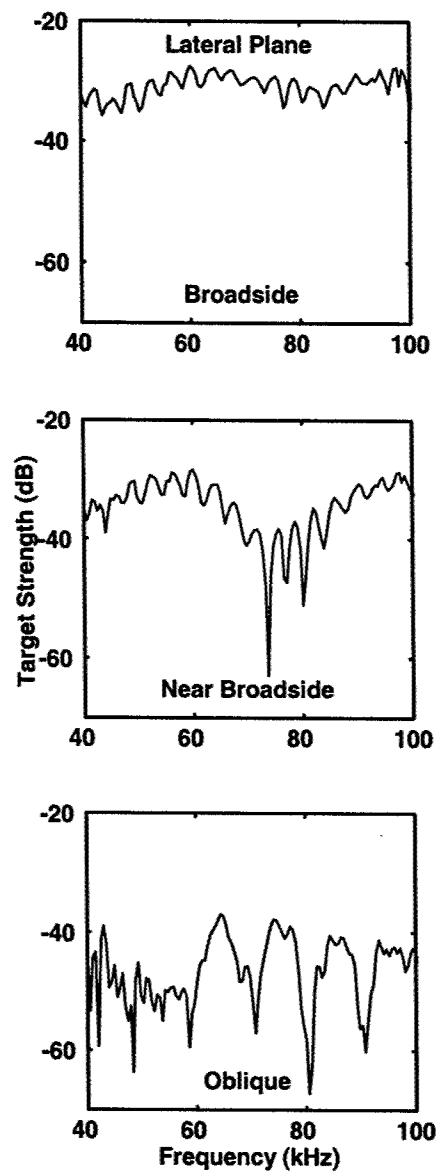
Figure 3-11: Target strength as a function of frequency in the lateral plane as measured for Alewife 15 at broadside, near broadside and oblique angles of incidence. In this case, the oblique angle was 30 degrees from end-on, or 60 degrees from broadside.

117
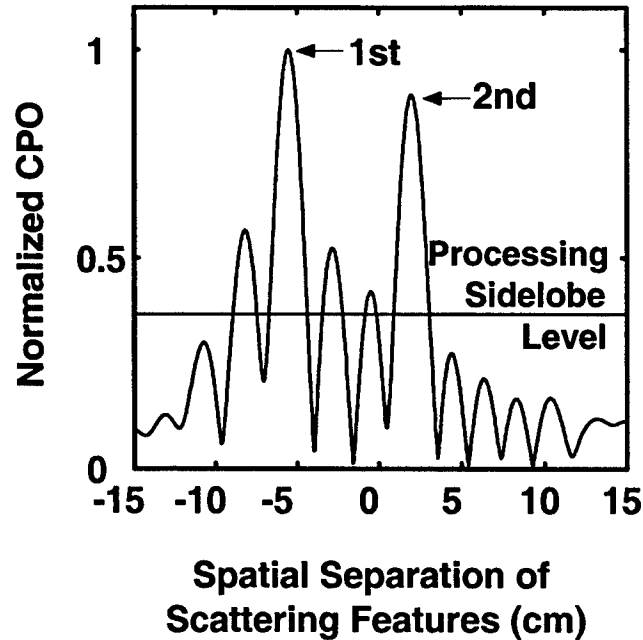
Figure 3-12: Normalized compressed pulse output (CPO) for Alewife 15 at approximately 30 degrees from tail-on orientation in the lateral plane. The time delay on the horizontal axis has been converted to distance (cm) to represent the spatial separation between the scattering features of the fish. The processing sidelobe is an artifact of the pulse compression process, as illustrated in Fig. 3-7; therefore, any peak significantly higher than the processing sidelobe level represents a physical arrival from the fish.

and 3-14). In order to analyze this in terms of the scattering, time of arrival has been converted into separation distances. The overall separation and structure of the highlights in the CPO are a strong function of orientation angle. At normal incidence, there is generally a single, dominant peak. At oblique angles of incidence, multiple significant peaks are present in the received signal. The separation between the first and last arrival tends to increase for angles away from normal incidence.

The concept of partial wave target strength (PWTS) was introduced by Chu and Stanton (1998) to characterize the contributions by various individual highlights or partial

118
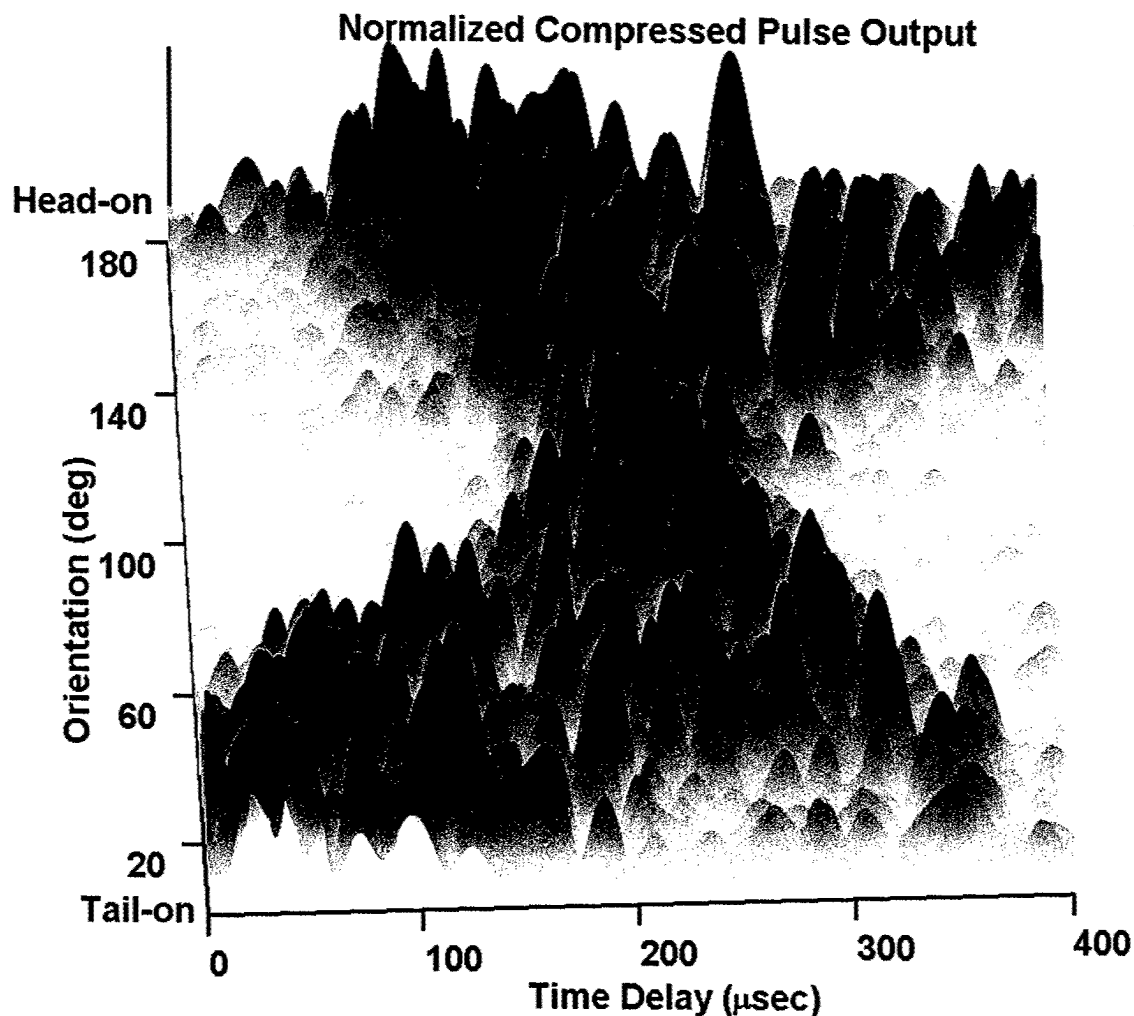
Figure 3-13: Normalized CPO (contour plot) for Alewife 17 as a function of angle of orientation and time delay, depicting the changing CPO as the fish is rotated from tail-on through broadside to head-on orientation in the dorsal/ventral plane. Each segment of the plot corresponding to each degree of rotation is the CPO from a single realization at that particular angle of orientation. At angles near end-on, the individual arrivals are spread out in time, whereas at angles near broadside, the individual rays return nearly simultaneously.

119

Normalized Compressed Pulse Output

Y-axis: Orientation (deg) from Tail-on (bottom) to Broadside (top), labeled 10, 20, 30, 40, 50, 60, 70

X-axis: Tail <-- Spatial Separation of Scattering Features (cm) --> Head, labeled -15, -10, -5, 0, 5, 10, 15
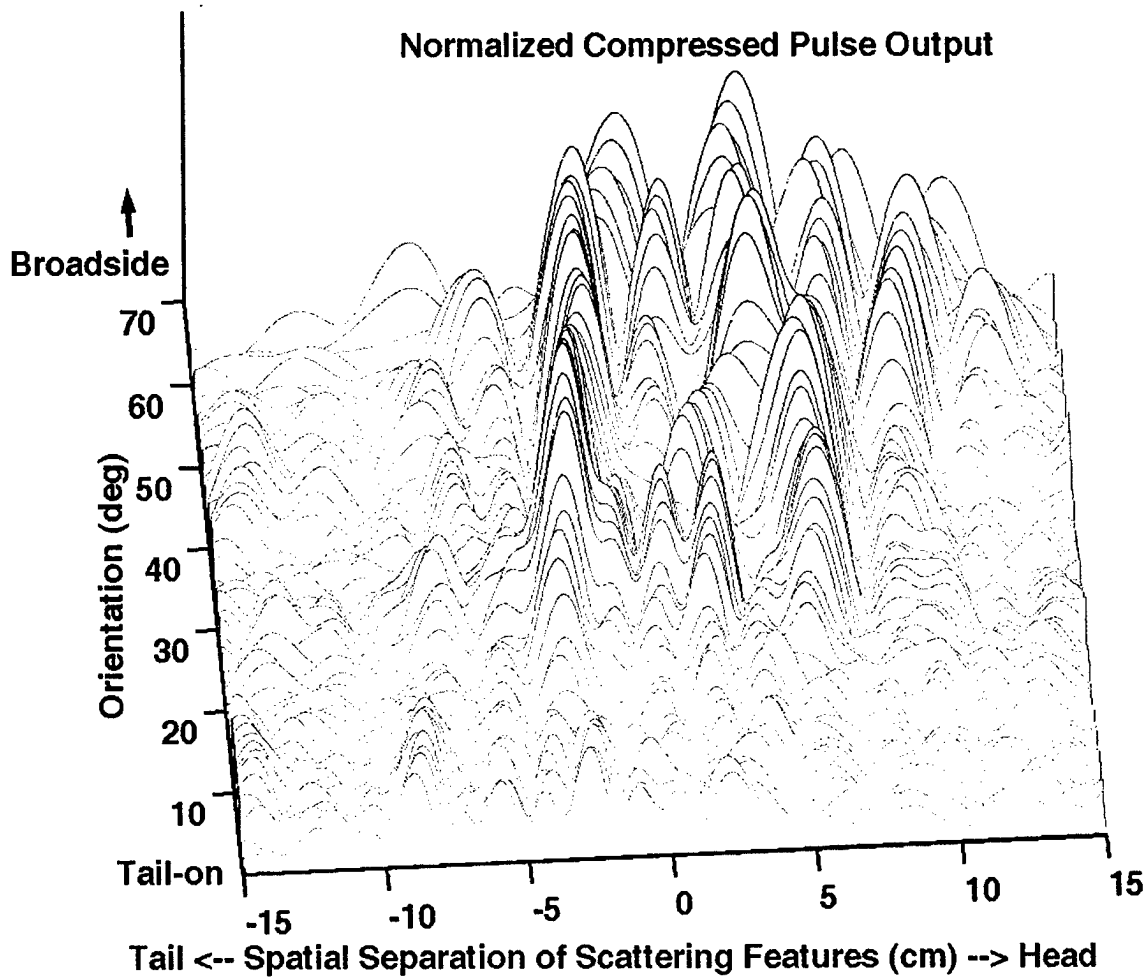
Figure 3-14: Normalized CPO for Alewife 15 as a function of angle of orientation and time delay converted to distance (along fish), depicting the changing CPO as the fish is rotated from tail-on to broadside orientation in the lateral plane. This figure is similar to Fig. 3-13, except that the conversion of time delay to distance allows better visualization of the scattering features and their changes as a function of angle of orientation.

120

waves that make up the total backscattered signal from the animal. PWTS is achieved by partitioning, or time-gating, the CPO to isolate scattering highlights of interest. The spectral characteristics of the PWTS features of these echoes are significantly different than that of the total signal (Figs. 3-15 and 3-16).

3.5 Modeling and comparison with data

3.5.1 Relating scattering features to fish anatomy

The dependencies of acoustic backscattering strength of the alewife on orientation, frequency and morphology are clearly seen in the data. The narrow width of the main lobes indicated in Fig. 3-8 correlates to scattering from the relatively long, narrow swimbladder and body. The difference between dorsal and ventral scattering directivity in Figs. 3-9 and 3-10 is also consistent with an elongated shape that also possesses a difference in the curvature between the two sides (i.e., the ventral side of the swimbladder is more rounded than the dorsal side). The pattern of peaks and nulls in Fig. 3-11 is consistent with constructive and destructive interference between multiple rays scattering from different parts of the body. The rays add constructively or destructively depending upon the location of the part of the body from which it is scattered, the frequency of the signal, and the angle of orientation in relation to the source/receiver transducer pair. Maximum target strength occurs near broadside incidence, as these multiple arrivals are in phase (or nearly so) and add coherently to the total target strength. As the orientation
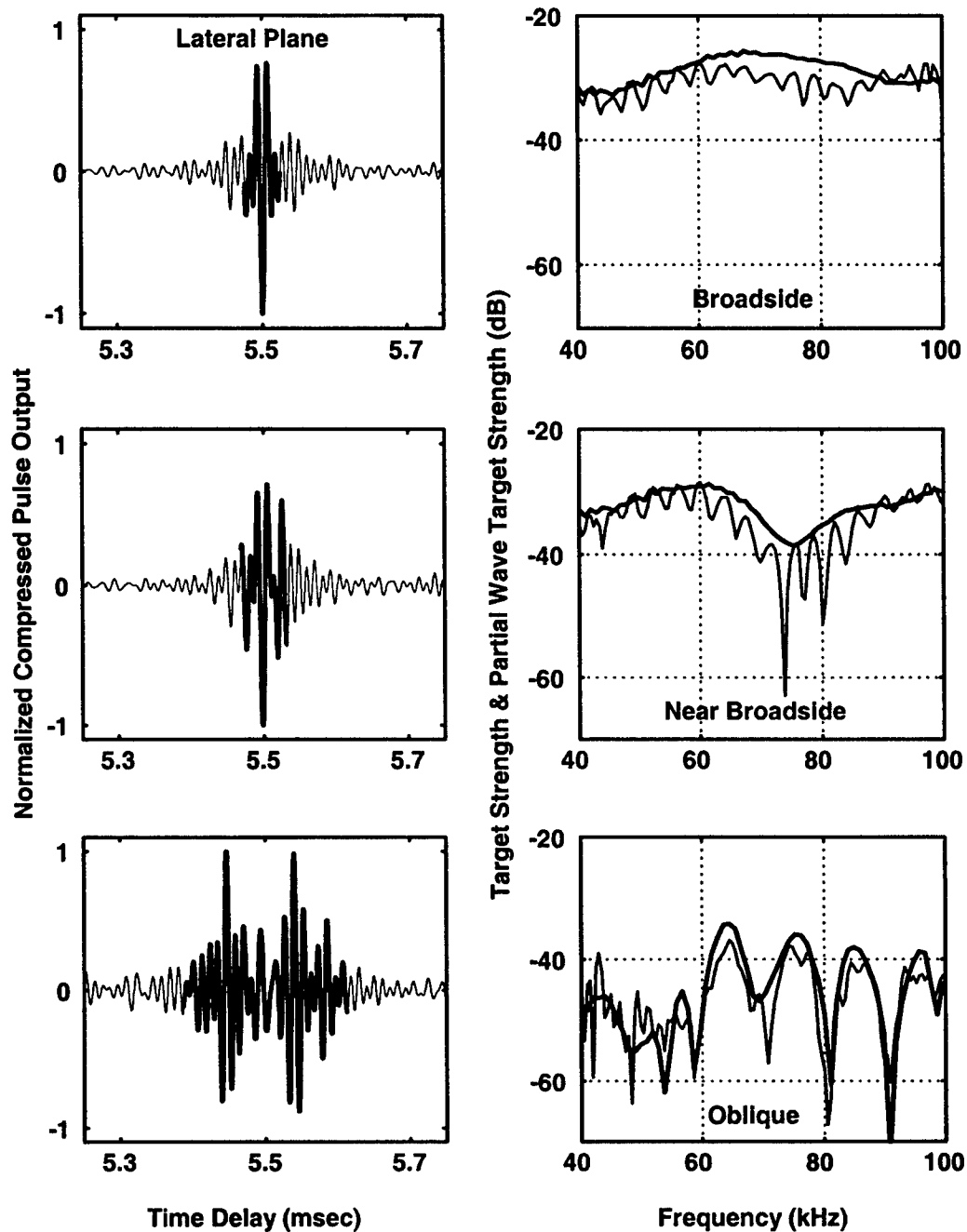
Figure 3-15: Normalized CPO, target strength and partial wave target strength (PWTS) for Alewife 15 at three different orientations in the lateral plane. The plots on the right are TS (thin lines) computed from the whole time series and PWTS (thick lines) computed from the thick-lined (time-gated) portions of the time series on the left.

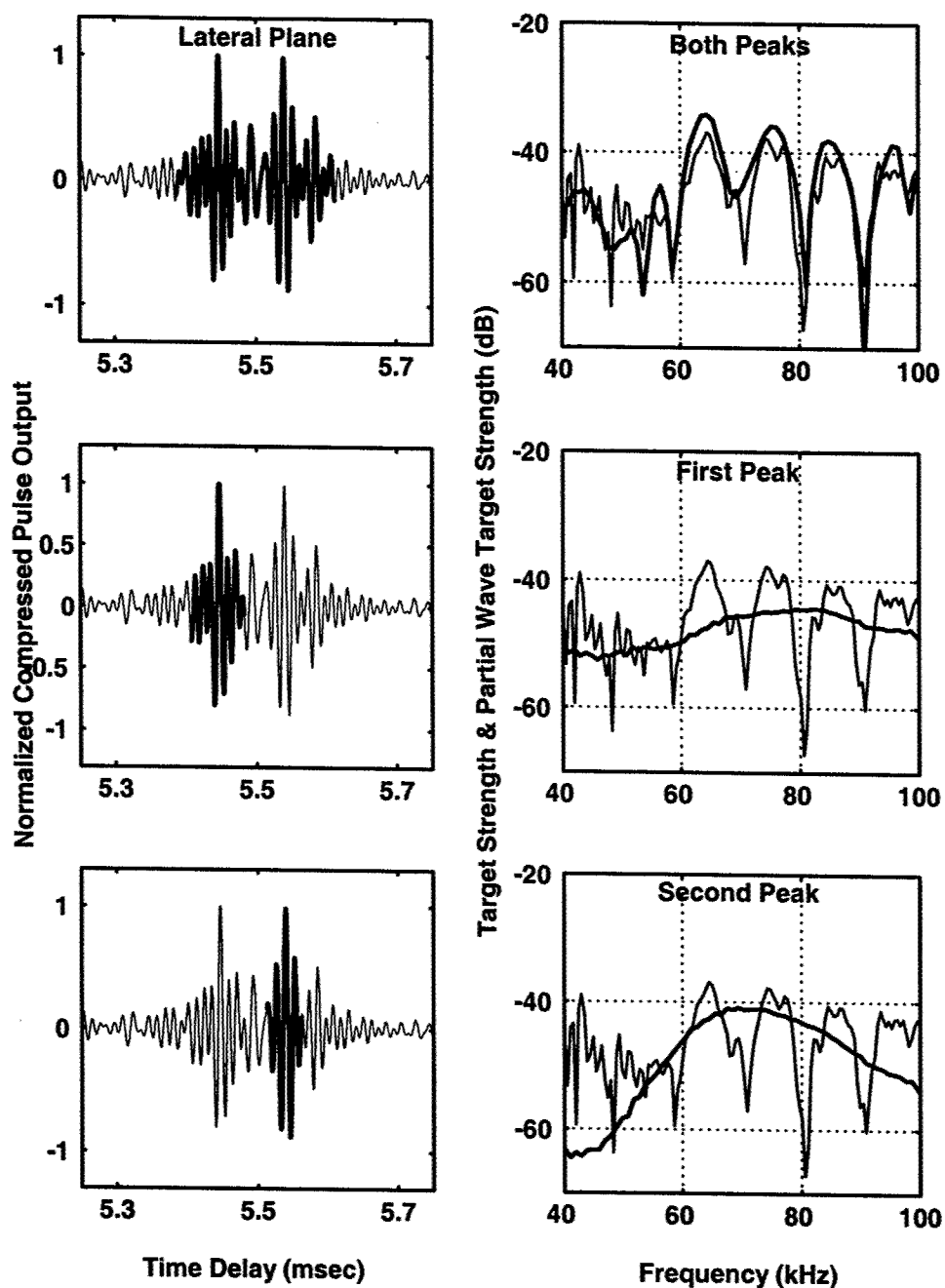Figure 3-16: Normalized CPO, target strength and partial wave target strength (PWTS) for Alewife 15 in the lateral plane. All three pairs of panels are for the same oblique angle of orientation, but represent processing of different segments of the CPO. The top pair of plots is identical to the bottom pair plots of Fig. 3-15 for reference, while the lower four panels illustrate the characteristics of the separate arrivals.

moves away from broadside incidence, the arrivals become well out of phase and add destructively at certain frequencies as evidenced by the one null and two broad peaks at near broadside incidence. At more oblique angles, the peaks and nulls are more closely spaced as constructive and destructive interferences occur at more frequencies within the band.

Through pulse compression processing, the individual arrivals from different parts of the body (which apparently cause the interference patterns in the spectral plots) are resolved, resulting in several significant scattering features being extracted from the received signal (Fig. 3-12). The separation of the peaks (~8 cm) correlates well with the physical separation between the skull and swimbladder of the alewife used in the experiment.

The separation in time of the arrivals from individual scattering features in the fish as it rotated in the acoustic beam is illustrated in Fig. 3-13. At tail-on orientation, the scattering features nearest the tail scatter the incident wave first, followed by scattering from other features as the incident wave travels from tail to head. As the orientation moves toward broadside, the time separation between the partial waves decreases as the physical separation of the scattering features in the transducer direction decreases. As the orientation moves toward head-on, the time separation increases again. The temporal distribution of the arrivals from different significant scatterers in the fish in Fig. 3-13 is apparent and is consistent with the physical separation of the scattering features in the fish; however, the contributions from individual scattering features in

124

the fish are indiscernible. In order to elucidate the dynamic contributions of individual scatterers in the fish as a function of orientation, temporal separation is converted to spatial separation (Fig. 3-14). The arrival nearest to the tail and apparently from the swimbadder, is generally the most significant contributor to the overall scattering throughout the 90 degree rotation. The scattering near the end of the time series, apparently from the head, is initially shadowed by the body of the fish and cannot be detected acoustically. As the fish is rotated toward broadside incidence, the head exits the acoustic shadow, and the amplitude of the arrival from the head increases. The arrivals between the head and swimbladder demonstrate complicated variable scattering mechanisms that are orientation dependent. The two significant scatterers within the fish nearest the head and tail are separated by approximately 12 cm, correlating well with the anatomical dimensions of the fish.

Partial wave target strength (PWTS) makes more evident the characteristics of selected arrivals in the backscattered signal and their interactions (Fig. 3-15). These constructive and destructive interferences vary as the animal's orientation changes according to the separation (relative to the transducers) of the scattering features with respect to the wavelength of the sound. At broadside incidence, the multiple arrivals are in phase (or nearly so) and add coherently, resulting in a relatively flat response over the band. As the orientation moves away from broadside, the arrivals add less coherently, causing the individual waves to add destructively at certain frequencies, which results in a series of peaks and nulls in the target strength over the frequency band. If the

125

multiple arrivals are analyzed separately, the interference mechanism can be further elucidated (Fig. 3-16). The partial wave target strengths of the individual first and second major arrivals at oblique angles exhibit smooth and relatively flatter responses than that of a combination of the two arrivals. This further illustrates the hypothesis that these resolved echoes are due to multiple singular scattering features.

3.5.2 Modeling the scattering

For all animals, it has been demonstrated experimentally that the acoustic backscattering is strongly dependent upon morphology, angle of orientation and frequency. In an effort to quantify these dependencies, the FMM and KRM models were used for predictions of target strength vs. angle to compare to the acoustic measurements of the alewife. Although, as shown above, there are several scattering features in the fish, the FMM predictions are based upon scattering from high resolution representations of the swimbladder alone,which is the dominant scatterer near broadside incidence, modeled with soft, or pressure-release, boundary conditions. The KRM results are based upon the coherent addition of the scattering from the swimbladder with soft boundary conditions and the scattering from the fish body with fluid boundary conditions.

Experimental measurements and accompanying model calculations are presented for two different fish (#15 and #17) at dorsal and ventral aspects at two different frequencies (Fig. 3-17). There is good agreement between the models and data in the general structure and amplitude of the target strength as a function of orientation. Both models and
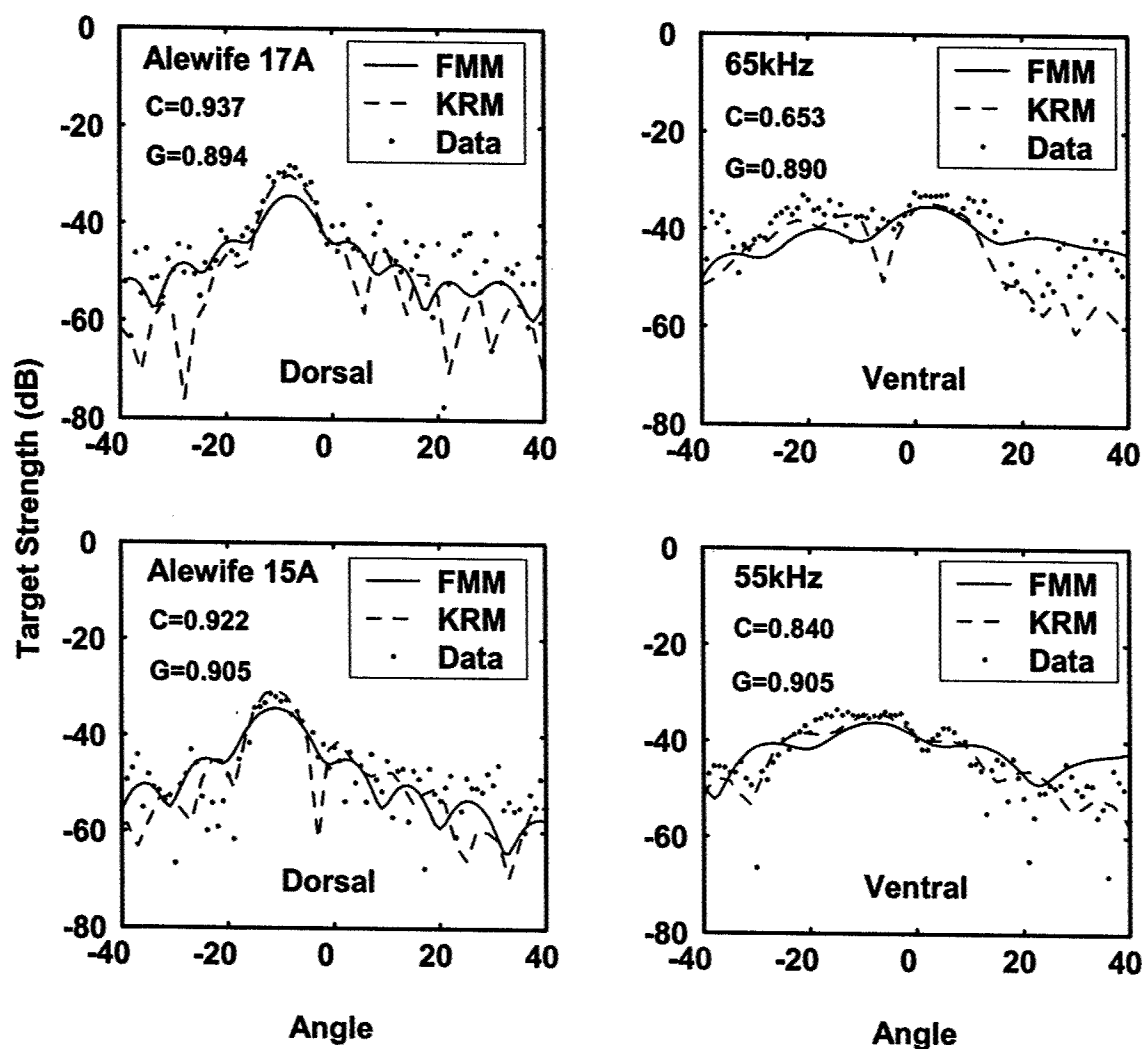
Figure 3-17: FMM, KRM and acoustic scattering data: Target strength as a function of angle of orientation for Alewife 15 and 17 in the dorsal/ventral plane at 65 kHz (top panels) and 55 kHz (bottom panels). C is the correlation coefficient, and G is the average relative error across the band between the FMM and measured values. The plotting convention is the same as Fig. 3-9. These particular frequencies were chosen due to the good fit between the models and data.
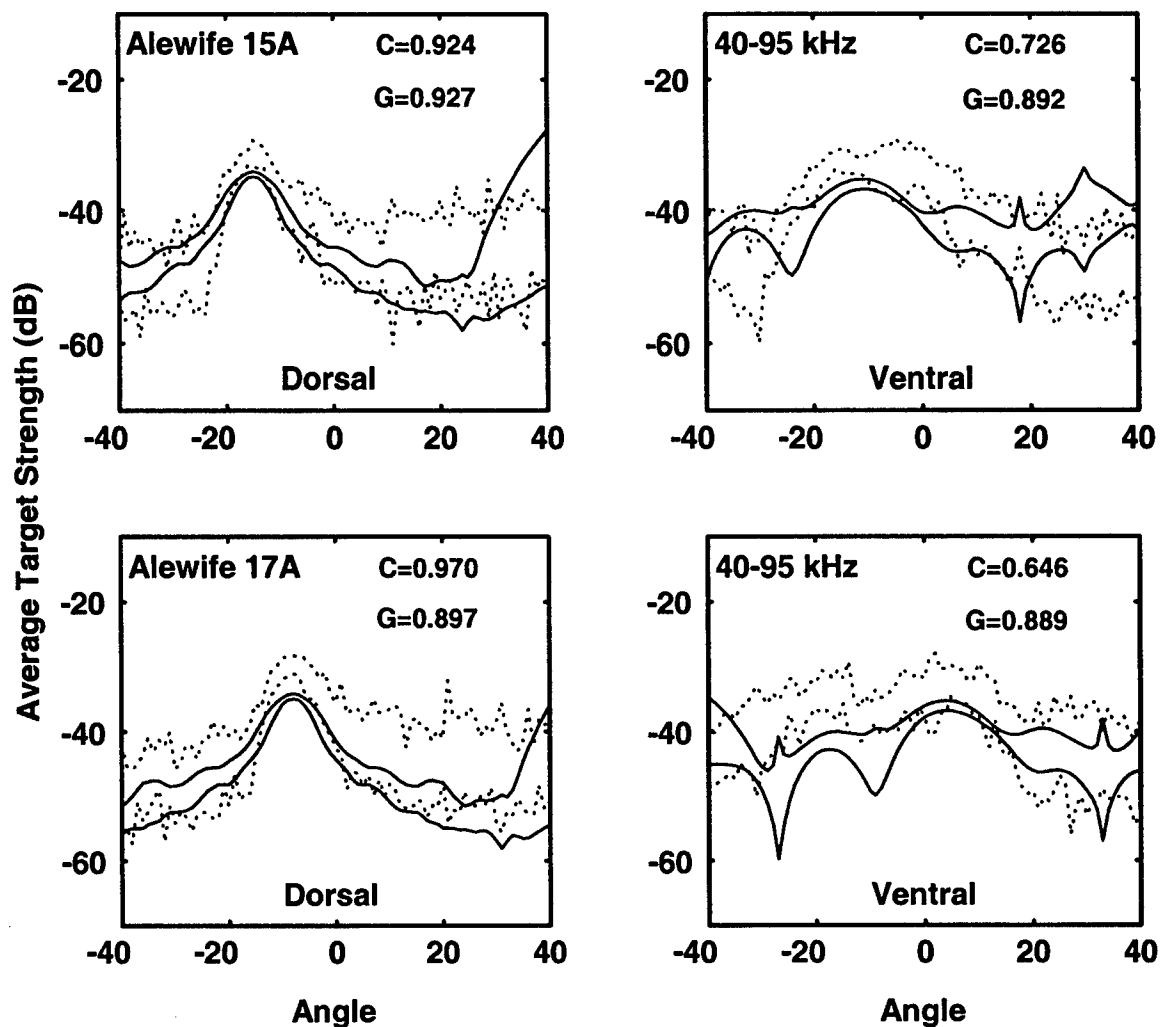
Figure 3-18: FMM and acoustic scattering data: Average target strength vs. angle of orientation for Alewife 15 and 17 in the dorsal/ventral plane. The backscattering cross sections were averaged across the band before taking the logarithm. C and G are the same as in Fig. 3-17, and the plotting convention is the same as in Fig. 3-9. The dots depict the standard deviation about the measured values, and the solid lines depict the standard deviation about the FMM predictions.

128

data demonstrate well the more narrow acoustic beampattern at dorsal aspect compared to that of the ventral aspect, which is consistent with morphology. Also consistent with morphology is the position of the center of the main lobe at broadside incidence. The position of the main lobe is a function of the position of the fish in the harness and the offset of the swimbladder within the fish from the axis of the fish body. It is expected that the FMM would typically under-predict the target strength predicted by the KRM and the actual target strength values from the measurements due to the fact that the FMM is based upon scattering from the swimbladder alone. Additionally, the conformal mapping formalism used in the FMM to model the shape of the swimbladder is two-dimensional, resulting in an axisymmetric shape. The mapping procedure accurately accounts for the shape along the length of the swimbladder; however, the cross-sectional radius of curvature is too small, contrbuting to the underprediction. This under-prediction by the FMM is particularly apparent at near-broadside angles. In the frequency band of interest (40-95 kHz), the KRM relies on the Kirchhoff approximation and is valid only at near-broadside incidence. The KRM prediction falls off too rapidly at off-broadside angles; hence, the FMM typically performs better than the KRM at off-broadside angles. For all frequencies at broadside incidence, the FMM and KRM generally agree with the data to within 6 dB in most cases.

The scattering process is highly complex and can depend on numerous parameters simultaneously. Predictions of single realizations are difficult to make due to the uncertainty and variability of each parameter. In this particular experiment, the animals

had some freedom of movement within the harness, which introduced significant variation into the acoustic data from realization to realization, while exhibiting consistent trends in the dependencies on orientation and frequency in all data sets. Therefore, comparisons between predictions and data for a single realization are generally qualitative. Quantitative comparisons can be made for both the statistics of scattering and for averaged levels, where the averages can be over some distribution of parameters, such as a distribution of sizes, angles of orientation or range of frequencies. An attempt was made to provide a relative quantification of the "goodness of fit" between the FMM and data. With each plot of target strength vs. angle, values of "C" and "G" are listed. The correlation coefficient between the FMM predictions and the data is designated "C", and the average relative error across the band between the FMM and data is designated "G." Typically, "C" tends to be a better measure of the agreement in the structure as a function angle, while "G" tends to be a better measure of the agreement in overall amplitude. In terms of structure and amplitude, scattering as a function of orientation angle at dorsal aspect was modeled better than at ventral aspect, as demonstrated by the slightly higher values of "C" and "G" for dorsal aspect.

Due to the high degree of variability of the data on an ping-by-ping, comparisons of data and model predictions can be difficult and sometimes qualitative at best. Given these challenges, model performance can be assessed based on comparisons of averages taken over a uniform distribution of orientations or frequencies. Average target strengths across the frequency band and standard deviations were computed from the acoustic mea-

130

surements and the FMM predictions (Fig. 3-18). The average target strength values were obtained by averaging the backscattering cross section over all frequencies (40-95 kHz), then taking the logarithm. While the FMM predicts the expected lower target strength at broadside angles, there is good agreement between the average target strengths from the measurements and the FMM. The overall amplitude of the target strength and the finer structure of the scattering as a function of orientation is smoothed out as a result of the averaging process; however, the high degree of variability in the data at all angles of orientation is demonstrated by the elevated levels of standard deviation about the average target strength values. The FMM predictions vary less over the frequency band, particularly at near broadside angles.

3.6   Summary and conclusions

In summary, detailed and extensive measurements of morphology and acoustic scattering and predictions of scattering have been made for adult alewife fish. The acoustic measurements consisted of using a greater-than-octave bandwidth (40-95 kHz), shaped chirp to insonify adult alewife that were tethered while being rotated. The acoustic scattering time series were measured in 1-degree increments of orientation angle over all angles in two planes of rotation (lateral and dorsal/ventral). High-resolution Phase Contrast X-rays (PCX) and Computerized Tomography (CT) scans were used for detailed morphological evaluation and measurement. Axisymmetric bodies of revolution for each aspect of the swimbladder were developed from the CT scans for use in the models. The

131

acoustic scattering predictions have been made by the FMM and KRM models. While the KRM is based on the Kirchhoff-ray mode approximation and specifically designed for fish scattering, the FMM is a three-dimensional conformal mapping, general scattering solution that is valid over a wide range of frequencies, from the low-frequency resonance region to the high-frequency geometric scattering region.

These data, as well as the modeling results and predictions, demonstrate that inclusion of exact morphology through the use of high-resolution imaging techniques and the use of broadband signals provide specific information about the scatterer. Specifically, analysis in both the spectral and time domains demonstrate that acoustic scattering by fish is strongly dependent upon morphology, orientation and frequency in both lateral and dorsal/ventral aspects. The use of pulse compression processing of the echoes from the animals allowed the temporal resolution of multiple returns from each individual, demonstrating that there exists more than one significant scattering feature in the animal, which could include the head, vertebral column, gonads and gut. The multiple returns from the animal also show good correlation with size and orientation. Comparisons between the model predictions and acoustic measurements show good agreement as a function of orientation for dorsal and ventral aspects. Further use of CT scans and PCX imaging on multiple species of fish under various conditions (juvenile vs. adult, spawning vs. non-spawning, shallow vs. deep, etc.) and subsequent modeling are necessary to expand understanding of the extent to which the various factors affect the scattering, as well as experimental investigations into the extent to which scattering by

anatomical features other than the swimbladder and fish body (gonads, gut, muscle tissue and vertebral column) contribute to the overall scattering.

Chapter 4

Summary and conclusions

This thesis investigates the complexities of acoustic scattering by finite bodies in general and by fish in particular. Through the extension of an advanced acoustic scattering model and the extensive measurement and associated analysis of acoustic backscattering by fish, the scattering properties of finite bodies and alewife fish are explored to determine the extent to which morphology, orientation and acoustic frequency affect the scattering. The following paragraphs provide a summary and conclusions of the thesis and recommendations for future work. The final section consists of a summary of the contributions of this thesis.

4.1 Modeling

In the second chapter, an advanced scattering model is presented. Specifically, a general acoustic scattering model is developed that is numerically efficient over a wide range of

frequencies, angles of orientation, irregular shapes and boundary conditions. The model presented is an extension of a two-dimensional conformal mapping approach to scattering by irregular, finite-length bodies of revolution. The model conformally maps the coordinate variables of the original coordinate system to a new orthogonal coordinate system in which the locus of all points where the new radial coordinate is a constant exactly coincides with the scatterer surface. The solutions to the transformed Helmholtz equation are a general solution for the total pressure in the case of far-field scattering by a finite-length body of revolution. This model has been shown to be very accurate in the prediction of scattering by smooth, symmetric bodies for a wide range of frequencies (resonance in the Rayleigh region through the geometric scattering region), scattering angles (monostatic and bistatic), aspect ratios and boundary conditions, and for all angles. Good agreement has also been demonstrated for irregular, realistic shapes when compared to the Kirchhoff approximation. While this method is a formally exact, numerically solved formulation which is valid for all frequencies and all angles of orientation, it is limited to far-field scattering by axisymmetric bodies and possesses practical limitations in its numerical implementation. Due to the limitations of machine precision, computation of converged solutions become more difficult with increasing frequency and eccentricity of scatterer shape. However, this work represents a significant advancement by providing a model whose usefulness generally extends over a wider range of conditions over other series-based models.

4.2 Measurement and analysis

In the third chapter, high-resolution morphological and acoustic scattering measurements of fish are conducted. In particular, high-resolution measurements of the morphology of fish have been made to accurately represent the exact shapes of the scattering features in the fish on which the models are based, and detailed acoustic backscattering measurements of fish have been made for the identification of dominant scattering mechanisms and refinement of the scattering models. Imaging technologies to exactly measure the morphology of the scattering features of fish include very high-resolution Phase Contrast X-rays (PCX) and Computerized Tomography (CT) scans. PCX technology provides a morphological evaluation tool for the small-scale anatomical features of alewife such as fins, ribs, striations in muscle tissue, gills and weakly scattering soft tissue. CT scans are used to produce high-resolution digital swimbladder objects that are used as scatterer shapes by the FMM. Detailed acoustic scattering measurements have been conducted, and acoustic model predictions have been made for adult alewife fish using the FMM and KRM models. These data, as well as the modeling results and predictions, have shown that the scattering process is highly complex and depends upon morphology, orientation and acoustic frequency. The acoustic measurements consisted of using a greater-than-octave bandwidth (40-95 kHz), shaped chirp to insonify adult alewife. The tethering system provided the control necessary to maintain the animal in the center of the acoustic beam while allowing sufficient movement of the fish in a naturally swimming position to minimize stress. The acoustic scattering time series were measured in two planes of

rotation (lateral and dorsal/ventral) in 1-degree increments over all angles of orientation. Strong dependence upon morphology, orientation and frequency in both lateral and dorsal/ventral aspects was demonstrated in the analysis and plots of the data in both the spectral and time domains. Temporal resolution of multiple returns from each individual fish by the use of pulse compression processing of the echoes demonstrated that there exists more than one significant scattering feature in the animal. The multiple returns from the animal also show good correlation with size and orientation.

Ultimate objectives of this research include the improvement in the use of acoustic surveys for numerical abundance estimates, size estimates and species identification, as well as improvement in naval sonar system performance by feature extraction from scattered acoustic signals. Quantitative use of acoustics in the ocean requires studies such as this one, which combine scattering models with high-resolution morphological information and high-quality laboratory data. Specifically, good agreement between measured and predicted target strengths increase confidence in the use of acoustic scattering models to estimate numerical abundance of fish in ocean surveys, thus reducing reliance upon traditional net surveys. Increased SNR and improvement in the probability of detection would result from inclusion of acoustic scattering models in naval sonar systems to aid in the discrimination between unwanted reverberation and target echoes.

4.3 Recommendations for future work

There is great potential for further development of the FMM, including extension to elastic boundary conditions. The use of extended precision format of floating point arithmetic, implementation of better numerical integration techniques, derivation of certain mathematical expressions in a form that is less susceptible to roundoff error, and various smoothing techniques (Yamashita, 1990) could delay the onset of ill-conditioned matrices, improving the result. New scaling techniques based upon the physical scattering mechanisms (Schmidt, 1993) and incorporation of prolate spheroidal radial and angular wave functions could also improve performance.

Further use of CT scans and PCX imaging on multiple species of fish under various conditions (juvenile vs. adult, spawning vs. non-spawning, shallow vs. deep, etc.) and subsequent modeling are necessary to expand understanding of the extent to which the various factors affect the scattering. Experimental investigations into the extent to which scattering by anatomical features other than the swimbladder and fish body (gonads, gut, muscle tissue and vertebral column) contribute to the overall scattering are needed. These experimental investigations could include bistatic scattering measurements that could exhibit enhanced scattering profiles that are not evident in the backscattering configuration.

4.4 Contributions of this thesis

- Extension of the FMM to three dimensions as a formally exact, general solution to far-field scattering by axisymmetric irregular, finite-length bodies for all frequencies (resonance in the Rayleigh region through the geometric scattering region) for all angles of orientation (forward scattering, bistatic scattering and backscattering), and for soft, rigid and fluid boundary conditions. This numerically efficient formulation is generally useful over a wider range of conditions than other series-based solutions.

- Detailed and extensive measurement of broadband acoustic scattering by adult alewife in 1-degree increments of orientation angle over all angles in two planes of rotation (lateral and dorsal/ventral). Through spectral and temporal analysis, these measurements elucidate dominant scattering features of fish that are correlated to size, anatomy and orientation.

- Use of new phase contrast x-ray (PCX) technique and high-resolution computerized tomography (CT) scans to not only evaluate the morphology, but to generate digital scattering shapes for input into scattering models.

- Application of the new, more general FMM model to predicting acoustic scattering by fish through use of high-resolution morphometry.

139

Bibliography

Anderson, V.C. (1950) "Sound scattering from a fluid sphere," J. Acoust. Soc. Am., 22:426-431.

Andreyeva, I.B. (1964) "Scattering of sound by air bladders of fish in deep sound-scattering ocean layers," Sov-Phys-Acoust., 10:17-20.

Au, W.W.L., and Banks, K. (1998) "The acoustics of the snapping shrimp Synalpheus parneomeris in Kaneohe Bay," J. Acoust. Soc. Am., 103: 41-47.

Baggeroer, A.B., Sperry, B., Lashkari, K., Chiu, C.S., Miller, J.H., Mikhalevsky, P.N., and von Der Heydt, K. (1994). "Vertical array receptions of the Heard Island transmissions," J. Acoust. Soc. Am., 96:2395-2413.

Born, M., and Wolf, E. (1999) *Principles of Optics* (Seventh Edition, University Press, Cambridge).

Bowman, J.J., Senior, T.B.A., and Uslenghi, P.L.E. (1987) *Electromagnetic and Acoustic Scattering by Simple Shapes* (Hemisphere Publishing Corp., New York).

Chu, D., and Stanton, T.K. (1998) "Application of pulse compression techniques to broadband acoustic scattering by live individual zooplankton," J. Acoust. Soc. Am., 104:39-55.

Clay, C.S. (1991) "Low-resolution acoustic scattering models: Fluid-filled cylinders and fish with swimbladders," J. Acoust. Soc. Am., 89:2168-2179.

Clay, C.S., and Heist, B.G. (1984) "Acoustic scattering by fish-acoustic models and a 2-parameter fit," J. Acoust. Soc. Am., 75:1077-1083.

Clay, C.S., and Horne, J.K. (1994) "Acoustic models of fish: The Atlantic cod (*Gadus morhua*)," J. Acoust. Soc. Am., 96:1661-1668.

Davis, T.J., and Stevenson, A.W. (1996) "Direct measure of the phase shift of an x-ray beam," J. Opt. Soc. Am., 13: 1193-1198.

Dawson, J.J. and Karp, W.A. (1990) "In situ measures of target-strength variability of individual fish," Rapp. P.-v. Reun. Cons. Int. Explor. Mer., 189:264-273.

Diercks, K.J., and Goldsberry, T.G. (1970) "Target strength of a single fish," J. Acoust. Soc. Am., 48:415-416.

DiPerna, D.T., and Stanton, T.K. (1994) "Sound scattering by cylinders of noncircular cross section: A conformal mapping approach," J. Acoust. Soc. Am., 96:3064-3079.

Do, M.A., and Surti, A.M. (1990) "Estimation of dorsal aspect target strength of deep-water fish using a simple model of swimbladder back scattering," J. Acoust. Soc. Am., 87:1588-1596.

Faran, J.J. (1951) "Sound scattering by solid cylinders and spheres," J. Acoust. Soc. Am., 23:405-417.

Feuillade, C., and Werby, M.F. (1994) "Resonances of deformed gas bubbles in liquids," J. Acoust. Soc. Am., 96:3684-3692.

Feuillade, C., and Nero, R.W. (1998) "A viscous-elastic swimbladder model of describing enhanced-frequency resonance scattering from fish," J. Acoust. Soc. Am., 103:3245-3255.

Flammer, C. (1957) *Spheroidal Wave Functions* (Stanford University Press, Stanford).

Fogerty, M.J., and Murawski, S.A. (1998) "Large-scale disturbance and the structure of marine systems: Fishery impacts on Georges Bank," Ecol. Appl., 8:S6-S22.

Foote, K.G. (1980) "Importance of the swimbladder in acoustic scattering by fish: A comparison of gadoid and mackerel target strengths," J. Acoust. Soc. Am., 67:2084-2089.

Foote, K.G. (1985) "Rather-high-frequency sound scattering by swimbladdered fish," J. Acoust. Soc. Am., 78:688-700.

Foote, K.G. (1987) "Fish target strengths for use in echo integrator surveys," J. Acoust. Soc. Am., 82:981-987.

Foote, K.G. (1997) "Target strength of fish," In *Encyclopedia of Acoustics* (Ed. by Malcolm J. Crocker, John Wiley and Sons, New York).

Foote, K.G. (2001) "Acoustic scattering by marine organisms," In *Encyclopedia of Ocean Sciences* (Ed. by J.H. Steele, K.K. Turekian and S.A. Thorpe; Academic Press, London).

Foote, K. G., and Francis, D. T. I. (2002) "Comparing Kirchhoff-approximation and boundary-element models for computing gadoid target strengths," J. Acoust. Soc. Am., 111:1644-1654.

Francis, D.T.I. (1993) "A gradient formulation of the Helmholtz integral equation for acoustic radiation and scattering," J. Acoust. Soc. Am., 93:1700-1709.

Francis, D.T.I. (2001) Personal communication.

Furusawa, M. (1988) "Prolate spheroidal models for predicting general trends of fish target strength," J. Acoust. Soc. Jpn. (E), 9:13-24.

Gaunaurd, G.C. (1985) "Sonar cross sections of bodies partially insonified by finite sound beams," IEEE J. Ocean. Eng., 10:213-230.

Goodman, R.R., and Stern, R. (1962) "Reflection and transmission of sound by elastic spherical shells," J. Acoust. Soc. Am., 34:338-344.

Greenlaw, C.F., and Johnson, R.K. (1983) "Multiple-frequency acoustical estimation," Biol. Oceanography, 2:227-252.

Gunderson, D.R. (1993) *Surveys of Fisheries Resources* (John Wiley and Sons, New York).

Gureyev, T.E., Stevenson, A.W., Paganin, D., Mayo, S.C., Pogany, A., Gao, D., and Wilkins, S.W. (2000) "Quantitative methods in phase-contrast x-ray imaging," J. of Dig. Imaging, 13: 121-126.

Hackman, R.H. (1993) "Underwater Scattering and Radiation," In *Physical Acoustics*, Vol. XXII, Ed. A.D. Pierce and R.N. Thurston (Academic Press, San Diego).

Hackman, R.H., and Todoroff, D.G. (1985) "An application of the spheroidal-coordinate-based transition matrix: The acoustic scattering from high aspect ratio solids," J. Acoust. Soc. Am., 78:1058-1071.

Haslett, R.W.G. (1962a) "Determination of the acoustic back-scattering patterns and cross sections of fish," Br. J. Appl. Phys., 13:349-357.

Haslett, R.W.G. (1962b) "Determination of the acoustic scatter patterns and cross sections of fish models and ellipsoids," Br. J. Appl. Phys., 13:611-620.

142

Haslett, R.W.G. (1962c) "Measurement of the dimensions of fish to facilitate calculations of echo-strength in acoustic fish detection," J. Cons. Int. Explor. Mer., 27:261-269.

Haslett, R.W.G. (1969) "The target strengths of fish," J. Sound Vib., 9:181-191.

Haslett, R.W.G. (1977) "Automatic plotting of polar diagrams of target strength of fish in roll, pitch and yaw," Rapp. P.-v. Reun. Cons. Int. Explor. Mer., 170:74-81.

Hawkins, A.D. (1977) "Fish sizing by means of swimbladder resonance," Rapp. P.-v. Reun. Cons. Int. Explor. Mer., 170:122-129.

Hawkins, A.D. (1981) "Some biological sources of error in the acoustical assessment of fish abundance," In Meeting on Hydroacoustical Methods for the Estimation of Marine Fish Populations, Draper Lab., Cambridge, MA, June, 1979.

Hildebrand, F.B. (1964) *Advanced Calculus for Applications* (Prentice-Hall. New Jersey).

Horne, J.K. (1998) "Acoustic approaches to remote species identification," In Remote Species Identification Workshop Report, Monterey, CA, August, 1998. Ed. by J.K. Parrish.

Horne, J.K., and Jech, J.M. (1999) "Multi-frequency estimates of fish abundance: constraints of rather high frequencies," ICES J. Mar. Sci., 56:184-199.

Jones, F.R.H., and Pearce, G. (1958) "Acoustic reflexion experiments with perch (*Perca fluviatilis Linn.*) to determine the proportion of the echo returned by the swimbladder," J. Exp. Biol., 35:437-450.

Junger, M.C. (1951) "Sound scattering by thin elastic shells," J. Acoust. Soc. Am., 24:366-373.

Junger, M.C. (1982) "Scattering by slender bodies of revolution," J. Acoust. Soc. Am., 72:1954-1956.

Kjaergaard, L., Bjorno, L., Kirkegaard, E., and Lassen, H. (1990) "Broadband analysis of acoustical scattering by individual fish," Rapp. P.-v. Reun. Cons. Int. Explor. Mer., 189:370-380.

Lakhtakia, A., Varadan, V.K., and Varadan, V.V. (1984) "Iterative extended boundary condition method for scattering by objects of high aspect ratios," J. Acoust. Soc. Am., 76:906-912.

Levy, B.R., and Keller, J.B. (1959) "Diffraction by a smooth object," Comm. on Pure Applied Math., 12:159-209.

Love, R.H. (1969) "Maximum side-aspect target strength of an individual fish," J. Acoust. Soc. Am., 46:746-752.

Love, R.H. (1970) "Dorsal-aspect target strength of an individual fish," J. Acoust. Soc. Am., 49:816-823.

Love, R.H. (1971) "Measurements of fish target strength: A review," Fishery Bulletin, 69:703-715.

Love, R.H. (1977) "Target strength of an individual fish at any aspect," J. Acoust. Soc. Am., 62:1397-1403.

Love, R.H. (1978) "Resonant acoustic scattering by swimbladder-bearing fish," J. Acoust. Soc. Am., 64:571-580.

Medwin, H., and Clay, C.S. (1998) *Fundamentals of Acoustical Oceanography* (Academic Press, Boston).

Midttun, L. (1984) "Fish and other organisms as acoustic targets," Rapp. P.-v. Reun. Cons. Int. Explor. Mer., 184:25-33.

Miyanohana, Y., Ishii, K., and Furusawa, M. (1990) "Measurements and analyses of dorsal-aspect target strength of six species of fish at four frequencies," Rapp. P.-v. Reun. Cons. Int. Explor. Mer., 189:317-324.

Morse, P.M., and Feshbach, H. (1953) *Methods of Theoretical Physics* (McGraw-Hill, Boston).

Morse, P.M. (1981) *Vibration and Sound* (Acoustical Society of America).

Nakken, O., and Olsen, K. (1977) "Target strength measurements of fish," Rapp. P.-v. Reun. Cons. Int. Explor. Mer., 170:52-69.

Nash, D.M., Sun, Y., and Clay,C.S. (1987) "High resolution acoustic structure of fish," J. Cons. int. Explor. Mer., 43:23-31.

Neubauer, W.G. (1963) "Summation formulation for use in determining the reflection from irregular bodies," J. Acoust. Soc. Am., 35:279-285.

Neubauer, W.G. (1986) *Acoustic Reflection from Surfaces and Shapes* (Naval Research Laboratory, Washington, DC).

Ogilvy, J.A. (1991) *Theory of Wave Scattering from Random Rough Surfaces* (IOP Publishing, Adam Hilger, Bristol, UK).

144

Oliveri, M.P., and Glegg, S.A.L. (1998) "Measurements of snapping shrimp colonies using a wideband mobile passive sonar," J. Acoust. Soc. Am., 103:3000.

Ona, E. (1990) "Physiological factors causing natural variations in acoustic target strength of fish, " J. Mar. Biol. Assoc. U.K., 70:107-127.

Partridge, C. and Smith, E.R. (1995) "Acoustic scattering from bodies: Range of validity of the deformed cylinder method," J. Acoust. Soc. Am., 97:784-795.

Press, W.H., Teukolsky, S.A., Vetterling, W.T. and Flannery, B.P. (1992) *Numerical Recipes in Fortran: The Art of Scientific Computing* (Second Edition, Cambridge University Press, Australia).

Rayleigh, Lord (J.H. Strutt) (1945) *The Theory of Sound* (Dover, New York).

Reeder, D.B. and Stanton, T.K. (submitted) "Acoustic scattering by axisymmetric finite bodies: an extension of a 2-dimensional conformal mapping method," J. Acoust. Soc. Am.

Reeder, D.B., Jech, J.M, and Stanton, T.K. (submitted) "Broadband acoustic backscatter an high-resolution morphology of fish: Measurement and modeling," J. Acoust. Soc. Am.

Sammuelmann, G.S., Trivett, D.H., and Hackman, R.H. (1988) "High-frequency scattering from rigid prolate spheroids," J. Acoust. Soc. Am., 83:46-54.

Schmidt, H. (1993) "Numerically stable global matrix approach to radiation and scattering from spherically stratified shells," J. Acoust. Soc. Am., 94:2420-2430.

Schmitz, B., Versluis, M., von der Heydt, A., and Lohse, D. (2000) "A unique way of sound production in the snapping shrimp (*Alpheus heterochaelis*)," J. Acoust. Soc. Am., 108:2542.

Simmonds, J.E., Armstrong, F., and Copland, P.J. (1996) "Species identification using wideband backscatter with neural network and discriminant analysis," ICES J. Mar. Sci., 53:189-195.

Spence, R.D., and Granger, S. (1951) "The scattering of sound from a prolate spheroid," J. Acoust. Soc. Am., 23:701-706.

Stanton, T.K. (1988a) "Sound scattering by cylinders of finite length. I. Fluid cylinders," J. Acoust. Soc. Am., 83:55-63.

Stanton, T.K. (1988b) "Sound scattering by cylinders of finite length. II. Elastic cylinders," J. Acoust. Soc. Am., 83:64-67.

Stanton, T.K. (1989a) "Sound scattering by cylinders of finite length. III. Deformed cylinders," J. Acoust. Soc. Am., 86:691-705.

Stanton, T.K. (1989b) "Simple approximate formulas for the backscattering of sound by spherical and elongated objects," J. Acoust. Soc. Am., 86:1499-1510.

Stanton, T.K., Chu, D., Wiebe, P.H., and Clay, C.S. (1993) "Average echoes from randomly oriented random-length finte cylinders: Zooplanktonn models," J. Acoust. Soc. Am., 94:3463-3472.

Stanton, T.K., Wiebe, P.H., Chu, D., Benfield, M.C., Scanlon, L., Martin, L., and Eastwood, R.L. (1994a) "On acoustic estimates of zooplankton biomass," ICES J. Mar. Sci., 51:505-512.

Stanton, T.K., Chu, D., Wiebe, P.H., Martin, L.V., and Eastwood, R.L. (1998a) "Sound scattering by several zooplankton groups. I. Experimental determination of dominant scattering mechanisms," J. Acoust. Soc. Am., 103:225-235.

Stanton, T.K., Chu, D., Wiebe, P.H. (1998b) "Sound scattering by several zooplankton groups: II. Scattering Models," J. Acoust. Soc. Am., 103:236-253.

Stanton, T.K., Chu, D., Wiebe, P.H., Eastwood, R.L., and Warren, J.D. (2000) "Acoustic scattering by benthic and pelagic shelled animals," J. Acoust. Soc. Am., 108:535-550.

Steele, J.H. (1998) "Regime shifts in marine ecosystems," Ecol. Appl., 8:S33-S36.

Strang, G. (1986) *Introduction to Applied Mathematics* (Wellesley-Cambridge, Wellesley, MA).

Strasberg, M. (1953) "The pulsation frequency of nonspherical gas bubbles in liquids," J. Acoust. Soc. Am., 25:536-537.

Stevenson, A.W. (2002) Personal communication.

Sun, Y., Nash, R., and Clay, C.S. (1985) "Acoustic measurements of the anatomy of fish at 220 kHz," J. Acoust. Soc. Am., 78:1772-1776.

Svensson, U.P, Fred, R.I., and Vanderkooy, J. (1999) "An analytic secondary source model of edge diffraction impulse responses," J. Acoust. Soc. Am., 106:2331-2344.

Tobacman, W. (1984) "Calculation of acoustic wave scattering by means of the Helmholtz integral equation," J. Acoust. Soc. Am., 76:599-607.

Turin, G.L. (1960) "An introduction to matched filters," IRE Trans. Info. Thy., IT-6:311-329.

Uberall, H., Doolittle, R.D., and McNicholas, J.V. (1966) "Use of sound pulses for a study of circumferential waves," J. Acoust. Soc. Am., 39:564-578.

Urick, R.J. (1983) *Principles of underwater sound* (Peninsula Publishing).

Varadan, V.K., Varadan, V.V., Dragonette, L.R., and Flax, L. (1982) "Computation of rigid body scattering by prolate spheroids using the T-matrix approach," J. Acoust. Soc. Am., 71:22-25.

Versluis, M., von der Heydt, A., Lohse, D., and Schmitz, B. (2000) "On the sound of snapping shrimp: The collapse of a cavitation bubble," J. Acoust. Soc. Am., 108:2541-2542.

Waterman, P.C. (1968) "New formulation of acoustic scattering," J. Acoust. Soc. Am., 45:1417-1429.

Weston, D.E. (1967) "Sound propagation in the presence of bladder fish," *Underwater Acoustics*, Ed. by V.M. Albers (Plenum Press, New York).

Wilkens, S.W., Gureyev, T.E., Gao, D., Pogany, A., and Stevenson, A.W. (1996) "Phase-contrast imaging using polychromatic hard x-rays," Nature, 384:335-338.

Williams, K.L., and Marston, P.L. (1985) "Backscattering from an elastic sphere: Sommerfeld-Watson transformation and experimental confirmation," J. Acoust. Soc. Am., 78:1093-1102.

Yamashita, E. (1990) *Analysis Methods for Electromagnetic Wave Problems* (Artech House, Norwood, MA).

Ye, Z., and Farmer, D.M. (1994) "Acoustic scattering from swim-bladder fish at low frequencies," J. Acoust. Soc. Am., 96:951-956.

Ye, Z. (1996) "Acoustic scattering from fish swimbladders," J. Acoust. Soc. Am., 99:785-792.

Ye, Z., Hoskinson, E., Ding, L., and Farmer, D.M. (1997) "A method for acoustic scattering by slender bodies. I. Theory and verification," J. Acoust. Soc. Am. 102:1964-1976.

Ye, Z. and Hoskinson, E. (1998) "Low-frequency acoustic scattering by gas-filled prolate spheroids in liquids. II. Comparison with the exact solution," J. Acoust. Soc. Am., 103:822-826.

Yeh, C. (1967) "Scattering of acoustic waves by a penetrable prolate spheroid. I. Liquid prolate spheroid," J. Acoust. Soc. Am. 42:518-521.

Zakharia, M.E. (1990) "Variations in fish target strength induced by movement: a wideband-impulse experiment," Rapp. P.-v. Reun. Cons. Int. Explor. Mer., 189:398-404.

Zakharia, M.E., Magand, F., Hetroit, F., and Diner, N. (1996) "Wideband sounder for fish species identification at sea," ICES J. Mar. Sci., 53:203-208.

University of California, San Diego
SIO Library 0175C
9500 Gilman Drive
La Jolla, CA 92093-0175

Hancock Library of Biology & Oceanography
Alan Hancock Laboratory
University of Southern California
University Park
Los Angeles, CA 90089-0371

Gifts & Exchanges
Library
Bedford Institute of Oceanography
P.O. Box 1006
Dartmouth, NS B2Y 4 A2
CANADA

NOAA/EDIS Miami Library Center
4301 Rickenbacker Causeway
Miami, FL 33149

Research Library
U.S. Army Corps of Engineers
Waterways Experiment Station
3909 Halls Ferry Road
Vicksburg, MS 39180-6199

Institute of Geophysics
University of Hawaii
Library Room 252
2525 Correa Road
Honolulu, HI 96822

Marine Resources Information Center
Building E38-320
MIT
Cambridge, MA 02139

Library
Lamont-Doherty Geological Observatory
Columbia University
Palisades, NY 10964

Library
Serials Department
Oregon State University
Corvallis, OR 97331

Pell Marine Science Library
University of Rhode Island
Narragansett Bay Campus
Narragansett, RI 02882

Working Collection
Texas A&M University
Dept. of Oceanography
College Station, TX 77843

Fisheries-Oceanography Library
151 Oceanography Teaching Bldg.
University of Washington
Seattle, WA 98195

Library
R.S.M.A.S.
University of Miami
4600 Rickenbacker Causeway
Miami, FL 33149

Maury Oceanographic Library
Naval Oceanographic Office
Building 1003 South
1002 Balch Blvd.
Stennis Space Center, MS 39522-5001

Library
Institute of Ocean Sciences
P.O. Box 6000
Sidney, B.C. V8L 4B2
CANADA

National Oceanographic Library
Southampton Oceanography Centre
European Way
Southampton SO14 3ZH
UK

The Librarian
CSIRO Marine Laboratories
G.P.O. Box 1538
Hobart, Tasmania
AUSTRALIA 7001

Library
Proudman Oceanographic Laboratory
Bidston Observatory
Birkenhead
Merseyside L43 7 RA
UK

IFREMER
Centre de Brest
Service Documentation–Publications
BP 70 29280 PLOUZANE
FRANCE

50272-101

REPORT DOCUMENTATION PAGE	1. REPORT NO. MIT/WHOI 2002-11	2.	3. Recipient's Accession No.
4. Title and Subtitle Acoustic Scattering by Axisymmetric Finite-Length Bodies with Application to Fish: Measurement and Modeling			5. Report Date June 2002
			6.
7. Author(s) D. Benjamin Reeder			8. Performing Organization Rept. No.
9. Performing Organization Name and Address MIT/WHOI Joint Program in Oceanography/Applied Ocean Science & Engineering			10. Project/Task/Work Unit No. MIT/WHOI 2002-11
			11. Contract(C) or Grant(G) No. (C) N00014-98-1-0879 (G)
12. Sponsoring Organization Name and Address Office of Naval Research			13. Type of Report & Period Covered Ph.D. Thesis
			14.

15. Supplementary Notes

16. Abstract (Limit: 200 words)

This thesis investigates the complexities of acoustic scattering by finite bodies in general and by fish in particular through the development of an advanced acoustic scattering model and detailed laboratory acoustic measurements. A general acoustic scattering model is developed that is accurate and numerically efficient for a wide range of frequencies, angles of orientation, irregular axisymmetric shapes and boundary conditions. The model presented is an extension of a two-dimensional conformal mapping approach to scattering by irregular, fine-length bodies of revolution. An extensive series of broadband acoustic backscattering measurements has been conducted involving alewife fish (*Alosa pseudoharengus*), which are morphologically similar to the Atlantic herring (*Clupea harengus*). A greater-than-octave bandwidth (40-95 kHz), shaped, linearly swept, frequency modulated signal was used to insonify live, adult alewife that were tethered while being rotated in 1-degree increments over all angles of orientation in two planes of rotation (lateral and dorsal/ventral). Spectral analysis correlates frequency dependencies to morphology and orientation. Pulse compression processing temporally resolves multiple returns from each individual which show good correlation with size and orientation, and demonstrate that there exists more than one significant scattering feature in the animal. Imaging technologies used to exactly measure the morphology of the scattering features of fish include very high-resolution Phase Contrast X-rays (PCX) and Computerized Tomography (CT) scans, which are used for morphological evaluation and incorporation into the scattering model. Studies such as this one, which combine scattering models with high-resolution morphological information and high-quality laboratory data, are crucial to the quantitative use of acoustics in the ocean.

17. Document Analysis   a. Descriptors

Acoustic Scattering
Underwater Acoustics
Acoustic Modeling

b. Identifiers/Open-Ended Terms

c. COSATI Field/Group

18. Availability Statement Approved for publication; distribution unlimited.	19. Security Class (This Report) UNCLASSIFIED	21. No. of Pages 148
	20. Security Class (This Page)	22. Price

(See ANSI-Z39.18)	*See Instructions on Reverse*	OPTIONAL FORM 272 (4-77) (Formerly NTIS-35) Department of Commerce